UNIVERSITÀ DEGLI STUDI DI PADOVA
DIPARTIMENTO DI FISICA E ASTRONOMIA GALILEO GALILEI

SCUOLA DI DOTTORATO DI RICERCA IN FISICA
CICLO XXVIII

Production of the new pixel detector for the upgrade of the CMS experiment and study of anomalous couplings in the non-resonant Higgs bosons pair production in p-p collisions at $\sqrt{s}$ = 13 TeV

DIRETTORE DELLA SCUOLA:
PROF. Andrea Vitturi

SUPERVISORE:
PROF. Dario Bisello

CO-SUPERVISORE:
DOTT. Tommaso Dorigo

DOTTORANDO:
Martino Dall'Osso

a Sara,

Riassunto

Questo lavoro di tesi è stato svolto nell'ambito della collaborazione CMS, uno degli esperimenti progettati per studiare la fisica delle collisioni protone-protone al Large Hadron Collider (LHC) presso il CERN.

La sperimentazione a CMS (ed a ATLAS) ha portato nel 2012 alla scoperta di una nuova particella che è stata in seguito identificata come il bosone di Higgs, l'ultimo tassello mancante dello Standard Model delle interazioni fondamentali. Tutti gli esperimenti a LHC sono in una fase di miglioramento degli apparati in vista del continuo aumento di luminosità di LHC e del conseguente aumento del rate di eventi per collisione.
Il progetto di upgrade di CMS prevede tra l'altro la produzione di un nuovo rivelatore a pixel (CMS Phase 1 Pixel Upgrade) da inserire nell'apparato all'inizio del 2017. Parte cruciale dell'upgrade è il nuovo chip di lettura (ROC) dei sensori al silicio, *psi46digV2respin*, disegnato al Paul Scherrer Institute (PSI) in tecnologia CMOS 250 nm. Tale chip rappresenta lo stato dell'arte nell'elettronica di lettura di rivelatori al silicio.
La tesi riguarda lo studio e lo sviluppo di procedure di test di questo nuovo chip di lettura. Grazie ad una lunga permanenza al PSI ho potuto fornire un importante contributo alle fasi di debug delle prime versioni del ROC e del TBM, il chip che gestisce i diversi ROCs all'interno di un pixel module, ed allo sviluppo del software utilizzato da tutta la collaborazione per il test del ROC e dei moduli.
Questa esperienza mi ha permesso essere l'esperto per l'installazione e messa a punto dei sistemi di lettura dei ROC nei centri di produzione di moduli in Italia. Inoltre ho gestito il test dei ROC wafers fin dalle prime fasi di sviluppo del progetto. I ROC sono prodotti su wafers di silicio e subiscono diversi processi di lavorazione prima dell'assemblaggio sui moduli, *e.g.*, la deposizione di metalli sulle pixel pads, l'assottigliamento ed il taglio. Queste lavorazioni comportano stress meccanici e termici che possono danneggiare i chips. Il test dei ROC wafers è stato quindi effettuato, con la stessa procedura, prima e dopo la lavorazione per ridurre al minimo la frazione di ROCs non funzionanti montati sui moduli. Si è misurato che la lavorazione dei wafers introduce una riduzione del 5.2% del numero di ROCs perfettamente funzionanti. Nella tesi sono riportati la catena di produzione del rivelatore a pixel, il processo di qualifica dei moduli ed il dettaglio dei test su ROC wafers. Vengono inoltre descritte le modifiche apportate alla tecnologia utilizzata per la connessione ROC-sensore.

L'installazione del nuovo rivelatore a pixel permetterà di aumentare l'efficienza di ricostruzione delle tracce e di mantenere una risoluzione di 10-15 μm nella ricostruzione dei vertici d'interazione anche all'aumentare del numero medio di eventi per interazione p-p dagli attuali 15 a 50-60 nel 2017. Le ottime prestazioni del nuovo rivelatore di vertice a pixel sommate al previsto aumento di luminosità (un fattore 35 tra il valore attuale e quello previsto per il 2017) potranno dare accesso a processi fisici con bassa sezione d'urto ed alto numero di b quarks negli stati finali.

Viene a tal fine presentato uno studio preliminare della produzione non risonante di

coppie di bosoni di Higgs nel canale di decadimento completamente adronico ($b\bar{b}\ b\bar{b}$), analizzando i dati raccolti dall'esperimento CMS nel 2015, pari a 2.19 fb^{-1}. Questo processo presenta una ridotta sezione d'urto, secondo il Modello Standard, e la sua misura in collisioni p-p ad energie del centro di massa di 13-14 TeV è prevista solo con un'elevata quantità di dati (ab^{-1}). I dati raccolti nel 2015 non permettono di ottenere un limite ragionevole sulla sezione d'urto di produzione di tale processo e l'analisi verrà sviluppata pienamente nel 2016 e nei successivi anni.

Lo studio della produzione di coppie di bosoni di Higgs è rilevante poich esse possono essere prodotte anche in seguito ad accoppiamenti non previsti dal Modello Standard (anomali), come l'interazione di contatto tra bosoni di Higgs e gluoni. Tali accoppiamenti anomali danno luogo ad un incremento della sezione d'urto del processo e ad una differente cinematica degli stati finali. Il processo di produzione di coppie di bosoni di Higgs per mezzo di accoppiamenti anomali è descritto da una Lagrangiana con cinque parametri liberi. Questo comporta una difficoltà nell'individuare i punti dello spazio dei parametri da indagare sperimentalmente.
Ho sviluppato una tecnica di analisi che permette, attraverso lo studio di campioni simulati, di suddividere tale spazio in regioni cinematicamente simili ed identificare per ognuna di esse il punto maggiormente significativo. La distanza tra i diversi punti dello spazio dei parametri è stata definita tramite un binned likelihood ratio ed un algoritmo iterativo è stato sviluppato per raggruppare tali punti. Sono state quindi individuate dodici regioni cinematicamente simili in uno spazio 5-D. I risultati di tale studio, descritti in questa tesi, sono raccolti in un articolo in fase di pubblicazione su JHEP e verranno considerati come linee guida per le ricerche di produzione non risonante di coppie di bosoni di Higgs a CMS.

Abstract

The present thesis work has been carried out in the framework of the CMS collaboration, one of the experiment designed to study the physics of the proton-proton collisions at the Large Hadron Collider (LHC) at CERN.

Experimentation at CMS (and at ATLAS) led to the discovery of a new particle in 2012 which has been identified as the Higgs boson, the missing brick of the Standard Model of the fundamental interactions. All the experiments at LHC are upgrading their detectors in order to fulfill the continuous increment of the LHC luminosity and the consequent increment of the per collision event rate.
The CMS upgrade project foresees, inter alia, the production of a new pixel detector (CMS Phase 1 Pixel Upgrade) to be commissioned at the beginning of 2017. Crucial part of the upgrade is the new readout chip (ROC) for the silicon sensor, *psi46digV2respin*, designed at the Paul Scherrer Institute (PSI) with a 250 nm CMOS technology. This chip represents the state of the art in the readout electronics for the silicon detectors.
The thesis concerns the study and the development of test procedures for this new readout chip. Thanks to a long stay at PSI, I could provide an important contribution to the debug phases of the first version of the ROC and TBM, the chip that handles the various ROCs in the pixel module, and to the development of the software used by the whole collaboration for the ROC and module testing.
This experience allowed me to be the expert for the installation and commissioning of the ROC readout system in all the production centres in Italy. Furthermore, I managed the ROC wafers test from the early project phases. The ROCs are produced on silicon wafers and undergo various processes before being assembled on the modules, *e.g.*, metal deposition on the pixel pads, thinning and dicing. These processes lead mechanical and thermal stresses that can damage the chips. The ROC wafers test has thus been performed following the same procedure before and after the processing. In order to minimize the failing ROCs fraction mounted on the modules. It has been measured that the processing introduces a 5.2% reduction of the number of perfectly working ROCs. The pixel detector production line, the module qualification process and the ROC wafers test results are reported in this thesis. The modifications performed on the ROC-sensor connection technology are also described.

The new pixel detector installation will allow an increase of the tracks reconstruction efficiency and a 10-15 μm resolution to be maintained in the interaction vertices reconstruction, independently from the increment of the mean number of events per p-p interaction from the current 15 to 50-60 in 2017. The excellent performances of the new pixel vertex detector plus the planned increment of the luminosity (a factor 35 between 2017 and the current value) could allow access to physical processes with a low cross section and a high number of b quarks in the final states.

For this purpose, a preliminary study on the non-resonant Higgs bosons pair production in the fully hadronic decay channel ($b\bar{b}\ b\bar{b}$) is here presented. The study has been

performed analysing the data collected by the CMS experiment in 2015, equal to 2.19 fb^{-1}. This process has a low cross section, accordingly to the SM, and its measurement in p-p collision at centre of mass energies of 13-14 TeV is forecast only with a high amount of data (ab^{-1}). The data collected in 2015 do not allow to set a reasonable exclusion limit on the cross section of this process and the analysis will be completely developed in 2016 and following years.

The study of the Higgs bosons pair production is relevant because the pairs can be produced also after couplings which are not allowed by the Standard Model (anomalous), such as the higgs-gloun contact interaction. These anomalous couplings lead to an increment of the cross section of the process and to differences in the kinematics of the final states. The process of Higgs bosons pair production via anomalous couplings is described by a Lagrangian with five free parameters. This implies a difficulty in the identification of parameters space point to be experimentally investigated.
I developed an analysis technique which allows, by studying simulated samples, to divide the parameters space in kinematically similar regions and to identify a benchmark in each of them. The distance among different points of the parameters space has been defined through a binned likelihood ratio and an iterative algorithm has been developed to group them together. Twelve regions which are kinematically equivalent have been identified in a 5-D space. The results of this study, described in this thesis, are collected in an article which is under publication on JHEP and they will be considered as guideline for the searches of non-resonant Higgs bosons pair production at CMS.

Contents

Introduction

The fundamental constituents of matter can interact via four forces: electromagnetic, weak, strong, and gravitational. In the context of particle physics, the first three interactions are described by a single theory, the Standard Model (SM) of fundamental interactions. Formulated in the late sixties, the SM has been tested by a huge variety of experiments and no evidence of deviation from its predictions has been measured so far. All the particles predicted by the SM have been experimentally confirmed, last but not least the Higgs boson, which has been discovered in 2012 by the LHC experiments at CERN [1, 2].

Although the particle physics scenario seems to be properly described by the SM, there are some aspects of the theory that still lack an explanation, *e.g.*, the hierarchy problem or the masses and mixings of quarks and leptons. Furthermore, the necessity of the presence of additional fundamental laws or particles in nature is coming from other physical observations, such as the recent experimental evidence for neutrino oscillations [3, 4], the matter/antimatter asymmetry in the Universe [5] and the necessary presence of the dark matter [6]. A lot of alternative or complementary theoretical scenarios have been formulated, the so-called Beyond Standard Model (BSM) theories; however, no evidence has been found for any of them yet.

The search for BSM phenomena, together with the study of the Higgs boson properties, is currently one of the main topics of the experiments at the LHC. The BSM searches are mainly performed looking for resonance states induced by the presence of new particles introduced by BSM theories, such as SuperSymmetry (SUSY) [7]. The BSM effects can also be highlighted from possible variations of parameters predicted by the SM. This is the case of the search for Higgs boson pairs production, which allows to study possible Higgs boson anomalous couplings induced by BSM phenomena.

The search for di-Higgs production at the LHC is currently in its preliminary phase, since its SM cross-section is extremely low and an elevated statistics is needed in order to set meaningful exclusion limits to this process. Di-Higgs production is thus one of the physical processes which will be widely studied in the next years of LHC operation. This search will therefore take advantage of the upgrade projects planned for the experiments at LHC. These upgrades are foreseen because of the increment of the LHC performances over the next few years which will lead to a more challenging environment for the current detectors. In particular, the CMS experiment will undergo an important upgrade at the beginning of 2017, which consists in the substitution of the whole pixel detector. The production of the new detectors started at the beginning of 2015 and the project is currently in its core phase. The new CMS pixel detector will lead to improvements in the tracking reconstruction and in the b-tagging efficiency, even in the highly crowded environment of the interaction region in CMS in the future years.

The CMS Pixel Upgrade project, together with the study of di-Higgs boson pairs production, will be described in this thesis.

In Chapter 1, the LHC and the CMS experiment are introduced. The CMS sub-detectors

are described with a focus on the current Pixel detector. The objects reconstruction techniques are also explained and the algorithm for the jet b-tagging is defined.

In Chapter 2, the CMS Pixel Phase 1 Upgrade project is described. The main features of the upgraded detector are reported with a focus on the new read-out chip (ROC). The production of the new pixel detector is then introduced and the module production line in Italy is described in detail. In particular, the ROC wafer test procedure and its results are shown.

In Chapter 3, after a brief introduction on the SM and the Higgs mechanism, the Higgs boson pairs production in p-p collision is described. A parametrization of the Lagrangian, which describes the non-resonant Higgs boson pairs interaction in BSM contexts, is introduced and the current searches for Higgs boson pairs at LHC are illustrated.

In Chapter 4, a statistical approach to define physical benchmarks to be studied in a complex BSM scenario is shown. The technique has been developed by studying the parameters spaces related to the Higgs boson anomalous couplings in the context of the di-Higgs production.

Finally, in Chapter 5, a preliminary study of the non-resonant di-Higgs production in its four b-quark jet final state is shown. This study is performed on the data collected by CMS in 2015 at a center of mass energy of 13 TeV.

Chapter 1

The Large Hadron Collider and the CMS experiment

1.1 The Large Hadron Collider

The Large Hadron Collider (LHC) [8] is a two-ring-superconducting-hadron accelerator and collider installed in a 26.7 km circular tunnel at CERN. The LHC is designed to produce collision of two proton-proton beams up to a centre of mass energy ($\sqrt{s}$) of 13 TeV and lead-lead beams collision up to 5.5 TeV nucleon-nucleon. The tunnel in which the LHC is placed was constructed between 1984 and 1989 for the LEP accelerator [9]. It has eight straight sections and eight arcs and lies between 45 m and 170 m below the surface on a plane inclined at 1.4 grades sloping towards the Léman lake. The LHC is connected to the CERN accelerator complex, that acts as injector, by two transfer tunnels of approximately 2.5 km in length. The LHC injection chain is composed by several accelerators. The proton beam is first accelerated by a LINAC, where its energy firstly reaches 50 MeV via a linear accelerator, then it passes through a booster, with energy increased to 1.4 GeV, and through the PS and the SPS accelerators where the beam energy rises up to 450 GeV. Finally, the beam is injected in the LHC ring, where it completes several revolutions to reach the planned energy. The LHC ring and the acceleration chain are sketched in Fig. 1.1.

The two main features of a collider like LHC are the energy of the centre of mass of the collisions, related to the beam energy, and the amount of events per second that can be produced in the collision, related to the luminosity. LHC is the world-leader machine in both aspects and the 13 TeV centre of mass collision energy obtained in the summer 2015 is the highest energy reached so far by any kind of particle accelerator.

The acceleration of protons inside LHC is made by radio-frequency cavities (400 MHz), giving a 492 keV energy gain per revolution, with a 7 keV loss per turn due to synchrotron radiation. The rise to the targeted acceleration is obtained with thousands of passages of the beam inside the circular accelerator. This is possible thanks to superconducting magnets displaced along the ring, among which 1232 superconducting dipoles operating in a bath of liquid helium at a temperature of 1.9 K, that can provide a maximum magnetic field of 8.4 T (11850 A current), necessary to bend the particle beam and to keep it into the circular tunnel. The total stored energy in the LHC magnets is equal to 11 GJ.

Inside the LHC there are two proton beams that circulate in opposite direction in separated ultra-vacuum tubes. The two beams are tilted and bring to collision only inside the four experimental areas present along the LHC tunnel. The beam is composed by several bunches with a fixed spatial separation. The machine luminosity depends only on the beam parameters and, considering a Gaussian distribution of the beam in the transverse

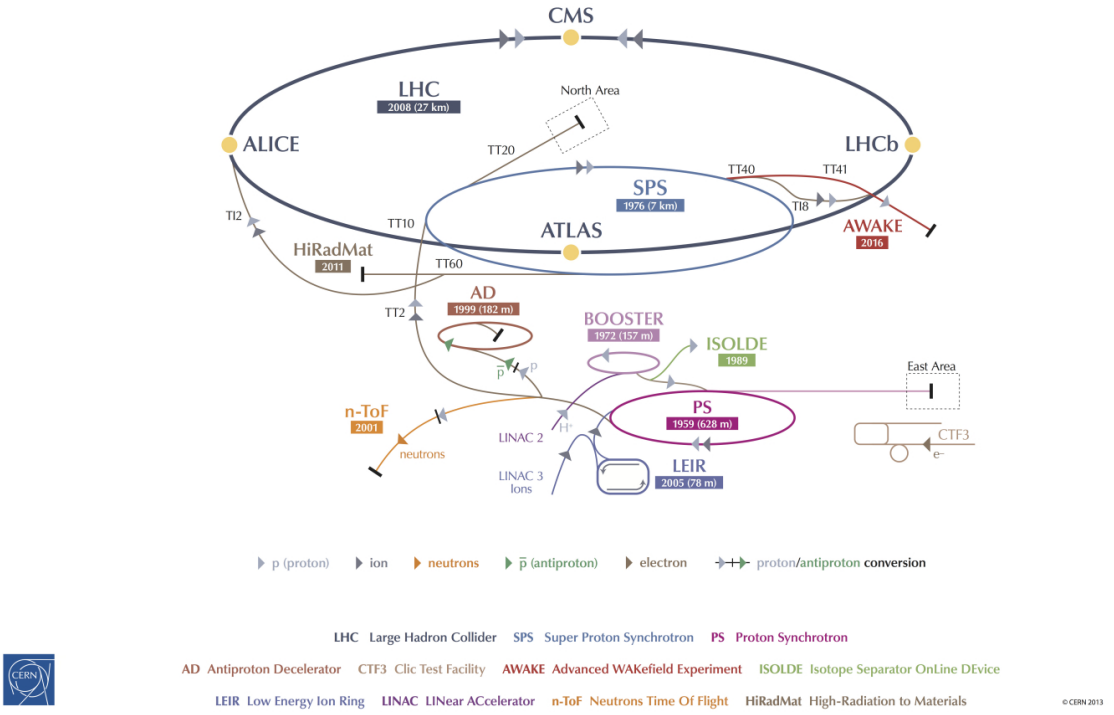

Figure 1.1: Schematic view of the CERN accelerator complex.

plane, it can be written as:

$$L = \frac{N_b^2 n_b f_{rev} \gamma_r}{4\pi\epsilon_n \beta} F \tag{1.1}$$

where N_b is the number of particles per bunch, n_b the number of bunches per beam, f_{rev} the revolution frequency, γ_r the relativistic gamma factor, ϵ_n the normalized transverse beam emittance, β the beta function at the collision point, and F the geometric luminosity reduction factor due to the crossing angle at the interaction point defined as:

$$F = \left(1 + \left(\frac{\theta_c \sigma_z}{2\sigma^*}\right)^2\right)^{-1/2} \tag{1.2}$$

where θ_c is the full crossing angle at the interaction point, σ_z the RMS bunch length, and σ^* the transverse RMS beam size at the IP. The above expression assumes beams with a circular transverse section, with $\theta_c << \beta$ and with beam parameters equal for both beams. The high luminosity of the LHC beams is thus obtained with a high frequency bunch crossing and a high density of protons per bunch. Each proton beam is separated by a fixed distance which defines the collision frequency (40 MHz by design). The usage of two proton beams and the possibility of reach higher centre of mass energies, lead to a greater partonic cross section with respect to previous colliders, such as Tevatron (Fig. 1.2). This allows to get higher statistics and it has been essential to obtain the discovery of the Higgs boson and to improve the sensitivity of the new searches beyond the Standard Model (BSM).

Beams collisions take place in four points of the LHC tunnel where the four main experiments are present: ATLAS (*A Toroidal LHC ApparatuS*) [10], CMS (*Compact Muon Solenoid*) [11], LHCb (*LHC beauty experiment*) [12] and ALICE (*A Lead Ion Collider Experiment*) [13]. ATLAS and CMS are general purpose experiments, designed to get an extensive study of

SM and BSM physics and to operate at a peak luminosity of $L = 10^{34} cm^{-2} s^{-1}$ for proton collision. The LHCb experiment is instead optimized for bottom quark physics studies while ALICE is dedicated to the study of the lead-lead collisions with a peak luminosity of $L = 10^{27} cm^{-2} s^{-1}$.

LHC operation officially started at the beginning of September 2008 but it stopped after a short period, due to the breakdown of superconductor magnets. The collider has been reactivated in November 2009 with first proton-proton collisions at $\sqrt{s}$ = 900 GeV, officially starting a new era in the particle physics experiments. Up to now, two main periods of machine operation took place: *LHC Run1* and *LHC Run2*.

1.1.1 LHC Run 1

In March 2009, the LHC beams energy has been substantially incremented and the first p-p collisions with $\sqrt{s}$ = 7 TeV were obtained. In the whole Run 1, the LHC operated with a 50 ns bunch spacing and about 1380 colliding bunches. By the end of 2010 the total integrated luminosity delivered at $\sqrt{s}$ = 7 TeV was $L = \int \mathcal{L} dt = 44.96\, pb^{-1}$ ($44.96 \times 10^{-36} cm^2$). The centre of mass energy remained stable for the whole 2011 with a peak of instantaneous luminosity of $\mathcal{L}_{max} = 3.54 \times 10^{33}\, cm^{-2} s^{-1}$ and 6.10 fb^{-1} were delivered by the end of 2011 [14]. In 2012 the beam energy increased to 4 TeV per beam, with peak instantaneous luminosities up to $7.67 \times 10^{33}\, cm^{-2} s^{-1}$ and 23.3 fb^{-1} delivered integrated luminosity within the end of that year [14]. The increment of the instantaneous luminosity leads to a no more negligible number of simultaneous interactions per bunch crossing, the so-called *pile-up* (PU) events. It obviously depends on the cross section of inelastic collisions ($\sim$ 75 mb at $\sqrt{s}$ = 7 TeV [15]), and it is directly linked to number of particle per bunch and to the beam parameters, thus to the instantaneous luminosity. The average PU of the data collected in 2012 is equal to 21 (Fig. 1.3) while it has been around 15 in the 2011. Lead-lead collisions have been also performed in the 2011 at $\sqrt{s}$ = 2.76 TeV/nucleon with a delivered integrated luminosity of 184.07 μb^{-1}.

1.1.2 LHC Run 2

A shut-down period for the LHC occurred in the whole 2013 and 2014, where upgrades and technical improvements have been performed in order to reach the designed instantaneous luminosity and centre of mass energy. A 5.61 pb^{-1} proton-proton collisions at $\sqrt{s}$ = 2.76 TeV have been delivered into the 2013. On March, 21st 2015 the first proton-proton collisions at $\sqrt{s}$ = 13 TeV were obtained, a new record-breaking energy. For the first three months the machine operated with 50 ns bunch spacing while, from August 2015, it has been reduced to the designed 25 ns. A number of bunches per beam equal to 2244 and a β^* of 80 cm for collisions ATLAS and CMS experiment have been reached for the first time in 2015. The first part of this Run 2 proton-proton operation ended on November 2015 with a total delivered integrated luminosity of 4.24 fb^{-1} and a peak of instantaneous luminosity of $\mathcal{L}_{max} = 5.13 \times 10^{33}\, cm^{-2} s^{-1}$, with an average pileup of 12. Pb-Pb collisions have been also delivered at $\sqrt{s}$ = 5.02 TeV/nucleon energy with a final 0.6 nb^{-1} integrated luminosity at the end of 2015 [14]. The LHC Run 2 restart is planned around April 2016, after an end-of-the-year technical stop, and a peak luminosity of $1.2 \times 10^{34}\, cm^{-2} s^{-1}$ is expected to be reached. The machine is planned to remain in operation at $\sqrt{s}$ = 13 TeV for the whole year with an expected integrated luminosity of 30 fb^{-1}. Accordingly to the current LHC schedule, the Run 2 will proceed up to the end of 2018 with a total expected integrated luminosity of $\sim$ 100 fb^{-1}.

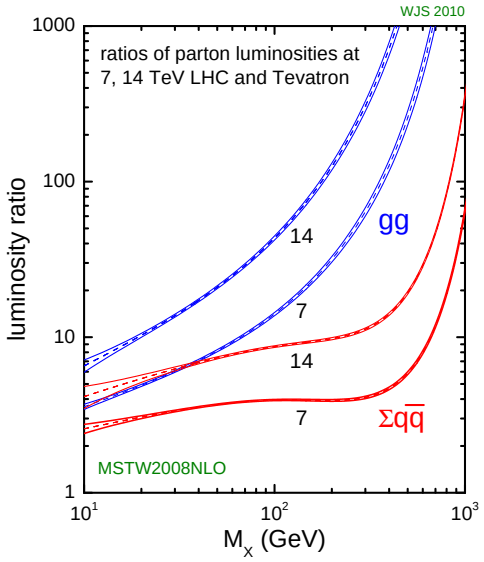

Figure 1.2: Parton luminosity ratios of $\sqrt{s}$ = 7, 14 TeV p-p collisions at LHC and $\sqrt{s}$ = 1.96 TeV p-$\bar{p}$ collisions at Tevatron [16].

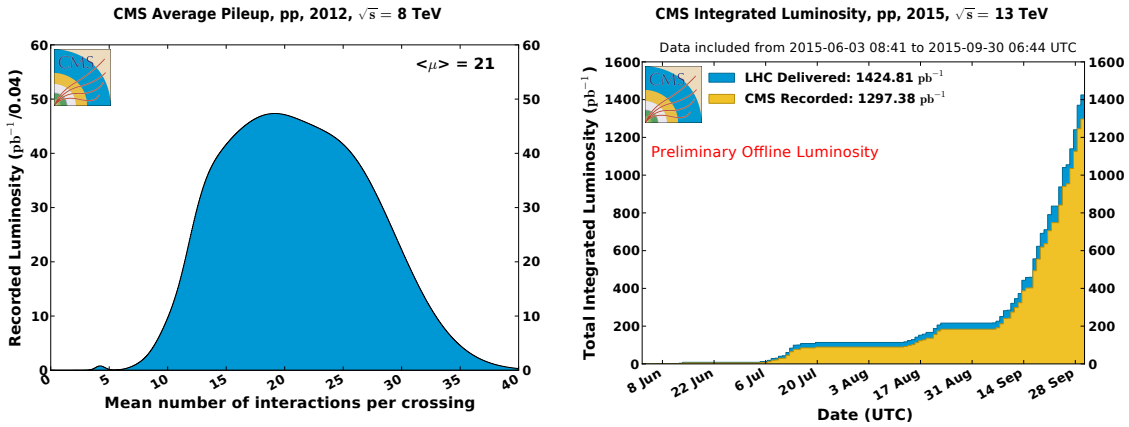

Figure 1.3: Mean number of interactions per bunch crossing in data collected in the 2012 by CMS experiment (left). Cumulative luminosity versus day (right) delivered by LHC (blue) during stable beams and for p-p collisions at $\sqrt{s}$ = 13 TeV in 2015; the off-line luminosity recorded by the CMS experiment is also reported (orange) [14].

1.2 The Compact Muon Solenoid

The Compact Muon Solenoid (CMS) experiment is one of the four main experiments that operate at the LHC at CERN [11]. It is placed along the LHC tunnel in the experimental cavern called *P5*, diametrically opposite to the injection system. It has been conceived to study proton-proton and lead-lead collisions at a centre-of-mass energy of 14 TeV (5.5 TeV nucleon-nucleon) and at luminosities up to 10^{34} cm$^{-2}s^{-1}$ (10^{27} cm$^{-2}s^{-1}$).

The CMS experiment is composed by a complex structure of different type of sub-detectors covering the whole solid angle around the beam pipe, as shown in Fig 1.4. At the core of the CMS detector sits the high magnetic field superconducting solenoid surrounding a silicon pixel and strip tracker, a lead-tungstate scintillating-crystals electromagnetic calorimeter, and a brass-scintillator sampling hadron calorimeter. The iron yoke of the flux-return is instrumented with stations of muon detectors covering most of the 4π solid angle. Forward sampling calorimeters cover low angle regions and assure very good hermeticity. The overall dimensions of the CMS detector are a length of 21.6 m, a diameter of 14.6 m and a total weight of 12500 t. The CMS experiment has been designed to have peculiar properties such as: high muon identification efficiency and muon p_T resolution in an wide kinematic region; very good reconstruction efficiency for charged particle and precise reconstruction of primary and secondary vertex; high photon energy resolution and missing energy reconstruction efficiencies.

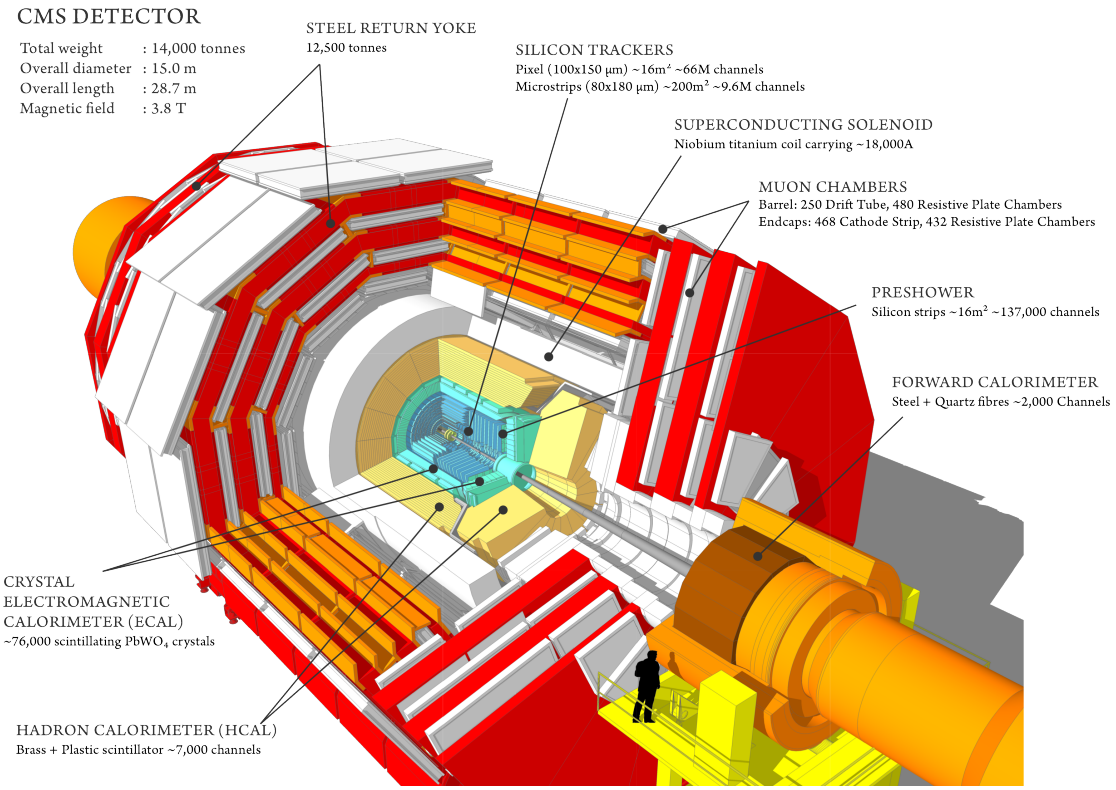

Figure 1.4: View of the CMS experiment and its sub-detectors.

1.2.1 CMS coordinates system

The CMS experiment coordinate system is reported in Fig. 1.5. The origin is fixed at the centre of the detector, in the nominal beams interaction point. The z-axis points along the direction of the counter-clockwise beam, the transverse plane is perpendicular to the beam and the y-axis points on the surface over the detector. The polar coordinates $r - \phi$ are defined in the transverse plane xy; ϕ is the azimuthal angle, θ is the polar angle, and the pseudo-rapidity is defined as $\eta = -ln\, tan(\theta/2)$. This coordinate identifies regions of the experiment along the longitudinal plane where differences in the placement of the detectors occur, *e.g.*, the inner tracking system covers a region up to $|\eta| < 2.5$, the solenoid is extends up to $|\eta| < 1.2$. In general, for each sub-detector a central region in $|\eta|$ is defined as *barrel*, while the two remaining solid angles are known as *endcaps*. The $|\eta|$ range of these two regions depends on the distance of the sub-detector system from the beam line. As for the physical variable convention, the transverse momentum (p_T) and the transverse energy (E_T) are calculated using their components along x and y axis.

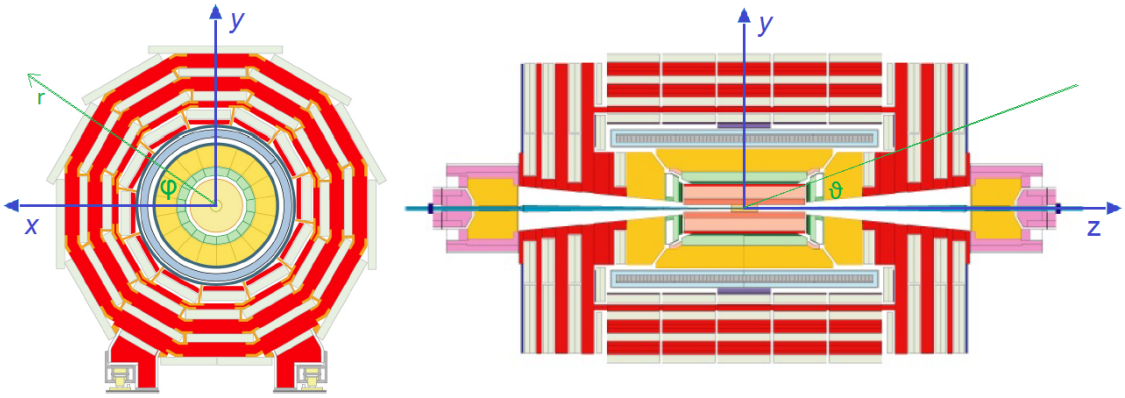

Figure 1.5: CMS transversal (left) and longitudinal (right) sections with relative coordinate system.

1.2.2 Superconducting solenoid

The CMS superconducting magnet has been designed to reach a 3.8 T field in a free cold bore of 6 m diameter and 12.5 m length with a stored energy of 2.6 GJ at full current [17]. The cold bore is refrigerated with a helium refrigeration plant and it operates at 4.5 K. The flux is returned through a 10000 t yoke comprising 5 wheels and 2 endcaps with three disks each. The distinctive feature of the 220 t cold mass is the 4-layer winding made from a stabilised reinforced $NbTi$ conductor, see Fig. 1.6. The solenoid has in fact been designed as a extremely compact element, to allow the placement of the muon detector system in the return yoke regions. Thus, the ratio between stored energy and cold mass is high (11.6 $\frac{KJ}{kg}$), causing a large mechanical deformation (0.15%) during energising, well beyond the values of previous solenoidal detector magnets. The CMS magnet has been successfully tested and commissioned during autumn 2006 and it has been set to provide a 3.8 T field in normal working conditions.

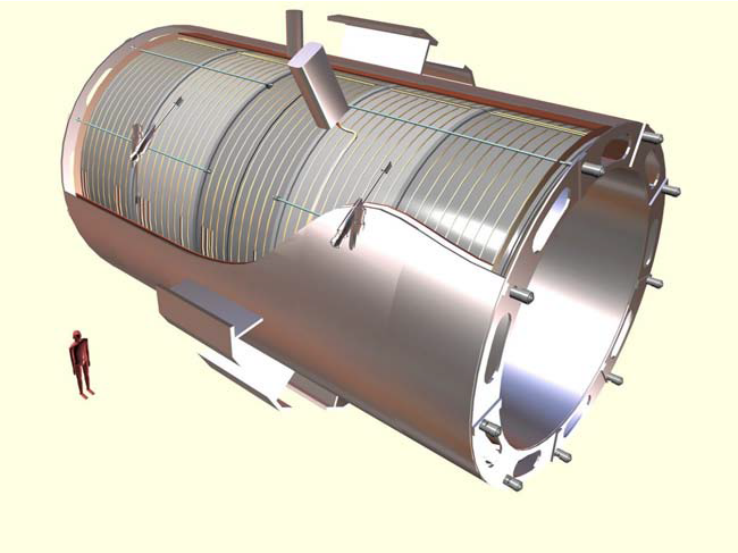

Figure 1.6: Schematic view of the 5 modules composing the cold mass inside the cryostat of the CMS superconducting solenoid.

1.2.3 Inner tracking system

The inner tracking system of CMS [18] [19] is designed to provide a precise and efficient measurement of the trajectories of charged particles emerging from the LHC collisions, as well as a precise reconstruction of primary and secondary vertices. It surrounds the beam pipe, which coincides with the z-axis of the CMS experiment, and has a length of 5.8 m and a diameter of 2.5 m.

The tracking system is designed to operate inside the magnetic field of 3.8 T, provided by the CMS solenoid, and at the LHC design luminosity of 10^{34} cm$^{-2}s^{-1}$. At this luminosity, an average of 1000 particles are expected from more than 20 overlapping proton-proton interactions traversing the tracker for each bunch crossing, i.e. every 25 ns. Therefore, a high granularity and fast response is required for the detector technology to get a high tracking efficiency. In parallel, the inner part of the tracking system needs to be extremely radiation hard to face this intense particle flux. As a final requirement, the material budget of the tracking system has to be as low as possible in order to avoid a worsening of the tracking efficiency and resolution due to material interaction effects of the charged particle, such as multiple scattering, bremsstrahlung, photon conversion or nuclear interactions. These requirements on granularity, speed and radiation hardness lead to a tracker design entirely based on silicon detector technology [20].

The CMS tracker can be divided into two main sub-detectors: a pixel detector in the innermost region with three barrel layers at radii between 4.4 cm and 10.2 cm from the beams interaction point, and a silicon strip tracker with 4 plus 6 barrel detection layers extending outwards to a radius of 1.1 m (Fig. 1.7). Each system is completed by endcaps which consist of 2 disks in the pixel detector and 3 plus 9 disks in the strip tracker on each side of the barrel, extending the acceptance of the tracker up to $|\eta| < 2.5$. With about 200 m^2 of active silicon area the CMS tracker is the largest silicon tracker ever built.

The CMS tracker is composed of 1440 pixel and 15 148 strip detector modules, which imply a high power density of the on-detector electronics that, in turn, requires an efficient cooling. The original design CO_2 distributed cooling system allowed the whole tracker system to be operated at $+4^{\circ}$ for the LHC Run. Several improvements have been

implemented after the end of the LHC Run 1 and an operative temperature of -15° is currently maintained by the upgraded cooling system and to the external thermal shielding, visible in Fig. 1.8.

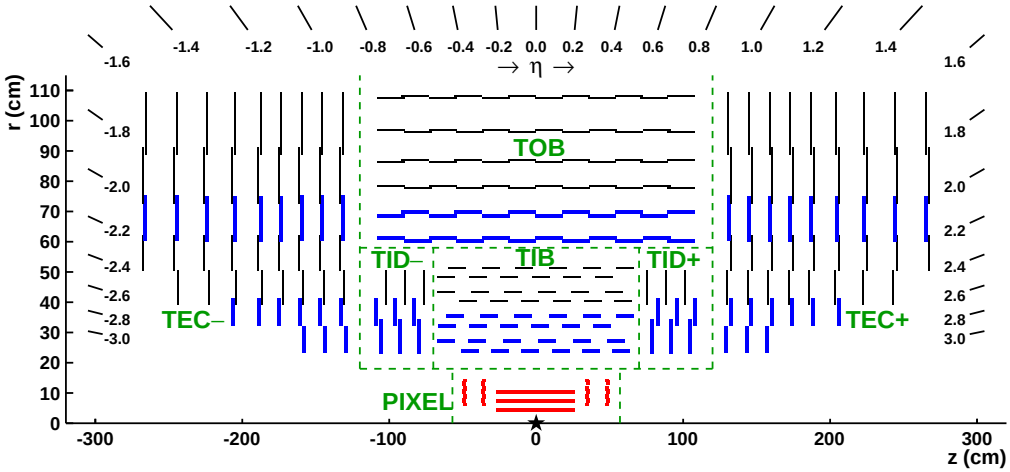

Figure 1.7: Transverse section of half of the CMS Tracker system; the different detector types are indicated.

1.2.3.1 Pixel detector

The pixel detector is the innermost detector of the whole CMS experiment, designed to provide high granularity and radiation hardness [21]. It is composed by 1440 silicon pixel detectors for a total of 66 million pixels which cover an area of about 1 m^2. The CMS pixel detector can be divided into a Barrel region (BPIX) and a Forward region (FPIX). Those two regions of the detector are mechanically and electrically separated. The BPIX is composed by three identical cylindrical layers placed around the the beam pipe at different distances (4.4, 7.3, 10.2 cm), see Fig. 1.9, while the FPIX is made by two endcap disks, placed at both side of the BPIX transversally to the beam axis at 34.5 and 46.5 cm from the nominal interaction point. The placement of the two regions provides a three-hit coverage for all tracks over the pseudorapidity range up to $|\eta| = 2.5$. The three hits allow a good estimation of the track parameters, thus the information from the pixel detector is used in the on-line event selection.

The unitary element of the detector is the module, composed by a silicon sensor electrically connected to 16 Read-Out Chips (ROCs) via a *bump-bonding* system, as shown in Fig. 1.10. A print board (HDI) is glued on top of the sensor and electrically connected to the ROCs to handle the I/O communication with them and to provide a unique interface to the external Front-End electronics. The module size is equal to 11×50 cm for the whole BPIX, the pixel size is 100×150 μm^2 and the sensor is read-out by 16 chips. The spatial resolution for the BPIX modules is about 10 μm in the transverse plane and 30 μm in the longitudinal plane, as shown in Fig. 1.11. The FPIX present modules with different shapes, and different number of ROCs each, since they are placed on trapezoidal petals on the disks; the petals are tilted by 20 degrees in a turbine-like geometry to induce charge sharing between pixels and achieve a spatial resolution of about 20 μm.

The sensor is 285 μm thick with a planar $n^+ - in - n$ pixel design. The pixels are formed

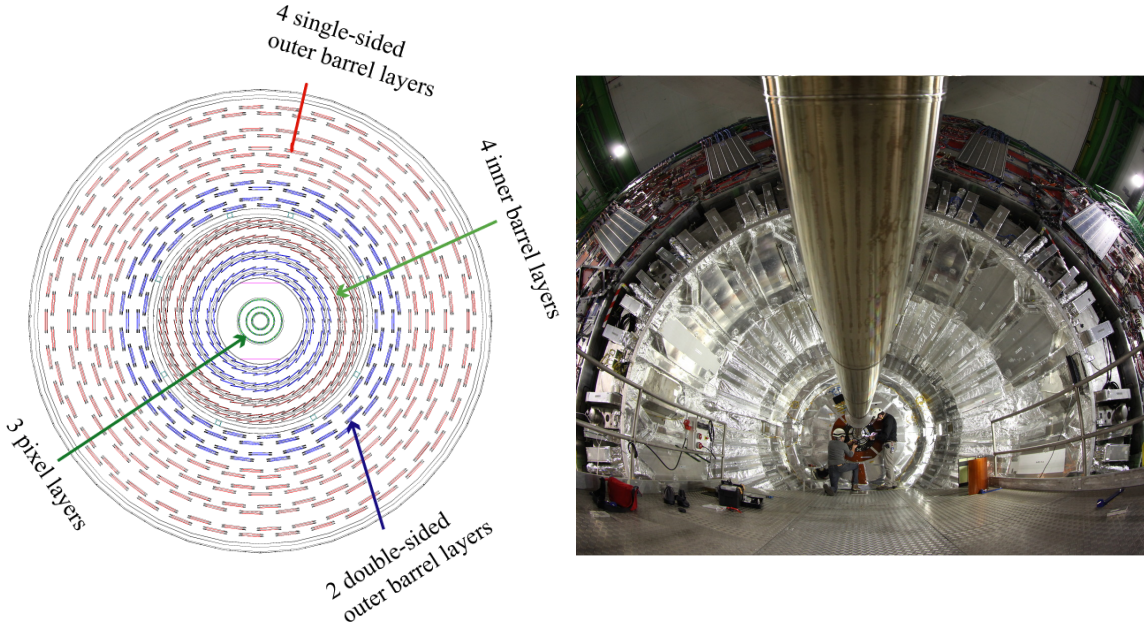

Figure 1.8: Scheme of the transverse section of the Tracker Inner System in the barrel region (left); frontal picture of a slice of the CMS detector before the LHC Run 2 start (right); the whole tracker system presents a thermal shielding to improve the performance of the distributed cooling system; the beam pipe going through the tracker is visible on the foreground.

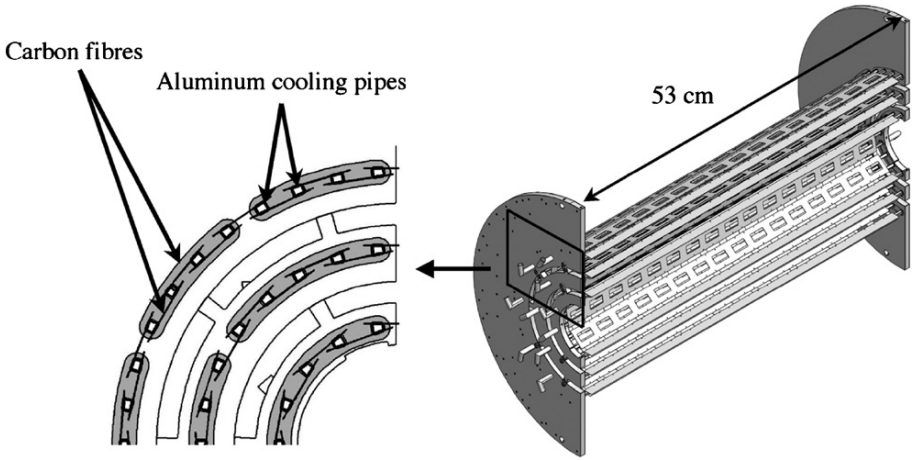

Figure 1.9: Schematics of the CMS BPIX system and its section with details of the cooling pipes and carbon structures on which the modules are mounted.

by high dose n-implants placed into a highly resistive n-substrate and the junction is formed with a p-implant on the back-side. The passage of a ionizing particle through the depleted region of the sensor lead to the release of charge carries which are then collected by the n-implant, as shown in Fig. 1.10 and described in [22]. The $n^+ - in - n$ design implies the collection of electrons which present a higher mobility compared to holes. This leads to a faster collection and also to a larger Lorentz drift (caused by the CMS magnetic field). Thus, the carriers do not follow the electric field lines to the collection electrodes, but are deflected by the Lorentz force and shared among pixels. The charge sharing is one of the required feature of the CMS pixel detector since it improves the position resolution. A single-pixel hits position resolution is given by the pitch divided by $\sqrt{12}$, while two-pixel clusters and interpolation allow a much better resolution, limited only by fluctuations of the charge deposition. Thus, the pixel cell size (100×150 μm) and its design have been chosen to maximize the presence of two-pixels clusters. This pixel based readout ensures low cell occupancy (order 10^{-4} per pixel with p-p collision) and a spatial resolution of about 10 μm in the r - ϕ plane and 15 μm in the z coordinate.

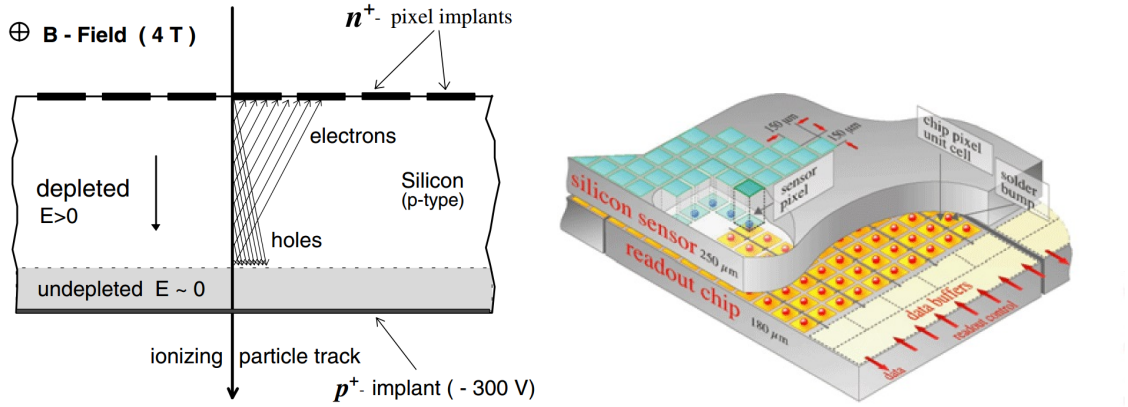

Figure 1.10: Schematic representation of the section of a silicon sensor (left), the charge induction is highlighted [22]. Scheme of a corner of the CMS pixel detector module (right), the red point are the bump-bonds connection between ROC and sensor pixels.

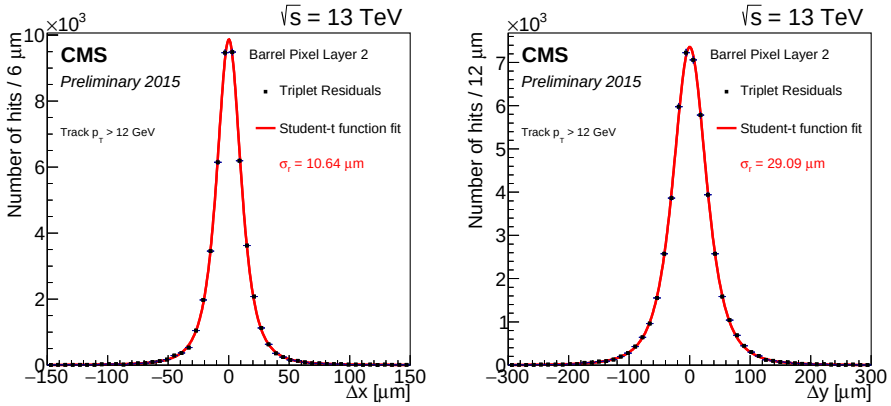

Figure 1.11: Distribution of hit residuals on pixel barrel layer 2 in the transverse (left) and longitudinal (right) direction with respect to the beam. The distributions are fitted with a student's t-function for which sigma is shown on the plot [23].

The ROC is a custom-designed chip, based on 250 nm process, which handles the readout of the signals coming from 4160 pixels (52 $\times$ 80), with a dedicated readout unit cell per each pixel of the sensor. The readout is 40 MHz analog and it is based on a double column system composed by data buffers and timestamps placed in the ROC periphery, at the bottom of the pixel matrix.

Each layers and disks of the pixel detector provide an excellent hit efficiency as shown in Fig. 1.12. A degradation of this performance is expected with the increment of instantaneous luminosity and PU. This is mainly due to the designed structure of the ROC. Due to the proximity to the interaction point, the absorbed dose of the pixel detector is high and, after several years of operation, radiation-induced effects do lower the detector performances. To prevent this, radiation hardness techniques have been used in the design of the pixel sensor and ROC. However, the radiation effects on sensor, such as displacement damages [24], lead to a lower charge collection and thus to the necessity of bias voltage increment with consequent problems due to the leakage current.

The tracking efficiency in the pixel detector is expected to be reduced by an up to 10% factor within the end of the LHC Run 2. A first action to overcome this problem has been the cooling of the system to operate at $-15°C$, to reduce the leakage current in the sensor and thus to get a lower noise. The second action will be the complete substitution of the pixel detector with an upgraded version, planned for the beginning of 2017 and described in details in Chapter 2.

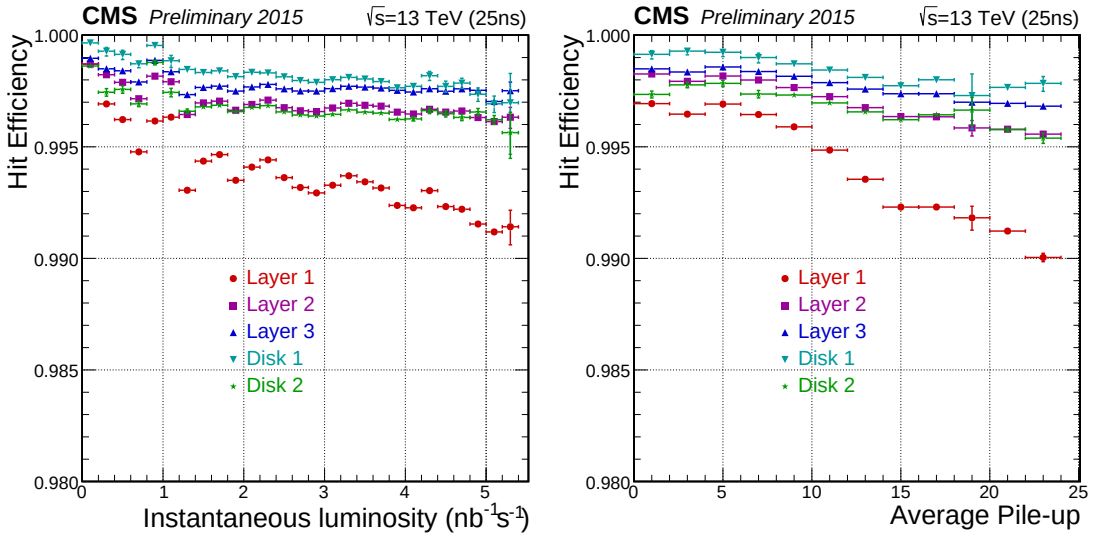

Figure 1.12: Hit efficiency versus instantaneous luminosity (left) and versus the average number of inelastic p-p collisions (right) for pixel barrel layers and forward disks. Measurements are from 2015 data $\sqrt{s}$ = 13 TeV and 25 ns bunch spacing [23].

1.2.3.2 Strip detector

All the tracker system outside the pixel detector is composed by silicon strip detector [25]. The flux of particle in this area is considerably lower than the pixel region and the design constraints on occupancy are less strict, thus a strip detector has been chosen [26]. From r = 20 cm to r = 130 cm, four types (TIB, TID, TOB, TEC) of silicon strip detectors are placed.

The strip detector is based on single-sided and double-sided microstrip detectors with

AC-coupled p-type strips in an n-type bulk, see Fig. 1.13. The wafer thickness is 320 μm or 500 μm, depending on the distance of the detector from the interaction points. A custom chip is placed on one or both sides of the sensor to handle the strip based readout of the sensor.

The whole strip detector presents a total of 9.6 M channels. The strip length is equal in the whole detector while the strip pitch varies all over the tracker detector from the inner to the outer layers (from 80 μm to 205 μm). This variation is related to the distance from the interaction point, thus to the different particle flux, and mainly identifies the 4 detector topologies of the CMS strip detector (Fig. 1.7):

- Tracker Inner Barrel (TIB): placed at a distance from the beam axis of 20 $<$ r $<$ 55 cm, it covers a 4π region up to $|z| < 65$ cm; composed by four layers with silicon sensor of 320 μm thickness; the first two layers allow measurements in both the planes $r\phi$ and rz; the resolution is between 23 and 34 μm in r and ϕ, while it is equal to 230 μm in z.
- Tracker Inner Disk (TID): complementary to the TIB, it covers the region $65 < |z| < 110$ cm with 3 disk of micro-strip detectors per side, placed transversally to the beam axis; the strips are centred on the beam axis and their width varies along the radius.
- Tracker Outer Barrel (TOB): placed outside the TIB and TID, at a distance from the beam line of $r > 55$ cm up to r = 130 cm; 6 layers with silicon sensor of 500 μm thickness, in $|z| < 110$ cm horizontal range; bigger silicon strip (25 cm $\times$ 120 μm per cell) that provide a coarse granularity; the first two layers allow measurements in both the planes $r\phi$ and rz; resolution is between 35 and 52 μm in r and ϕ while it is equal to 530 μm in z.
- Tracker End Cap (TEC): 9 rings centred on the beam axis and placed on both side of the Barrel at 120 cm $< |z| <$ 280 cm; as for the TID they present strips with a different width along the radius.

The strip detectors are read-out by a 250 nm CMOS Readout Chip, called *APV* [27]. Each APV handles 128 strip channels with a read-out rate of 100 kHz.

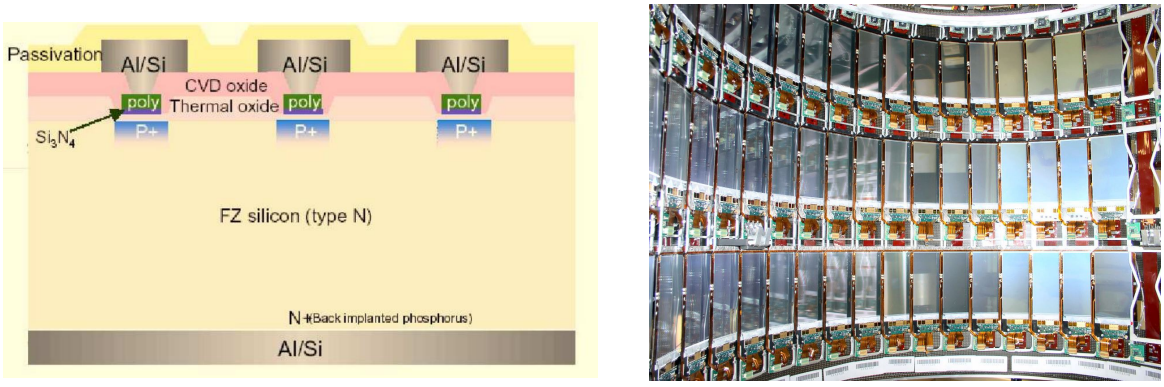

Figure 1.13: Schematic view of the transverse section of a strip detector sensor [28] (left); photography of the TIB Layer 3, strip sensor and relative readout electronics are clearly visible.

1.2.4 Electromagnetic calorimeter

The CMS Electromagnetic Calorimeter (ECAL) is designed to measure the energy of electrons and photons still inside the solenoid. It is placed immediately outside the

tracker and it covers a fiducial region up to $|\eta| < 2.5$. ECAL is a homogeneous calorimeters made of 74,848 lead-tungstate ($PbWO_4$) crystals, a transparent material denser than iron (8.3 g/cm^3). These crystals are characterized by a low radiation length $X_0 = 0.89$ cm, a Molière radius RM of 2.19 cm and fast response (80% of light emitted within 25 ns). The electromagnetic shower is thus contained in a limited regions and it allows the ECAL to be placed in the compact magnetic coil. The light from the crystals ($\sim 30\ \gamma$ per MeV) is collected by high gain photomultipliers designed to work inside magnetic field. ECAL is composed by 3 main regions (see Fig. 1.14), with different detectors types:

- Barrel ECAL: placed at r = 1.29 m, it covers a pseudorapidity region of $|\eta| < 1.48$; the crystals have a front face area of $2.2 \times 2.2 cm^2$, a length of 23 cm (25.8 X_0) and are grouped into 36 supermodules; the light is read by avalanche silicon photodiode (APD).
- Endcap ECAL: two disks placed at $|z| = 314$ cm which cover the $1.48 < |\eta| < 3$ regions; the crystals have a $2.47 \times 2.47\, cm^2$ front face, a 22 cm length and are linked to foto-triodi (VPT), more radiation-hardness than standard APD; each endcap is divided into two halves (DEE) and the crystal are mechanically grouped into 5×5 super-crystals.
- Pre-shower: placed in front of the endcaps at $1.653 < |\eta| < 2.6$; it is made of two disks of lead absorber of $2X_0$ and $3X_0$, and of two planes of silicon strip detectors; it supplies the larger granularity in the endcap regions and it allows the rejection of photon pairs from π_0 decays thanks mainly to a better discrimination of electron and photon.

The ECAL energy resolution can be parametrized by three different contributions:

$$\frac{\sigma_E}{E} = \frac{a}{\sqrt{E}} \oplus \frac{b}{E} \oplus c \tag{1.3}$$

where the first term is statistical in nature and contains fluctuation in showering and in the amplification through photodiodes ($a = 1.8\%$), the second considers electronic noise and pileup ($b = 4\%$) and the last term is related to calibration ($c = 0.5\%$). The latest measurements of ECAL performances can be found at [29].

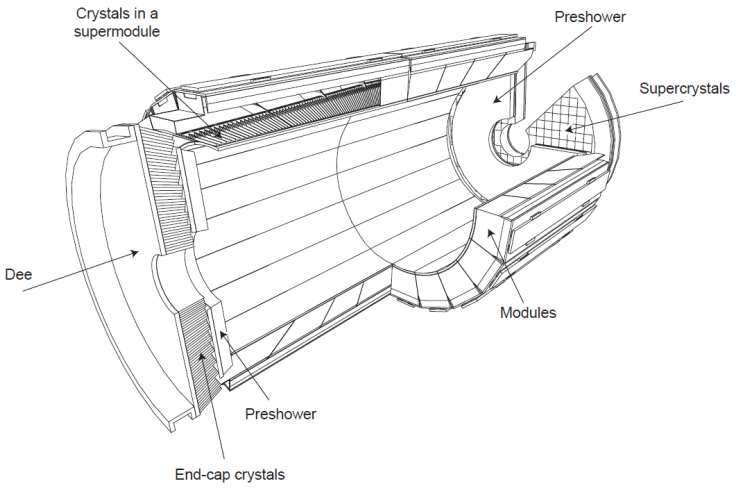

Figure 1.14: Layout of the CMS electromagnetic calorimeter (ECAL) and its 3 components.

1.2.5 Hadron calorimeter

The hadron calorimeter (HCAL) is a sampling calorimeter whose active elements are plastic scintillators interleaved with brass absorber plates and read out by wavelength-shifter fibers. Brass has a short interaction length and it is non-magnetic, thus it fits perfectly with the CMS needs. The thickness of the absorber layers is 60 mm in the barrel and 80 mm in the endcaps.

HCAL is placed just outside ECAL and inside the magnet coil. The design of the calorimeter is thus driven by the space restrictions, covering a $|\eta| < 1.3$ region in the barrel (HB) and the $1.3 < |\eta| < 3$ region in the endcaps (HE). The barrel depth goes from 5.46 interaction lengths at $\eta \sim 0$ to 10.8 at $\eta \sim 1.3$, while the endcaps coincide with an average of 11 interaction lengths. The calorimeter is segmented and arranged in towers of 0.087×0.087 in $\eta - \phi$ for $|\eta| < 1.6$ and 0.17×0.17 elsewhere, each tower matching a set of 5×5 ECAL crystals. The photodetection readout is based on multi-channel hybrid photodiodes, able to operate in a high magnetic field. They give an amplified response proportional to the original signal for a large range of particle energies.

Since HCAL plays also an important role in the reconstruction of missing energy, it is necessary to have a high hermeticity and to cover the greatest possible portion of the solid angle. Therefore the system is completed by a hadron forward calorimeter (HF), a steel/quartzfiber Cherenkov calorimeter placed outside the magnet return yokes at 11 m from the interaction point with a total coverage of $3 < |\eta| < 5.3$. Moreover, an outer hadronic calorimeter (HO), composed by an array of scintillators, is placed in the barrel region outside the magnet in order to enhance the containment of high-energy jets in the central region of the detector. The HCAL energy resolution (expressed in GeV) is $\sigma/E \sim (a/\sqrt{E} \oplus 5\%)$ where a is 65% in the barrel, 85% in the endcaps and 100% in the forward calorimeter.

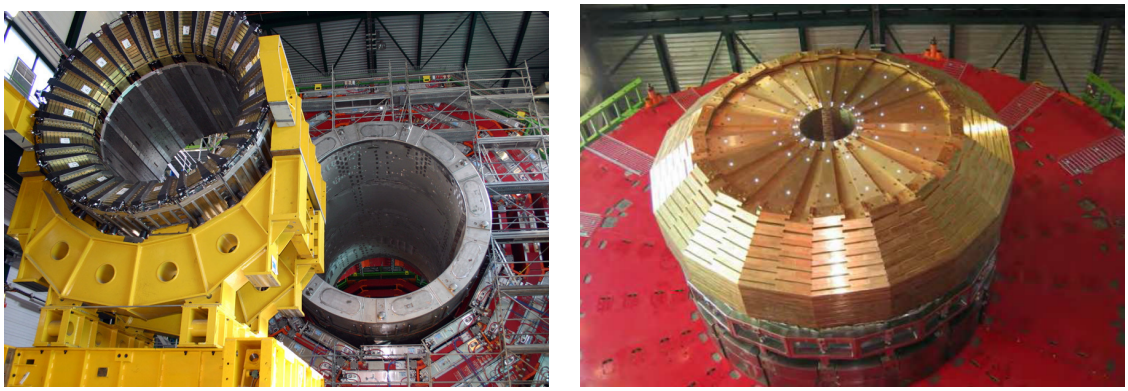

Figure 1.15: HCAL barrel before insertion in the magnet coil (left) and HE (right).

1.2.6 The muon system

The CMS muon detector is the unique system of CMS that is entirely placed outside the magnet coil and the calorimeters. It is located in the steel return yoke of the solenoid, covering the pseudorapidity region $|\eta| < 2.4$. This is possible because muons are scarcely affected by this huge material budget. The position of the detectors system has two important consequences: the coil provides a shield from electromagnetic and hadronic particles that are not contained inside the calorimeters and the yoke provides a magnetic

field between consecutive muon stations, allowing a momentum measurement independent from the inner tracker.

The muon system is designed for three major functions: robust and fast identification of muons, good resolution of momentum measurement, and integration to a fast and reliable trigger system. The gaseous detectors has been chosen as muon detectors since they are robust and with a relative fast response. Moreover, the area to be covered is huge and a gaseous detector system allows to reduce the cost and the amount of readout channels.

The muon system is thus composed of three types of gaseous detectors located inside the empty volumes of the iron yoke, and arranged in barrel and end-cap sections, as shown in Fig. 1.16. The choice of different detector topologies lies essentially in the different particle rate expected in the regions outside the solenoid. The forward region is where the flux of hadron punch-through and radiation is higher and the magnetic field is less uniform. In the barrel region instead, the particle rate and the residual magnetic field are low thus slower detectors, such as the drift tubes, can be used. The three different muon system sub-detectors are:

- Drift Tubes (DT): four layers of drift tube chambers are placed in the barrel region ($|\eta| < 1.2$); the chamber segmentation follows the iron yoke structure, consisting of 5 wheels along the z axis, each one divided into 12 azimuthal sectors; cells in consecutive layers are shifted by half of their width in order to avoid un-instrumented regions. Each DT chamber, on average 2×2.5 m in size, consists of 12 aluminium layers, arranged in three groups of four, each with up to 60 tubes. The middle group measures the coordinate along the direction parallel to the beam and the two outside groups measure the perpendicular coordinate. Each one of the 250 DT chambers has a resolution of ~ 100 μm in $r\phi$ and up to 150 μm in z, and can measure the particle direction with ~ 1 mrad accuracy [30].
- Cathode Strip Chambers (CSC): 540 CSC are used in the two endcaps ($0.8 < |\eta| < 2.4$) [] ; the chambers are arranged in 4 disks per endcaps divided in concentric rings (3 rings in the innermost station, 2 in the others). The cathode strips are oriented radially and provide precise measurement in the bending plane; the anode wires run approximately perpendicular to the strips and are read out to measure the pseudorapidity and the beam-crossing time of a muon. Each chamber has a spatial resolution of about 200 mm in r, and 75×150 mm in the $r\phi$ coordinate [30].
- Resistive Plate Chambers (RPC): in both the barrel and the endcaps, a system of 912 Resistive Plate Chambers is installed, ensuring redundancy to the measurement []; RPCs, operated in the avalanche mode, provide a rougher spatial resolution than DTs and CSCs, but the fast response with a good time resolution (1 ns) is used for triggering purposes.

1.2.7 Event reconstruction

The high segmentation of the CMS detector and the presence of the various type of subdetectors allow a good reconstruction efficiency for the different particles but require also the development of algorithms to group all the information together and to get the best efficiency in particle identification per each event.

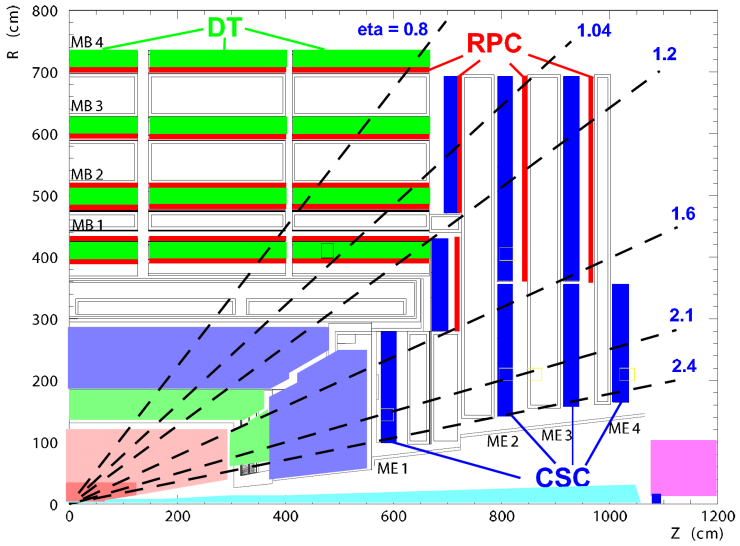

Figure 1.16: A longitudinal view of one quarter of the CMS experiment; the three muon detectors detector types are highlighted.

1.2.7.1 Track reconstruction

The charged track reconstruction at CMS [31] is based essentially on information coming from the inner tracker system. Despite the good performances and resolutions of the detectors, the track reconstruction is challenging due to huge tracks (and thus hits) density, to the multiple vertices present in each bunch crossing and to the amount of detector material (Fig. 1.17) leading to multiple scattering, energy loss and nuclear interactions.

The trajectories of charged particles are reconstructed through the so-called Iterative tracking which consists in multiple iterations of the Combinatorial Track Finder algorithm (CTF), based on the combinatorial Kalman Filter technique [32]. The algorithm starts searching for tracks of relative large p_T and produced near the interaction region. Then, hits associated to high quality tracks are iteratively removed from the input list to reduce the combinatorial complexity of the next iterations and to allow the more difficult reconstruction of low p_T or displaced tracks. Each iteration of the CTF algorithm is made of four steps:

- Seed Generation: provides an estimate of the helix parameters and their uncertainty by using only pairs or triplets of hits compatible with the hypothesis of a track coming from the p-p interaction region. Track candidates are best seeded from hits in the pixel detector (inner detector) because of the low occupancy, high efficiency and unambiguous 3-dimensional position information. This also facilitates reconstruction of low-momentum tracks that are deflected by the strong magnetic field before reaching the outer part of the tracker.
- Track Finding: the Kalman Filter is used to associate the tracks. A first trajectory, starting from the seed, is extrapolated to the next layer of the detector along the expected flight path of a charged particle, by selecting a compatible hit from the next detector layer and updating the parameters. In case multiple compatible hits are found when extrapolating the helix to a single layer, the algorithm creates one trajectory candidate for each hit and they are propagated independently. Once the track is completed another search is performed backward starting from the outermost hit to improve the hit collection efficiency.

This results to improve the accuracy of the p_T and impact parameter measurement by 0.5% and 1% respectively.

- Track Fitting: once all the track candidate hits are collected, the trajectory is refitted using the Kalman Filter to determine the most accurate estimate of the helix parameters. Compatible hits are assigned to the track on the basis of the χ^2 between the predicted and measured positions. Spurious hits (outlier) wrongly associated to the track are also checked. This results in a better discrimination against combinatorial fakes, and further improves the impact parameter and p_T resolution. The applied pattern recognition maximizes the efficiency and leads to a significant fraction of fake tracks (up to some 10%).
- Track Filters: a selection is performed to reduce the fake rate, mainly through the usage of multivariate analysis techniques; quality requirements on the number of layers that have hits, the track normalized χ^2, and the longitudinal distance from the closest vertex are applied; the selection is dependent on the number of reconstructed hits in the track, as tracks with more hits have a lower fake rate, which allows for lower thresholds.

Once all steps of iterative tracking have been performed, the output collections of the different steps are merged. In case two tracks share more than 50 % of their hits, the lower-quality track is discarded. Two additional iterations have been designed to recover the missing muon-track in the tracker (outside-in seeded) and re-reconstruct muon-tagged tracks with looser requirements (inside-out seeded). An additional iterative tracking step targeting the core of jets (JetCore) reconstructed with E_T >100 in calorimeters is run at the end of the track reconstruction. The tracking reconstruction efficiency has been measured to be about 100% for the isolated muons in the $|\eta| < 2.5$ range, from 98% to 89% for 10 GeV pions and over 92% for >10 GeV electrons, as shown in Fig. 1.17.

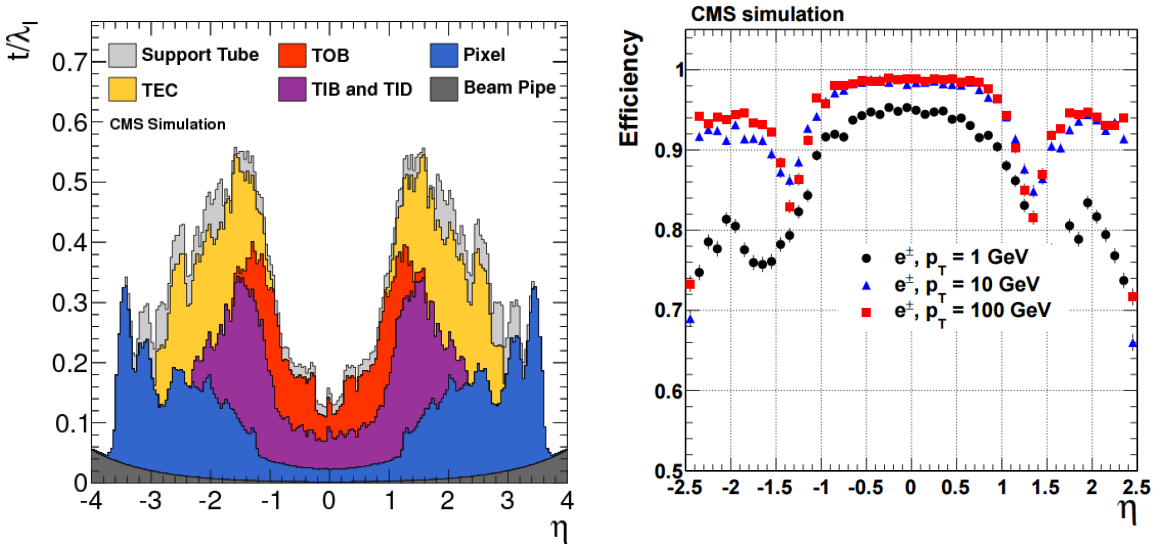

Figure 1.17: Material budget of the CMS tracker in units of hadronic interaction lengths λ_I (left). Track reconstruction efficiencies for electrons (right) passing the high-purity quality requirements; efficiency decrease for $|\eta| = 1.3$ is due a not complete overlap of the different detector systems [31].

1.2.7.2 Interaction vertex reconstruction

The position of the vertices resulting from the p-p interactions in the same buch crossing (*primary vertices*) and those originated by heavy flavours and long-lived particles (*secondary vertices*) is determined through a three step procedure using the available reconstructed tracks.

The first step is the selection of tracks consistent with being produced promptly in the primary interaction region. These are then clustered using a deterministic annealing (DA) algorithm [33], based on the impact parameter along the z coordinate, followed by the application of an Adaptive Vertex Fitter [34]. Thanks to the DA algorithm, vertices are resolved with separations about 1 mm, appropriate for a multiplicity of interactions per bunch crossing up to 20, as the longitudinal RMS spread of the luminous region is about 6 cm. The adaptive vertex fitter allows then to compute the best estimate of vertex parameters. This algorithm addresses the issue of secondaries and fake tracks in the cluster by iteratively down-weighting the tracks which are not compatible with the common vertex being fitted. The primary vertex originating the hard scattering is chosen as the vertex with highest sum of p_T^2 of the clustered tracks.

The primary vertex spatial resolution depends on the event topology and on the number of tracks related to the vertex, as shown in Fig. 1.18. For minimum-bias events, the resolutions in x and z are, respectively, less than 20 μm and 25 μm, for primary vertices reconstructed using at least 50 tracks. The resolution is better for the jet-enriched sample across the full range of the number of tracks used to fit the vertex, approaching 10 μm in x and 12 μm in z for primary vertices using at least 50 tracks.

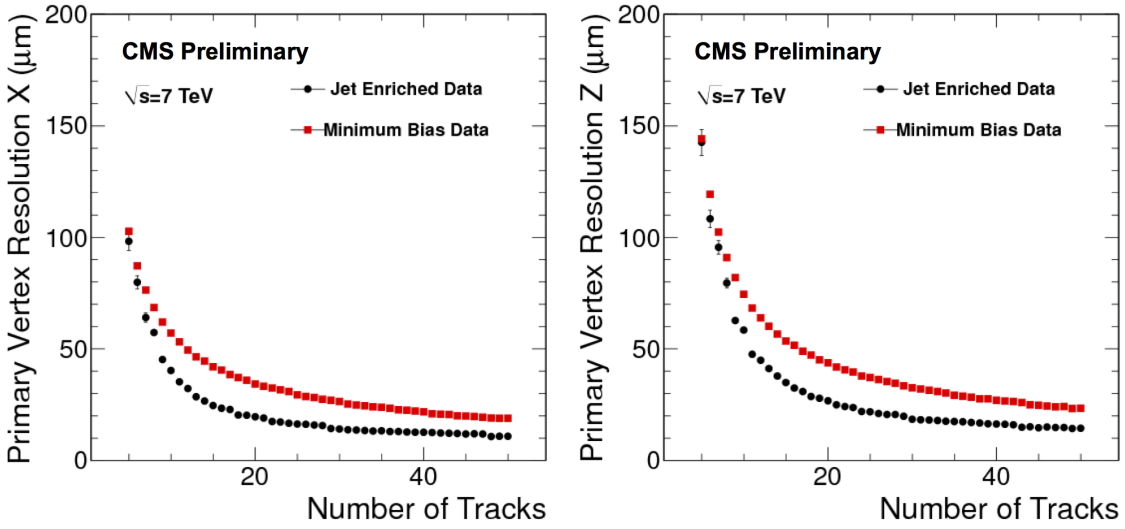

Figure 1.18: Primary-vertex resolution in x (left) and z (right) as a function of the number of tracks at the fitted vertex, for two kinds of events with different average track p_T values; the results in y is almost identical to the one in x [35].

1.2.7.3 Global event reconstruction

The global event reconstruction at CMS relies on the particle flow algorithm (PF) [36], [37], which reconstructs and identifies each individual particle with an optimized combination of information from the various elements of the CMS detector. The various type of particles provide different signals in the CMS sub-detectors, as shown in Fig. 1.19.

The particle flow reconstruction technique allows to analyse these different information and link them to reconstruct the complete track. The target of the PF is to get a full reconstruction of each single particle without getting a double counting from different sub-detectors. The association criteria is purely geometrical and the granularity of the reconstruction is dominated by the calorimeters one. The energy deposits and tracks are linked if their trajectory intersects one of the calorimetric cells, and likewise clusters in the ECAL pre-shower; ECAL and HCAL are linked if the cluster position is compatible in the η, ϕ plane between the extrapolated track position and the cluster position.

The charged hadrons are identified as tracks in the inner tracker and linked to calorimetric deposits if the particle p_T is large enough (> 750 MeV). If the tracker and calorimeter measurements are compatible, the best energy determination is obtained as a combination of the two, after accounting for non-linearities and zero-suppression effects. If instead an excess of calorimetric energy deposition is found with respect to the momentum of the associated track, or calorimetric deposits are not linked to any tracks, the energy is identified as coming from a photon or a neutral hadron. If the track momentum exceeds significantly the measured calorimetric energy, the particle is considered a minimum ionizing particle and is identified as a muon after satisfying very loose identification criteria. In this case, linking between tracks in the tracker and a muon tracks in the muon system is established and the momentum of muons is measured from the curvature of the corresponding track.

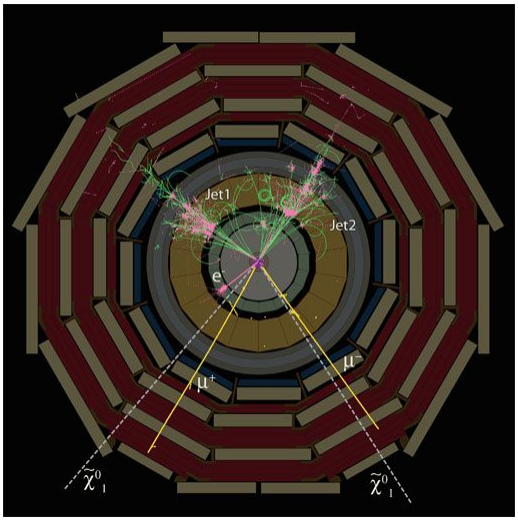

Figure 1.19: Representation of the CMS transverse section with reconstructed events superimposed; the simulated event shows the decay of a supersymmetric particle into: electron, muons, neutrinos and jets, produced by quarks.

1.2.8 Jets reconstruction

Because of QCD confinement [38], particles carrying a color charge cannot be observed free. Quarks and gluons interact with pairs of quarks and anti-quarks produced from the vacuum until the formation of stable colourless hadrons, the process is called hadronization. The heavy quarks undergo also a, so-called, fragmentation into lighter quarks. The totality of products of quark fragmentation and hadronization can be detected in tracking chambers and calorimeters and it is called *jet*. It starts from the interaction points and it is cone-distributed up to the calorimeters.

In p-p collision, due to the high probability of getting gluon-gluon interaction, most of the events are characterized by jets production, as shown in Fig. 1.19. The jet reconstruction depends on the capability to identify all the tracks related to that single jet, and the vertex from which the hadronization process started. A coarse jet reconstruction is based on the information from electromagnetic and hadronic calorimeter towers only, and provide the so-called *CaloJet*.

A more complete jet reconstruction is instead based on the PF objects (hence called *PF-Jets*), for example the *anti-k_T* clustering algorithm [39, 40].The anti-k_T is a sequential recombination jet algorithm, that merges pairs of particle candidates in order of increasing relative transverse momentum into jets, until a stopping requirement is achieved, typically when the distance between adjacent jets is greater than some value. The distance between two candidates i and j is defined as:

$$d_{ij} = min\left(\frac{1}{p_{Ti}^2}, \frac{1}{p_{Tj}^2}\right)\frac{\Delta R_{ij}^2}{R^2} \tag{1.4}$$

with $\Delta R_{ij}^2 = (\eta_i - \eta_j)^2 + (\phi_i - \phi_j)^2$. The use of p_T^{-2} in the distance metric is the anti-k_T peculiarity and it provides two features: the radiation around hard objects is clustered first; the soft particles tend to cluster with hard ones before they cluster among themselves. Thus, the algorithm produces conical jets of radius equal to the distance parameter (R) unless there are multiple hard objects separated by less than R. This weak dependence of the algorithm on the soft radiation is crucial and it is known as infra-red safety. The anti-k_T is also collinear safe, meaning that splitting an hard candidate in two or more collinear candidates with softer p_T does not change the result of the jet clustering. A value of R = 0.5 has been used in the LHC Run 1, while R = 0.4 is implemented for p-p collision at $\sqrt{s}$ = 13 TeV since more collimated jets are expected at higher $\sqrt{s}$.

The jet momentum is determined as the vectorial sum of all particle momenta in this jet (raw jets). At this stage, the reconstructed jet energy has a great uncertainty due to the several intrinsic limitations of the system, such as the non-linear response of the calorimeters, the detector segmentation, the presence of material in front of calorimeters, electronic noise, pile-up. The raw jets are thus corrected for several factors in order to obtain the energy value as close as possible to the true energy of the initial parton [41]. The corrections are applied in a multi-steps sequence including: the pileup and electronic noise effects removal, compensation of the variation of the jet response versus η, correction of the calorimetric energy response variation as a function of the jet p_T, residual correction coming from differences between data and simulation. The JEC computed for p-p collision at $\sqrt{s}$ = 7 TeV is reported in Fig. 1.20. The overall uncertainty on the jet energy scale for jets with $p_T > 30$ GeV is smaller than 3% in the barrel and 5% up to $|\eta| < 4.5$. Since measurements on data show that the jet energy resolution (JER) is not the same in data and MC, corrections are applied in simulation, smearing by about 5% jets in the barrel region, and up to 15% jets in the endcaps [41]. The resulting jet energy resolution (Fig. 1.20) is typically 15% at 10 GeV, 8% at 100 GeV, and 4% at 1 TeV. For the CaloJet instead, the jet energy resolution is about 40%, 12%, and 5% respectively [41]. Jets are also requested to pass loose identification criteria, in order to reject fake jets due to calorimeter noise, with more than 99% efficiency for true jets.

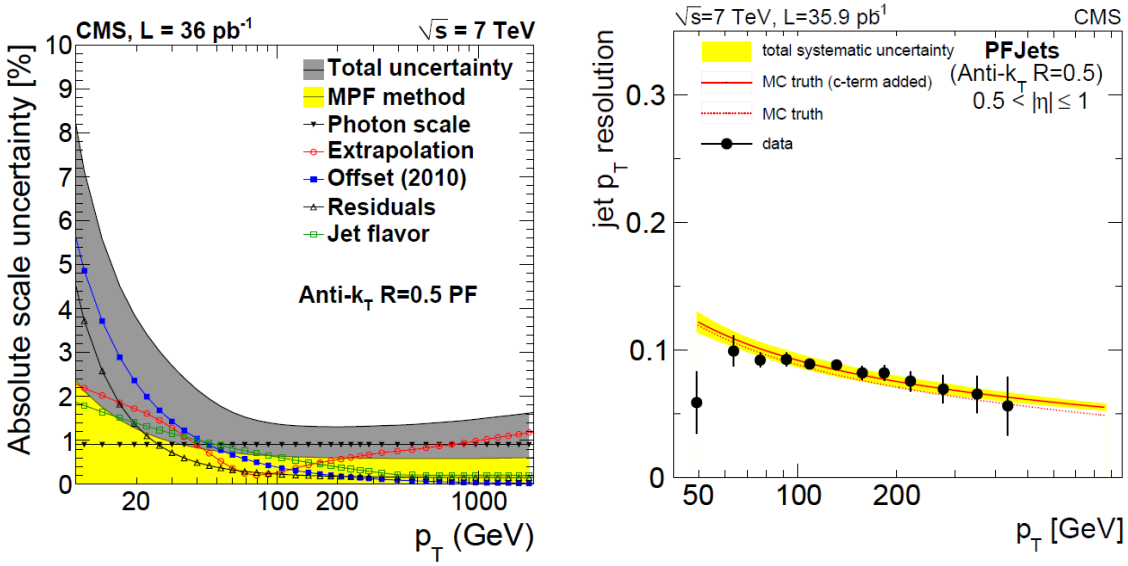

Figure 1.20: JEC uncertainties for each single source (left) and JER for PFJets in $0 < |\eta| < 0.5$ (right); data collected in 2011 at $\sqrt{s} = 7$ TeV are considered [41].

1.2.8.1 Identification of b-jets

At the LHC, the identification of jets originating from b quarks (*b-jet*) is important for searches for new physics and for the Higgs bosons search in the dominant $b\bar{b}$ decay mode. The ability to identify b-jets (*b-tagging*) accurately plays a fundamental role in reducing the overwhelming background coming from processes involving jets from gluons (g) and light-flavor quarks (u, d, s), and from c-quark fragmentation.

The jets originating from a b quark can be identified from the other thanks to the relative long lifetime of the b quark: $c\tau \sim 450$ μm. A b hadron with $p_T = 50$ GeV covers, on average, almost half a centimetre ($Lc \sim \gamma\tau$) before decaying. Thus, the particle coming from the b-quark decay (*daughters*) can have a sizable impact parameter with respect to the b quark point of origin. The impact parameter $d \sim L \sin\alpha \sim \gamma c\tau\alpha \sim c\tau$ is boost invariant (where α is the average opening angle of the decay products). The other properties on which the b-tagging can rely on are: a large mass (O(4-5 GeV)) and relatively large semileptonic branching ratios ($\sim$ 40%) of B hadron decays involve also muons or electrons.

These properties cause the b-jets to be wide, hence with high track multiplicity and large invariant mass. The tracks from a B hadron decay are typically produced with a non zero Impact Parameter (IP) with respect to the interaction point. Since, tracks from B hadron decays are mostly produced in a cone in the B hadron flight direction, one can approximate the B hadron flight direction with the jet direction and then search for tracks in the jet cone, see Fig. 1.21.

A variety of algorithms has been developed by the CMS collaboration to identify b-jets based on the B hadron properties just described. These algorithms use lower-level physics objects, mainly jets and charged tracks. Only the tracking detectors offer the spatial resolution needed to detect the significant decay length of B hadrons and thus the inner tracking system information is mainly used. Each algorithm associates a b-tag probability to each jet and three main working points are set on it looking at the rate of light jet misidentification. The loose operating point coincides with a 10% of light jet

misidentified as a b jet, the medium with a 1% misidentification and the tight with a 0.1%.

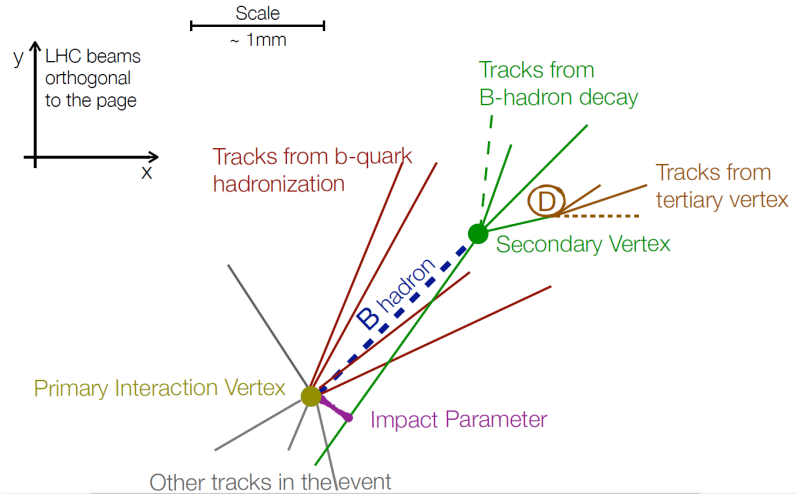

Figure 1.21: Representation of a b-hadron decay and relative properties.

1.2.8.1.1 Combined Secondary Vertex Algorithm The *Combined Secondary Vertex* (CSV) algorithm [42] is a vertex-based algorithm which collect in a single discriminator the information provided by all the possible variables, track IP included. This allows the algorithm to not be limited by the secondary vertex reconstruction efficiency. Jets are divided in three vertex-dependent exclusive categories: the presence of a reconstructed secondary vertex; at least two tracks with impact parameter significance larger than 2; none of the previous. A likelihood discriminator is built and trained separately on the three categories using the following set of variables:

- the 2D flight distance significance of the secondary vertex;
- the number of tracks in the jet
- the number of tracks associated to the secondary vertex
- the secondary vertex mass
- the ratio of the energy carried by tracks at the vertex with respect to all tracks in the jet;
- the pseudo-rapidity of the tracks at the vertex with respect to the jet axis;
- the 2D IP significance of the first track that raises the invariant mass above the charm threshold of 1.5 GeV when subsequently summing up tracks ordered by decreasing IP significance;
- the 3D signed IP significance for each track in the jet

The CSV has been used for the off-line b-jets selection in CMS during the LHC Run 1 and first attempts to exploit it in the on-line selection have been made. This algorithm provided the best performance expressed as b jet tagging efficiency versus c- or light-jet mis-tagging.

For the LHC Run 2, a second version of the algorithm has been implemented: Combined Secondary Vertex version 2 (CSVv2) [43]. This is an updated version of the CSV algorithm that combines the variables with a neural network instead of a likelihood ratio. In addition, the secondary vertex information is obtained with the *Inclusive Vertex Finder* algorithm. The performance of the CSVv2 has been measured using data recorded in

2015 at $\sqrt{s}$ = 13 TeV with a bunch spacing of 25 ns and for a total integrated luminosity of around 2.4 fb^{-1}. The three working points have been set to: 0.605 for the loose (CSVv2L), 0.890 for the medium (CSVv2M) and 0.970 for the tight (CSVv2T). A comparison between data and MC is shown in Fig. 1.22.

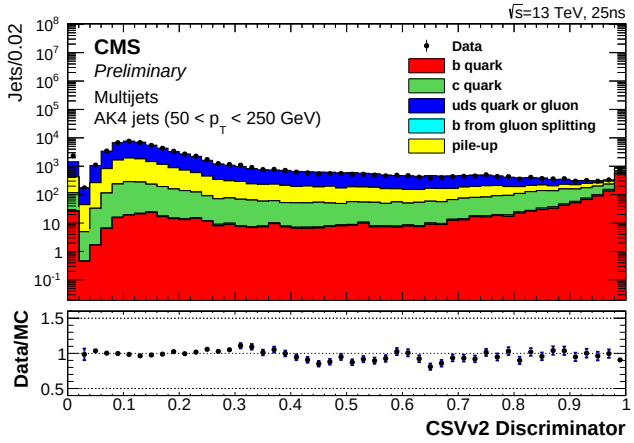

Figure 1.22: The CSVv2 discriminator (left) associated to jets with $50 < p_T^{jet} < 250$ GeV, data and MC comparison is shown. The stacked histograms indicate the contributions of different components from simulated multijet (QCD) samples. The operating point values for the loose, medium and tight tagging criteria are set to 0.605, 0.890, 0.970, respectively. [43].

1.2.9 The trigger and DAQ systems

The LHC provides proton-proton and heavy-ion collisions at high interaction rates. The bunch crossing time interval for the Run 2 is 25 ns. Furthermore, the number of simultaneous interactions per bunch crossing is not negligible and it depends on the instantaneous luminosity at which LHC operates.

The peak pile-up during the 2015 data taking period has been equal to 22-23 but up to 50 simultaneous interactions are expected in the next years. Given the high segmentation of the CMS detector, about 100 million readout channels are present and this corresponds to an enormous volume of data at the detector front-ends. Thus, the selection of signal events must start on-line.

The data size per bunch crossing is $\sim$1 MB resulting in a raw data rate of about 40 TB per second. Technical difficulties in handling, storing and processing such extremely large amounts of data impose a reduction factor on the rate of events that can be written to permanent storage. This task is performed by the trigger system, which is the baseline of the physics event selection process.

The key point of the trigger system is a fast time rejection of all the "non-interesting" events. This can be done by exploiting event topologies common to group of physics processes, such as the presence of one or more leptons in the event or a certain number of b-tagged jets. The trigger system needs to be as inclusive as possible, in order to collect data for all the physics searches that can be performed looking at proton-proton collision, but it has also to operate within the CMS time restriction and to not saturate the storage capability. The archival storage capability is of 1×10^3 Hz at data rates of $\mathcal{O}(10^2)$ MB/s and the required rejection power is $\mathcal{O}(10^5)$, too large to be achieved in a single processing step, if a high efficiency is to be maintained for rare physics phenomena. Thus, the trigger system is organized into two main levels [44]: the Level-1 trigger (L1), which reduced the

events rate down to 100 kHz, and the High Level Trigger (HLT), which reduced the L1 output to the final 1000 Hz to be stored. The L1 and the HLT are the active parts of the whole CMS data acquisition system (DAQ), that handles the data transfer from the sub-detectors pipelines up to the storage system.

1.2.9.1 Level-1 trigger

The Level-1 trigger (L1) consists of a custom-designed, largely programmable electronics, typically FPGAs (Field Programmable Gate Arrays) and ASICs (Application Specific Integrated Circuits). It is designed to take a fast accept/reject decision every bunch crossing, on the basis of a rough reconstruction of the event. Its design output rate limit is 100 kHz, which translates in practice to a maximal output rate of 30 kHz, assuming an approximate safety factor of three. The L1 is based on a synchronous pipelined architecture with an internal 40 MHz clock. Each process element must take less than 25 ns to complete its operation and the full detector information are stored in pipelined buffers for a constrained maximum time period of 3.2 μm.

The detector information used at L1 are coarsely segmented data from the calorimeters and the muon system only. These are the so-called *trigger primitives*, which indicate the presence and the number of objects like electrons, photons, muons, jets and E^T_{miss}. The data from the inner tracking system are not used at L1 since the bandwidth requirement of the tracker is too large to allow a read out at every bunch-crossing. The L1 multi level architecture analyses the trigger primitive while the high-resolution data are held in pipelined memories in the front-end electronics. A threshold on the transverse energy or p_{T} of these objects is applied and a selection of events on the basis of programmable trigger conditions are made. The event passing the L1 selection criteria are then analysed by the HLT system.

An upgrade of the L1 trigger system has been planned to improve its performance at high luminosity with large numbers of pile-up events. The electronics for the calorimeter have been replaced during the LS1 and the electronics for muon and global trigger systems is going to be replaced before the start of the 2016 data taking.

1.2.9.2 High level trigger

The high level trigger (HLT) is a software system implemented in a filter farm of about one thousand commercial processors (Event Filter). The full detector readout is available at HLT, but in order to meet the timing requirements given by the input rate from L1, events are discarded before being fully reconstructed, as soon there is enough reconstructed information to take the decision.

The HLT consists in a multi-step procedure that aims to reduce the $\sim$ 100 kHz event rate coming from the L1 to about 1000 Hz output to the data storage system. The first step requires the considered event has matched a particular L1 path or a logic combination of multiple L1 paths. In the second step, called L2, the information from the calorimeters and muon detectors are used to reconstruct the physical objects (CaloJets, electrons, photons, muons, MET). A further reduction of the event rate is obtained by applying requirements on the reconstructed objects properties. In the next step, denoted as L2.5, information from the pixel detector is exploited for track reconstruction and primary vertex identification. In the last step, known as L3, the information from the strip detector has also been processed and the same algorithms employed by the off-line reconstruction are used; due to time restrictions, the algorithms are modified in order to be faster even

with a slightly lower precision. At this stage, also particle-flow objects (in particular the *PFjets*) are reconstructed and used to get a further reduction of the event rate.

The HLT algorithms and filters are several and dedicated to various physical searches and different operating conditions (instantaneous luminosity, centre of mass energy, ect.). The group of algorithm and filters used to select a typical set of events is called an *HLT Path* and it is related to a precise L1 trigger path. About 400 HLT paths are currently implemented in CMS and two of these will be described in Section 5.3.

1.2.9.3 DAQ

The CMS data acquisition (DAQ) system assembles events at a rate of 100 kHz, transporting event data at an aggregate throughput of 100 GB/s to the high level trigger (HLT) farm. The L1 and HLT are completely integrated in the DAQ systems and they are its active components. Data coming from the detector are initially stored inside 40 MHz pipeline buffers by the front end system. Upon arrival of an acceptance signal from the Level-1, data is moved by the front end drivers (FEDs) to the front end readout links (FRLs) which are able to store informations coming from up to two FEDs.

The DAQ system has been redesigned during the accelerator shutdown in 2013/14 and 10/40 Gb/s Ethernet technologies are used for data concentration, as well as reduced TCP/IP implemented in FPGA for a reliable transport between custom electronics and commercial computing hardware. A Clos network based on 56 Gb/s FDR Infiniband has been chosen for the event builder with a throughput of $\sim$ 4 Tb/s. The fully built events are sent to the HLT with 1/10/40 Gb/s Ethernet via network file systems. Hierarchical collection of HLT accepted events and monitoring meta-data are stored into a global file system. The architecture of the new CMS DAQ2 system is schematically shown in Fig. 1.23 and further information can be found in [45].

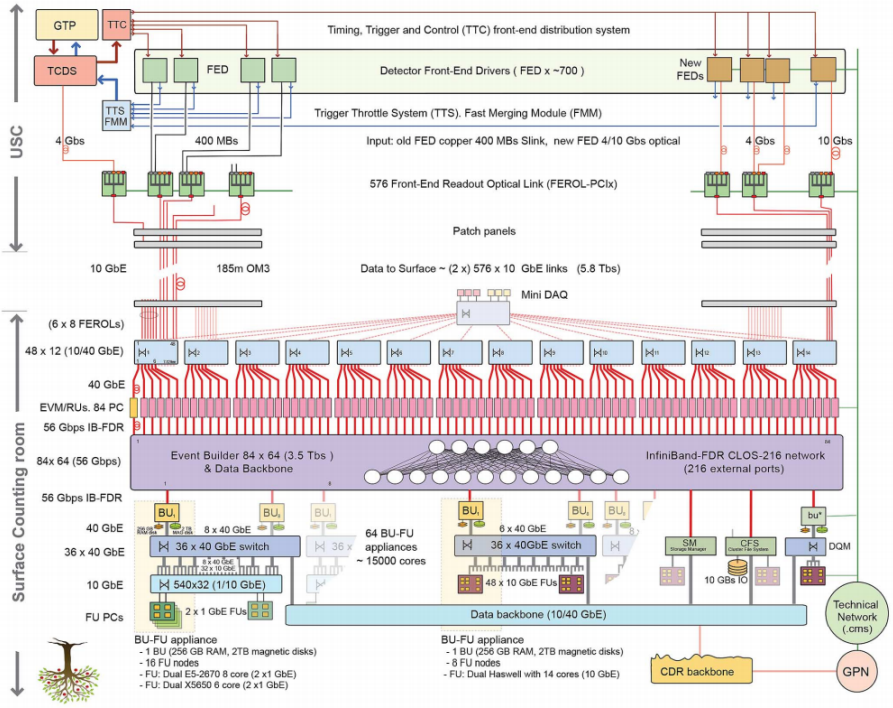

Figure 1.23: Over-all architecture of the new CMS DAQ system for LHC Run 2 [45].

Chapter 2

CMS Pixel Detector Phase 1 Upgrade

LHC started in 2008 and it is expected to be operative up to the 2035. During this period, the plan for machine and injector chain foresees a series of three long shut-downs, designated LS1, LS2, and LS3 (Fig. 2.1). The first, LS1, ended in 2014 and it allowed to increase the centre of mass energy of the collisions to 13 TeV. In the period through LS2 (2018), the injector chain will be improved and upgraded to deliver very bright bunches (high intensity and low emittance) into the LHC. Finally, in LS3 (2022), the LHC itself will be upgraded with new components to optimize the bunch overlap at the interaction region. Further upgrades will then be foreseen beyond the 2030.

The original performance goal for the LHC, to operate at an instantaneous luminosity of $1 \times 10^{34} \mathrm{cm}^{-2} s^{-1}$ with 25 ns bunch spacing, is likely to be achieved within next year (2016). Based on the excellent LHC performance to date, and the upgrade plans for the accelerators, it is anticipated that the peak luminosity will be close to $2 \times 10^{34} \mathrm{cm}^{-2} s^{-1}$ before LS2, and perhaps significantly higher after LS2. Thus, starting from 2017 the CMS experiment must operate with average number of interactions per bunch crossing (pile-up, PU) of 50 as a baseline, with the possibility that it may be significantly higher at the beginning of each LHC fills. Higher PU causes increment of fake rates in tracking and a reduced resolution in calorimetry with contamination due to overlapping signals. The total integrated luminosity prior to LS2 will reach of order 200 fb^{-1}, with 500 fb^{-1} achieved by LS3.

The detector performance, including good reconstruction efficiency at relatively low transverse energy, must be maintained even at a PU several times higher than the original design specification. This is the goal of the CMS upgrade program.

The first step of this program is called *CMS Phase 1 Upgrade* and it is related to the components mainly stressed by high PU: pixel detector, hadron calorimeters and L1-trigger. The Phase 1 Upgrade is currently on-going during the LHC technical stops and it will be finilized within the end of the 2017. A more complex upgrade step is planned for the LS3, the so-called *CMS Phase 2 Upgrade*. It will include deeper changes in the whole CMS, among which a complete substitution of the whole tracker detectors system. Looking at the nearest CMS Phase 1 Upgrade, three major changes are planned: a replacement of the pixel detector with a four-layer high-data-rate design, improvement to the L1-Trigger system with higher granularity and additional processing capabilities, and an upgrade to the photo-detectors and electronics for the hadron calorimeters (HCAL) to reduce background signals and improve measurement of jets and missing energy at high PU. The Phase 1 pixel detector upgrade is described in this chapter.

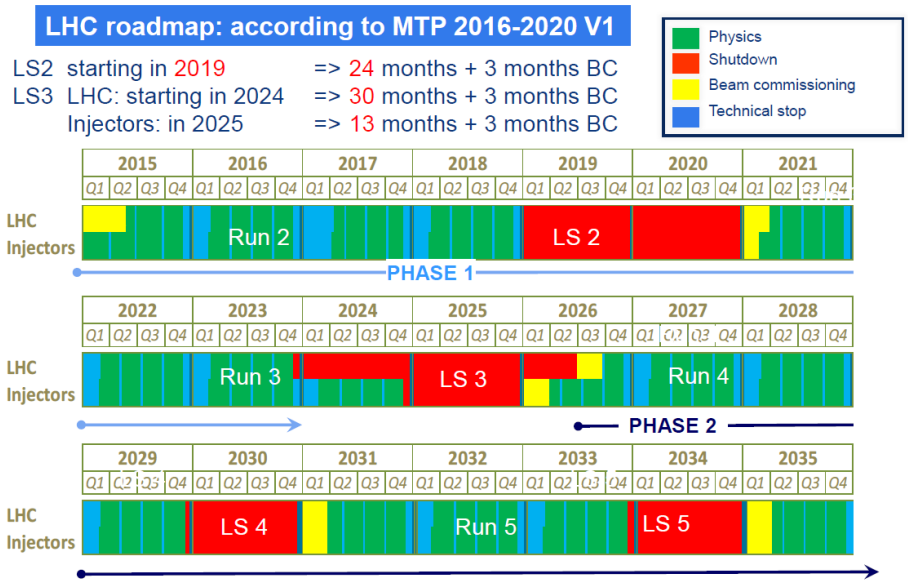

Figure 2.1: The outline LHC schedule out to 2035 as officially approved in June 2015 [46].

2.1 The Pixel Phase 1 Project

The pixel detector is a crucial component of the all-silicon CMS tracker as described in Section 1.2.3.1. The present detector was designed to operate up to the nominal instantaneous luminosity of $1 \times 10^{34} \mathrm{cm}^{-2} s^{-1}$ with 25 ns colliding bunch spacing, recording efficiently and with high precision the first three space-points next to the interaction region out to pseudorapidities ($|\eta|$) of 2.5. An average PU of about 25 is expected, under these conditions. Starting from 2017, the LHC performances are expected to increase and to reach the initial project ones. This will coincide with a worsening of the current pixel detector performances due to the dose absorbed from the detectors during 4 years of operation. The pixel detector is the closest to the interaction point and this leads to high level of radiation.The upgrade of the Pixel detector is therefore planned in order to maintain a high tracking performance at luminosities up to $2 \times 10^{34} \mathrm{cm}^{-2} s^{-1}$ and PU up to and exceeding 50.

The upgrade project is named *Pixel Phase 1 Upgrade* and it was defined in 2012 with the creation of the Technical Design Report [47]. It consists in the complete replacement of the current pixel detector including a re-design of the cooling system and re-position of all the services (front-end electronics, power supply, etc.).

The R&D for the development of the new modules started in the 2011 and the project is now in its core phase. After a pre-production period and a fine-tuning of the assembly steps, the modules production started this year in parallel with the producton of the mechanical structures, as it will be described in Section 2.2. The installation and commissioning of the detector is in fact planned for year-end LHC technical stop of 2016/2017. The new pixel detector is then expected to be operative up to the Phase 2 upgrade, around the 2022.

During this 5 years of operation, the LHC is expected to deliver about 500 fb^{-1}. Particle fluence has been estimated based on pixel cluster counting in the present detector and the expected absorbed ionizing dose for the different tracker detectors is reported in Fig. 2.2. The proposed upgrade system has been designed and tested to be operative up to this target, with the only exception of the innermost layer. The hadron fluence that will be

accumulated in the innermost pixel layer at $r = 3$ cm for 500 fb^{-1} is estimated to be $F = 3.0 \times 10^{15}$ n$_{eq}cm^{-2}$. This value is too high for the pixel sensor, thus a replacement of the innermost barrel layer is planned after 250 fb^{-1}.

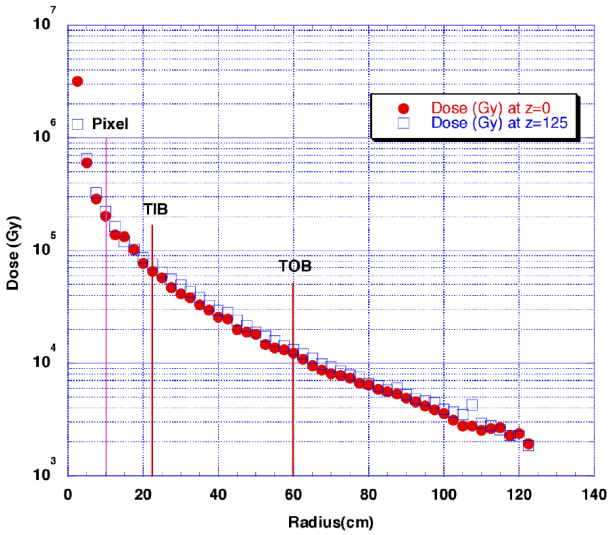

Figure 2.2: Estimate of the total Ionizing Dose absorbed by the CMS Tracker detectors after 500 fb^{-1} integrated luminosity.

2.1.1 Motivations for the pixel upgrade

As mentioned previously, the main motivations for the replacement of the current pixel detector are related to the worsening of the current pixel detector performances in conditions of high PU and instantaneous luminosity. The main limitations are reported below, together with the related solutions.

- Data loss at high occupancy and trigger rate. The current pixel detector was designed for a peak luminosity of 1 $\times 10^{34}$cm$^{-2}s^{-1}$ with a crossing time of 25 ns. Beyond this the pixel readout chip (ROC) suffers from significant dynamic data loss. This loss of data depends on both the occupancy and trigger rates and comes primarily from two sources, buffer size and readout speed. The pixel hits are stored in a finite sized buffer before being readout. When L1 trigger occurs, pixel hits are readout and the buffer is cleared. If this buffer is full the ROC cannot record any more hits and subsequent hits are lost. Furthermore, pixels that are being read out are blocked from having hits recorded; thus, data can be lost if the readout is slow with respect to the L1 trigger rate. Using a simulation of pp collisions and an emulation of the pixel readout, for the current pixel detector running at 1 $\times 10^{34}$cm$^{-2}s^{-1}$, a hit inefficiency of 4% is expected for the inner pixel barrel layer, raising to 15% for 2 $\times 10^{34}$cm$^{-2}s^{-1}$. A new Read-out Chip for the upgrade pixel detector will largely eliminate this dynamic data loss.
- Lower tracking efficiency or higher fake rates at high pileup. With more interactions per crossing giving rise to additional hits in the tracking detectors, the pattern recognition becomes more difficult and the current level of tracking efficiency is achievable only with a higher level of fake tracks. Thus, at

$2 \times 10^{34}\text{cm}^{-2}s^{-1}$ to keep both the CPU time and fake rate under control, the tracking needs to have lower efficiency than the current one. The requirement of hits in all 3 pixel layers leads to lower tracking efficiencies [48]. This negative effect of pileup can be partly mitigated with an extra pixel layer.

- Degradation in performance due to radiation damage. Hit detection efficiency and resolution for the pixel detector is expected to deteriorate with irradiation, due to the reduced charge collection. Although the degradation can initially be mitigated mostly with increase in bias voltage and modification of the pixel cluster hit templates, the reduced collected charge cannot be compensated after a certain value. A radiation fluence of 1.2×10^{15} $\text{n}_{eq}cm^{-2}$ is expected to be exceeded within LS3. After this exposure, according to simulations, the detector hit resolution deteriorates by roughly a factor of two in the transverse plane. Although the upgrade pixel sensor will suffer similar radiation damage, the new ROC will have a much lower charge threshold for pixel hits, which mitigates the effects of reduced collected charge. The degradation in hit resolution should be much reduced comparing to the same radiation fluence.
- Degradation in performance due to material. The pixel detector contains a sizeable amount of material, particularly in the higher $|\eta|$ part of the tracking region. Photons can be lost in this material due to conversion , electrons lose energy through bremsstrahlung, and charged particles suffer scattering effects close to the main pp interaction point which can affect vertexing. These effects may contribute to additional confusion for track pattern recognition in a high pileup environment. The upgrade pixel detector, even with an extra layer has less material in the tracking volume, due to a new lightweight construction, cooling, and relocation of passive material out of the tracking region.

2.1.2 The pixel detector layout

The Pixel Phase 1 detector can be divided, as the present one, into a Barrel region (BPIX) and a Forward region (FPIX). Those two regions of the detector are mechanically and electrically separated. The Barrel Pixel is divided into four layers while the Forward Pixel in six disks at both side of the barrel (endcap), as shown in Fig. 2.3. The main features and upgrade of BPIX and FPIX are reported in Tab. 2.1 and briefly described below:

- Barrel Pixel (BPIX): four concentric, cylindrical layers with a length of 548.8 mm and radii between 30 mm and 160 mm. The radius of the innermost layer is reduced by 10 mm from the current detector. The total number of pixels increases by a factor 1.6 from 48 M to 79 M.
- Forward Pixel (FPIX): six disks in each endcap, grouped in pairs of inner and outer rings, with a radial coverage ranging from 4.5 to 16.1 cm. The location along the beam line goes from 29.1 cm to 51.6 cm from the interaction point. It has a lighter structure than present FPIX and the blades on inner ring are tilted outward by 12° in to optimize hit coverage.

The placement of the two regions provides a four-hit coverage for all tracks over the pseudorapidity range up to $|\eta| = 2.5$.

The modules design and composition is almost equal in the whole pixel detector, except for the innermost layer where a considerable higher data rate is expected. The mechanical structure and services for both BPIX and FPIX are designed to reduce the material by using superlight mechanical support, CO_2 cooling, and by locating the readout elec-

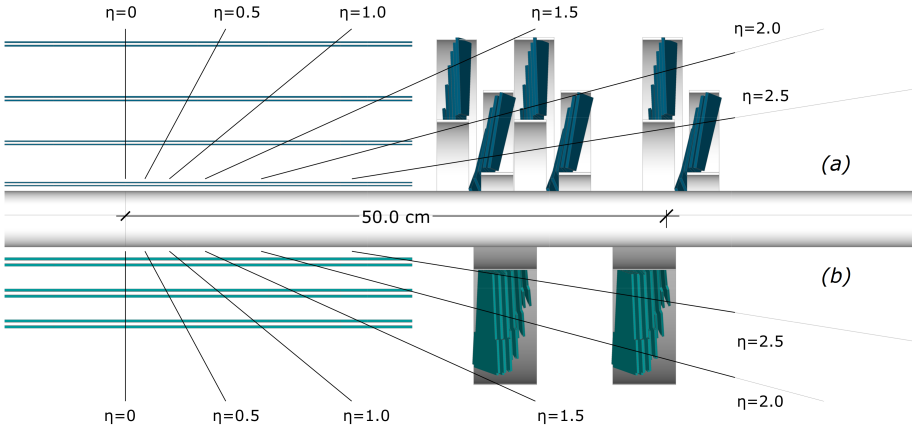

Figure 2.3: Layout of the upgrade (a) and current (b) pixel detectors; the different layers and disks of Barrel and Forward regions are shown.

		Current	Upgrade
Barrel Pixel (BPIX)	n° layers	3	4
	length on z-axis	570 mm	548.8 mm
	radial positions	44, 73, 102 mm	29.5, 68, 109, 160 mm
	n° modules	768	1184
	n° pixels	48 M	79 M
Forward Pixel (FPIX)	n° disks	2	6
	radial coverage	6-15 cm	4.5-16.1 cm
	z-axis position	$\pm$34.5, $\pm$46.5	$\pm$29.1, $\pm$39.6, $\pm$51.6 cm
	n° modules	672	672
	n° pixels	18 M	45 M

Table 2.1: Main features of the upgraded BPIX and FPIX systems; comparison with the current detector is also reported.

tronics away from the active region. The pixel detector modules will be described more in details below. Any additional information on the Phase 1 Pixel Detector can be found here [47].

2.1.3 The pixel modules

The upgraded pixel detector will have 1184 pixel modules in the barrel BPIX, compared to 768 modules in the present detector, with an increase in the pixel count from 48 million to 79 million. In the forward FPIX the number of modules will remain the same (672) but FPIX modules will be equal to the BPIX ones and thus larger than in the present detector, increasing the pixel count from 18 million to approximately 45 million. The module is the unitary element of the pixel detector and it is composed by four main parts, see Fig. 2.4:

- Sensor: silicon pixel sensor, $n^+ - in - n$ technology, 285 μm thickness, 66,560 pixels in each sensor, equal to the current one;
- Read-Out Chip (ROC): 180 μm thickness, 250 nm CMOS technology, ROC size of $7.9 \times 10.2 mm^2$, pixel array: $52 \times 80 = 4160$, completely re-disigned;
- High-density interconnects (HDI): connector print for power and control signals distributions, transfer data from ROC to DAQ, re-disigned;
- Token bit manager (TBM): module controller ASIC, it manages the data coming from ROCs and the clock distribution, re-disigned;
- Base strips: for mounting, 250 μm thick silicon nitride (SisN4), unique not-electrical component.

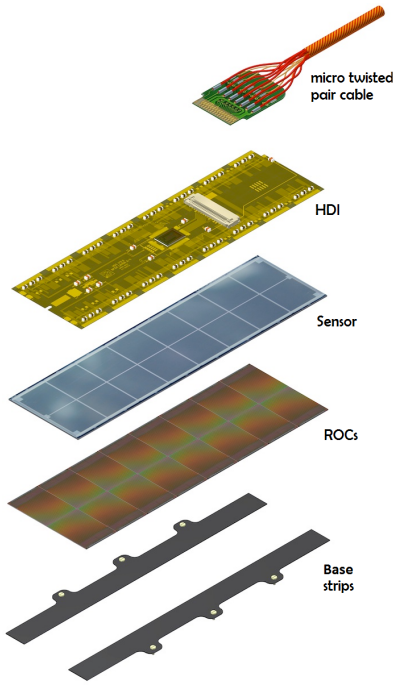

Figure 2.4: Module structure for the BPIX Layer 2-4 of the Pixel Phase 1 detector.

The sensor is bump-bonded to 2×8 ROCs forming a detector unit with 66,560 pixels. The HDI is glued on top of the sensor and wire-bonded to the pads in the ROCs periphery. The TBM chips is glued and wirebonded on the HDI. The module is connected to the front-end electronics via micro-twisted cables (Al,Cu) designed to minimize their

material budget.

Differently from the current detector, the modules design and composition is almost equal in the whole pixel detector. The size of the sensor is identical between FPIX and BPIX and inside each region. This simplifies sensor production, module assembly, and testing and it increases the number of pixels in the forward region. The FPIX has few differences in the sensor design and in the HDI, while the readout chip is the same of the Layer 2-4 of BPIX.

The innermost barrel layer presents the main differences from the rest of the detector because it needs to operate in more extreme conditions. The expected particle flux in the Layer 1 is four time the one for BPIX Layer 2. The readout line for the Layer 1 is thus enhanced and the readout chip is an evolution of the one used in the rest of the detector. The ROCs will be thinned to 75 μm and 180 μm thickness for the BPIX Layer 1 and the BPIX Layers 2-4, respectively, to reduce the material budget.

2.1.4 The sensor

The sensor is the core part of the pixel detector but it is also the one that necessitates less improvements in the Phase 1 upgrade. The sensor of the current detector has in fact been tested at different irradiation level, with various irradiation campaigns [49, 50], and good performances has been observed up to a proton fluence of $F = 1.1 \times 10^{15} n_{eq}/cm^2$, as shown in Fig. 2.5. This value is not sufficient for the innermost BPIX layer but it is enough for all the other layers and FPIX disks. Thus, the design of the sensors for the upgrade CMS pixel detector has been maintained equal to the current one.

The detector is a silicon sensor based on $n^+ - in - n$ technology, where the pixels are formed by high dose n-implants introduced into a highly resistive n-substrate [51]. The junction is formed with a p-implant on the back-side, as shown in Fig. 1.10. The active area of the module is $16.2 \times 64.8\, mm^2$ with the same pixel size as before, $100 \times 150\, \mu m^2$, for a total of 66,560 pixels. The sensors are fabricated on 4 inch wafers, 3 sensors each, with a thickness of 250 μm.

As described in Sec. 1.2.3.1, the pixel sensor design has been driven by the will to exploit charge sharing among pixels in order to improve the position resolution. The n-type substrate implies the collection of electrons, advantageous respect to the holes because of their higher mobility. This, in fact, causes a larger Lorentz drift of the signal charges which leads to charge sharing between neighbouring pixels. Furthermore, the higher mobility of electrons makes them less prone to trapping, which leads to a higher signal charge after high absorbed dose. Furthermore, after irradiation induced space charge sign inversion [24], the highest electric field in the sensor is located close to the n^+ electrodes used to collect the charge. This allows significantly underdepleted operation, it avoids extremely high bias voltages and thus it reduces the leakage currents and high voltage breakdown issues.

The main complication of the choice of n-substrate is the requirement of a double sided sensor process. The pn-junction on the back-side of the sensors can not extend into the diced edges of the sensor. Thus, the back-side must be structured and double-sided processing of the wafers is mandatory. Both sides of the sensor need photo-lithographic processing and this leads to higher costs compared to single sided p-in-n (or n-in-p) sensors. However, it leads also to the implementation of guard-ring structures on the backside, which keep the sensor edges near ground potential. This removes the risk of high voltage sparks across the 15 μm air gap between the sensor edge and the readout chip. The sensor is measured to have a high voltage stability well beyond 600 V.

The n-implants need to be electrically isolate from each other because the electron accumulation layer induced by ionizing radiation tends to short-circuit the pixel implants. To implement this inter-pixel isolation, two different techniques were developed. A moderated p-spray technique with a punch through biasing grid [52] has been used for the BPIX while a partially open p-stop technology for FPIX [53], Fig. 2.6. This difference in the design technologies is due to the fact that sensors for the forward and barrel detectors were developed independently, in cooperation with two different vendors. The p-stop rings have openings in order to have a controlled high resistive path between pixels and to maintain them at a well-defined potential. In the p-spray technology, a punch-through resistor connects pixel to a bias grid for the same purpose.

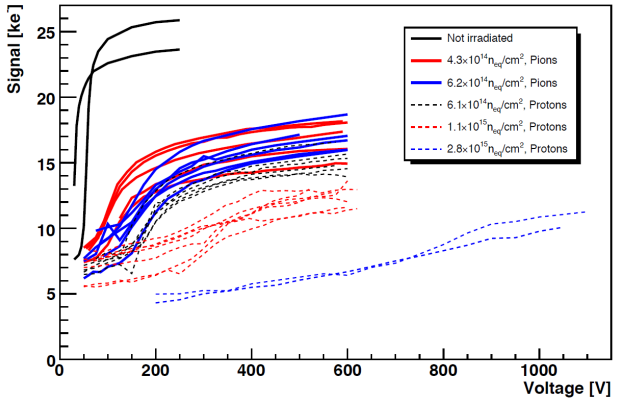

Figure 2.5: Charge collection in non-irradiated and irradiated sensors with different doses and different particle types (sensors of 285 ± 15 μm thickness) [49].

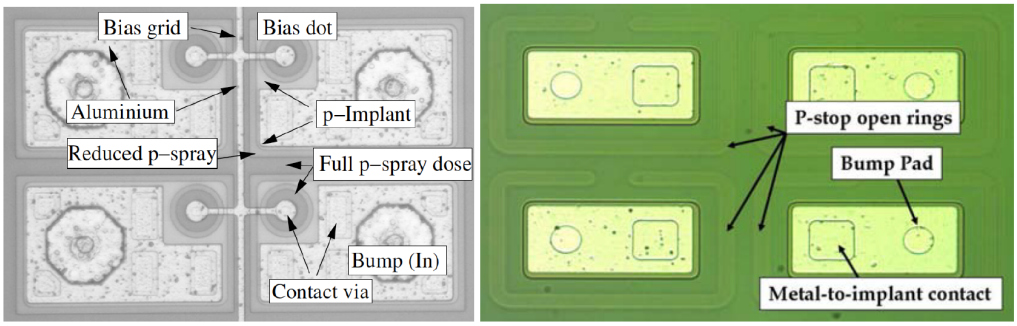

Figure 2.6: Photograph of four pixel cells in the same double column for BPIX (left) and FPIX (right) sensors; p-spray implant and p-stop open rings are visible [22].

2.1.5 The new Read Out Chip

The Read-Out Chip (ROC) for the new pixel detector has been re-designed by the CMS PSI group, based on the experience of the current well-proven ROC (*psi46v2*) that is operative in CMS since its commissioning [21]. The structure of the chip remains mostly untouched while the main changes occur in the read-out pipeline, such as a signal digitalization and an increment of the buffers. The new ROC (*psi46dig*) will be used for all the FPIX disks and for the BPIX Layers 2, 3 and 4. A more advanced ROC is currently under development for the Layer 1 in order to face the higher hit rate expected. Several version of the psi46dig occurred since the first prototype of the new ROC, each one with

some change suggested by test-beam results. Actually, the final version of the new ROC is called *psi46digV2.1respin* and it has been officially submitted on March 2015.

2.1.5.1 The ROC architecture

The *psi46digV2.1respin* is based on the 250 nm CMOS technology, as for the present ROC. The new ROC consists of three main parts, see Fig. 2.7: a pixel matrix composed of 4160 pixels distributed in an array of 80 rows and 52 columns; 26 double column interfaces each of which contains time stamp and data buffers; a control interface block that hosts readout logic, analog-to-digital converters (ADC), I2C interface, voltage regulators, etc.

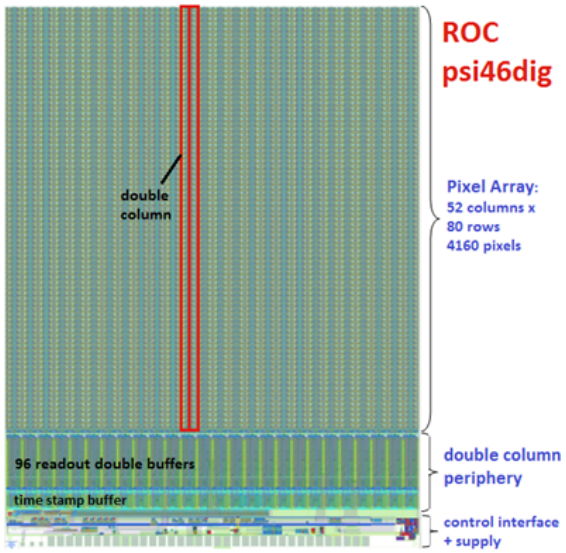

Figure 2.7: Scheme of the new CMS Pixel Read-Out Chip, psi46dig; courtesy of B. Meier et al., PSI.

2.1.5.1.1 The Pixel Unit The pixel rows and columns have a pitch of 100 μm and 150 μm respectively. Each pixel is composed by a pixel unit, schematically shown in Fig. 2.8. The pixel unit includes pre-amplifier, shaper and a sample and hold (S&H) circuit to store the signal before it is sent to the ROC periphery.

A comparator circuit is placed between the shaper and the S&H to get a signal discriminator inside each pixel unit. The comparator threshold is set once per ROC and then it can be fine-tuned inside each pixel unit. This process is called *Trimming* and, acting on 4 *trimbits* it allows to get an uniform threshold in the whole ROC. A *mask bit* is also present to completely de-activate the pixel in case it results to be noisy. In addition, an internal signal injection circuit is included to test the ROC without any external source. Each part of the pixel unit have individual registers that allow a fine regulation. The total amount of settable DACs in the ROC is 16 plus 2 internal registers. The number of DACs has been consistently reduced respect the current ROC to simplify the ROC tuning and to avoid issues coming from the alteration of the register after high absorbed doses.

2.1.5.1.2 The double column system and ROC Periphery The pixels are grouped in 26 double columns (DCOL) with 160 pixels each. Every double column is read out

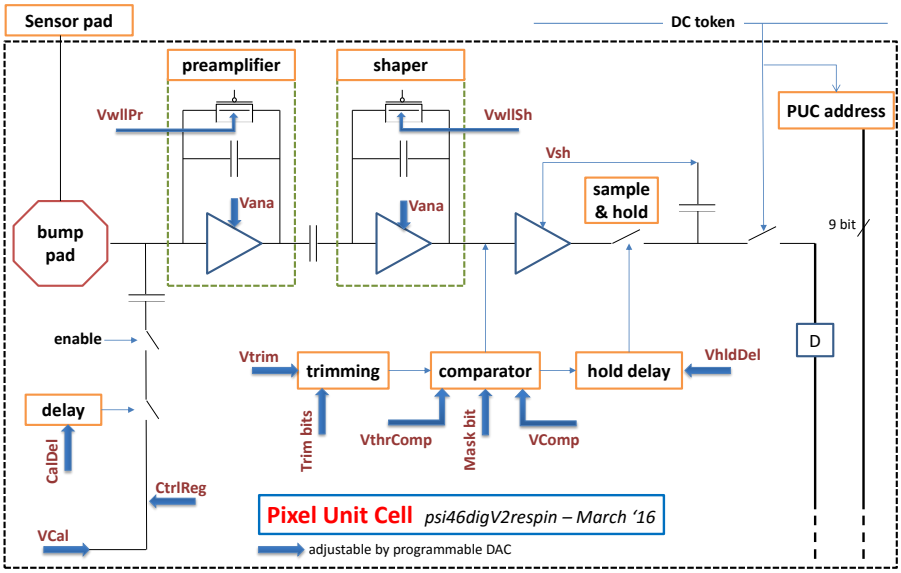

Figure 2.8: Schematic view of the pixel unit cell of new CMS pixel readout chip.

separately and has its own buffers. The first readout logic is included inside the pixel unit with the threshold cut. The pixel read out is so structured:

1. All pixels in a DCOL with a hit (signal over threshold) send immediately a signal to the DCOL periphery by a wired or line called *colOr*. This happens asynchronous, there is no clock in the pixel unit.

2. The DCOL periphery synchronize the signal with the clock and generates a timestamp that is written to the timestamp buffer.

3. The DCOL periphery sends a token to the pixels to read out all addresses and the analog pulse height of the hitted pixels. All this information is stored in the data buffer.

Once the trigger comes in the ROC periphery, an internal token starts to pass through the whole double column buffers and the stored signals are moved to the first readout level of the ROC periphery, as shown in Fig. 2.9. Here the Pulse Height (PH) is converted into a digital sequence by a 8-bit successive approximation current ADC which runs at 80 MHz. In the ROC periphery a PLL is also present, which generates the 160 and 80 MHz clock for the serial readout links and the ADC respectively, taking the 40 MHz LHC master clock as input. The PLL has an extremely wide locking range between 10 and 75 MHz. This ensures a frequency range wide enough for operation after the radiation induced damage expected over the full detector lifetime. The PH is then sent to the readout buffer, a FIFO in which the 15-bit pixel address is linked to the 8-bit PH. This readout buffer is linked to a 4 bit MUX, where the ROC information are added to the signal sequence, and finally to the serializer where the final 160 $Mbit/s$ data flow is managed. The communication between the readout buffer and the serializer is handled by an additional logic level which is directly interfaced with the two signals coming from the module (module Token and Trigger). The internal token that pass by the whole double columns is decoupled from the module token which handles the serial readout of the 16 ROCs in the module. This allows a strong reduction of the data loss as it will be described below, together with the main improvements and changes from the current chip.

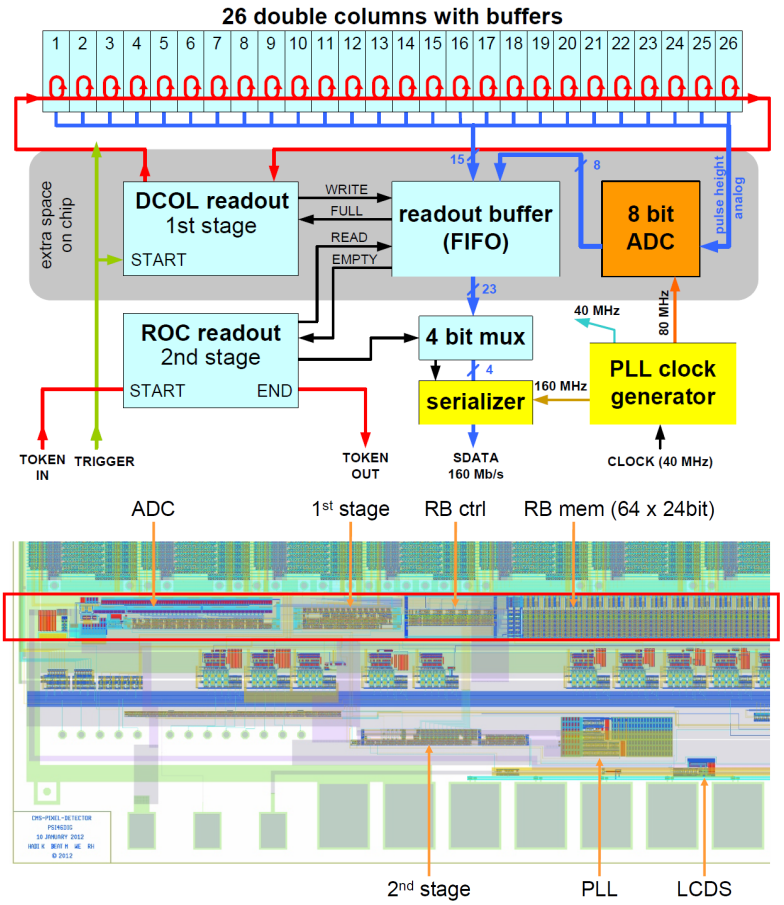

Figure 2.9: Schematic view (up) and design (down) of the psi46digV2.1respin periphery with details of the new readout system including an additional buffer stage.

	psi46v2	psi46digV2.1respin
ROC size	7.9 mm $\times$ 9.8 mm	7.9 mm $\times$ 10.2 mm
Pixel size	100 μm $\times$ 150 μm	100 μm $\times$ 150 μm
Smallest radius	4.3 cm	2.9 cm
Settable DACs / registers	26 / 2	16 / 2
Pixel charge readout	analog	digitized, 8bit
Readout speed	40 MHz	160 Mbit/s
Time stamp buffer size	12	24
Data buffer size	32	80
Output buffer FIFO	no	yes
Double column speed	20 MHz	20 MHz
Metal layers	5	6
Leakage current compensation	yes	no
In-time threshold	3500 e^-	< 2000 e^-
PLL	no	yes
Data loss at max operating flux	$\sim$3.8% at 120 MHz/cm^2	1.6% at 150 MHz/cm^2

Table 2.2: Comparison of the current (psi46v2) and the upgraded (psi46digV2.1respin) CMS Readout chips [47].

2.1.5.2 The new ROC improvements

The ROC architecture described before is driven by the necessity of reduce the current data loss mechanisms in high PU conditions and by the increment of the total amount of data rate coming out from the pixel detector, due to the higher number of modules and to the increased instantaneous luminosity. In addition, the ROC threshold has to be reduced to face the sensor performance decrease after high irradiation. It is in fact estimated that, after 250 fb^{-1}, the amount of the collected charge per minimum ionizing particle passes from 24 ke^- to 10 ke^-, due to non-fully depleted mode operation [47]. A comparison of the main features of the current and upgrade ROC is reported in Tab. 2.2.

The main improvements of the new readout chip are:

- Digital readout: to face the higher data rate, the bandwidth of the analog 40 MHz level-encoded data links have been replaced by a digital readout at 160 Mb/s. As shown in Fig. 2.10, the new data format is composed by a fixed ROC header (12-bit), column and row corresponding to the pixel address and the encoded pulse height. The pixel information correspond to 24-bit. The sequence is composed in the ROC periphery, as shown previously.
- Reduction of data loss: the main data loss mechanism in the current ROC is the overflow of both data and time stamp buffers [54]. Upon receiving a hit, a pixel sends to the double column periphery the bunch crossing number, its own address and the pulse height to be stored in these buffers. The Level 1 trigger latency in CMS is about 3.6 μs. During this time all hits should be stored in the double column periphery and, obviously, the frequency of the buffers overflow increases together with the instantaneous luminosity. Thus, the number of data buffer cells has been increased from 32 to 80 and the number of time stamp buffers from 12 to 24 cells, as shown in Fig. 2.11. The periphery footprint and overall size of the chip is increased of 0.5 mm only, thanks to the redesign of the buffer layout. To further reduce dead time during the readout phase, an additional global readout buffer has been introduced between the double column buffers and the output data links. This allows to separate the double column buffer from the readout chain of the whole module. In the cur-

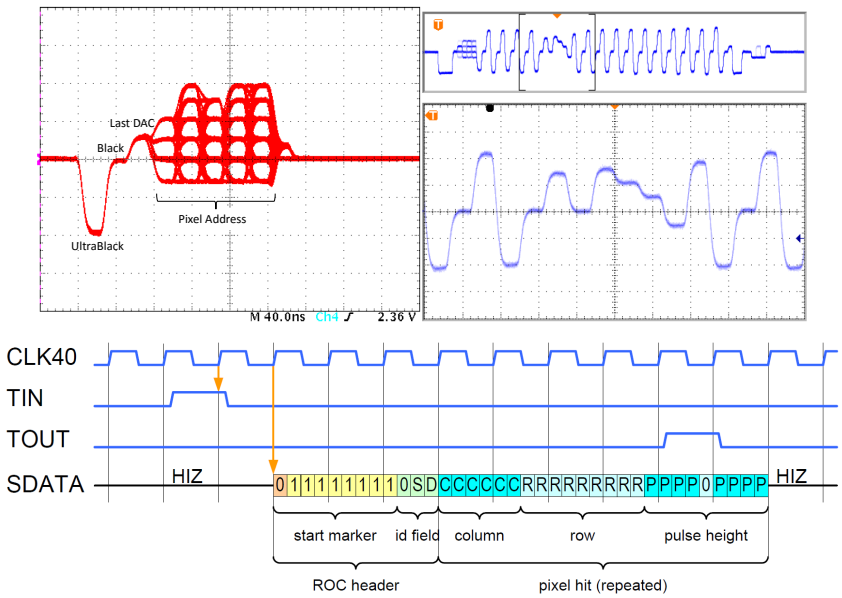

Figure 2.10: Data format of the current analog (up) and upgraded digital (down) ROC. A single pixel readout (36-bit) is shown for the digital ROC. For the analog readout, one pixel hit is shown on the left side and all possible pixel positions are scanned and the oscilloscope traces superimposed; the readout of a barrel module with a TBM and 16 chips is shown on the right [22].

rent ROC, the readout uses a serial protocol, where all double columns and all ROCs in a module are daisy-chained and controlled by the TBM. The higher the link occupancy the longer is the readout time and hence the dead time in the columns. With the new additional readout buffer instead, all ROCs on a module can readout the DCOL buffers by itself immediately after verifying the data by a trigger, reducing the DCOL dead time.

- Lower Threshold: the lower is the pixel threshold, the longer is the lifetime of the detector. This ROC feature lays on the analog amplifier and on the discriminator inside the pixel unit. Those have been completely re-designed, the power rails have been decoupled from the comparator ones and the routing of many rails have been optimized in order to lower as much as possible the cross-talk (induced noise). The new discriminator is extremely fast, its time-walk is almost negligible compared with the current ROC and no threshold increment is needed to face the time-walk effects, as shown in Fig. 2.12. In addition, a thicker metal layer has been used in the outermost level of the ROC. Thanks to these changes, the new ROC is expected to have a threshold of $<$ 2000 e^- versus the 3200 e^- threshold of the present ROC.
- Operational issues: several minor changes have been implemented to facilitate the operation of the detector. A power-up reset circuit has been introduced to ensure a low power state of the ROC after powering on. Programmable parameters on the ROC have been removed or made independent of each other to simplify procedures of finding ideal settings after radiation damage.

Considering those changes, while the current ROC would suffer from 16% data loss at the innermost layer at instantaneous luminosities of 2 $\times 10^{34}$cm$^{-2}s^{-1}$ for 25 ns bunch spacing, simulations show that the upgraded detector is expected to have a layer 1 data

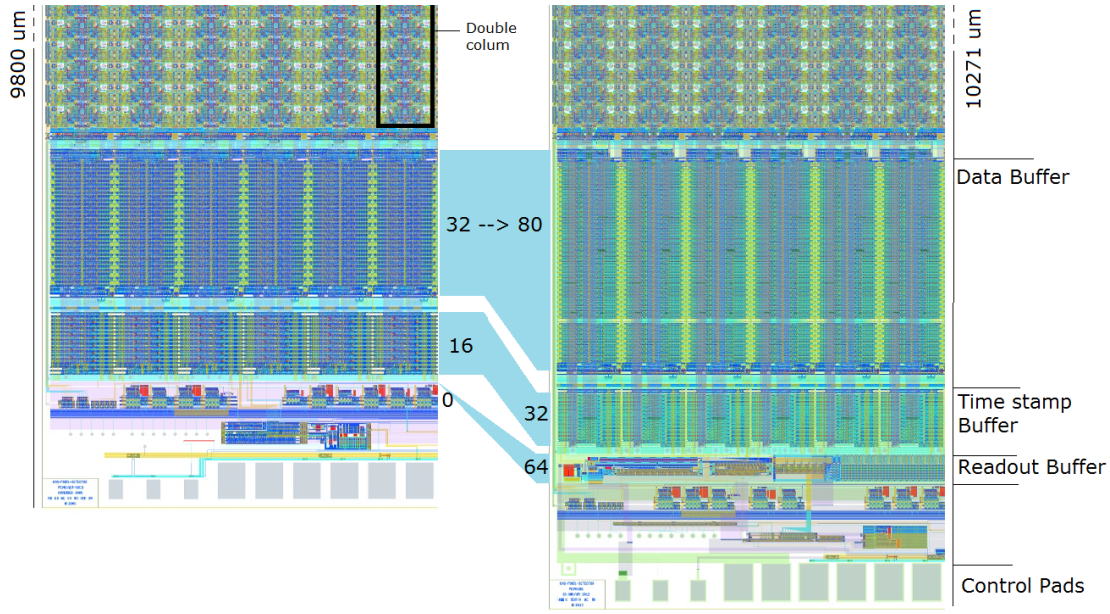

Figure 2.11: Design of the current (left) and upgraded (right) ROC periphery; 6 double columns on the bottom left corner of the ROC are shown; the data buffer and time stamps buffer cells increment is evident, together with the additional readout buffer cells.

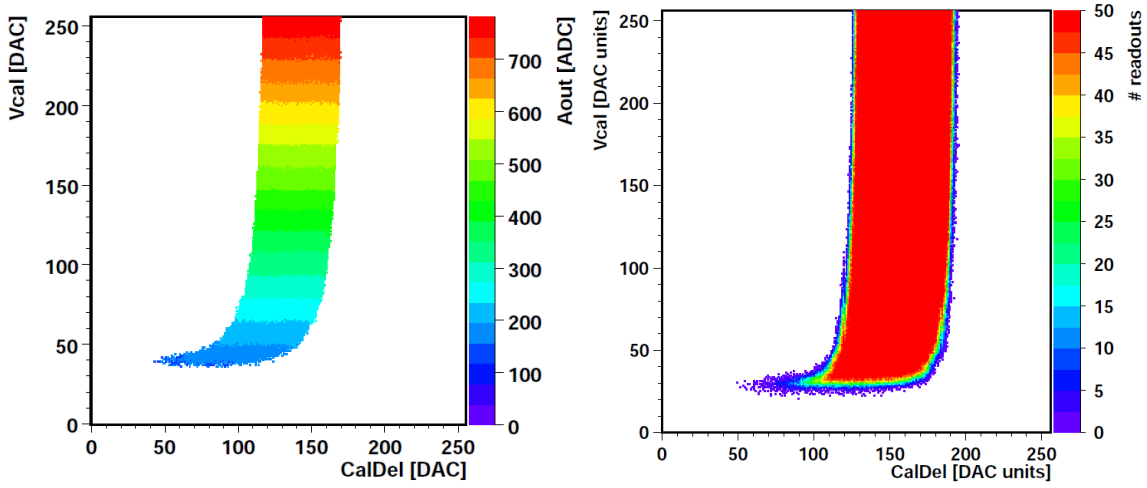

Figure 2.12: ROC read-out as a function of intensity of the injected signal (VCal) and injection delay (CalDel) for the current (left) (courtesy of CMS DESY laboratory group) and upgraded ROC (right). A fully efficient read-out is obtained for a larger time and threshold ranges in the upgraded ROC.

loss below 2.4% [54].

As for the radiation tolerance, the new readout chip have been exposed to different doses with 24 MeV protons. As described before, during the running period up to LS3 the LHC is expected to deliver about 500 fb^{-1}. For pixel modules in Layer 1 at z = 0 cm the estimated dose after 500 fb^{-1} is about 1.2 MGy while it is around 0.6 MGy for the other layers. Several irradiation campaigns has been made during the pre-production phase and some minor changes in the ROC design occurred in order to increase the ROC functionality after irradiation. Finally, ROCs irradiated up to 1.2 MGy have been tested and no operational failure has been observed [55]. The efficiency of the ROC will be maintained above 98% after the irradiation and the design values for the analog and digital currents ($\sim$ 24 mA) can be comfortably reached before and after irradiation.

2.1.6 The HDI and TBM

The 16 ROCs in the modules are electrically connected to the High Density Interconnects (HDI), glued on top of the sensor. The HDI is simply a connector print that transfers signals (and power) from ROCs to the DAQ system and vice versa.

The core of the signals management is a chip placed in the middle of the HDI: the Token Bit Manager (TBM). It is a custom, mixed-mode, radiation-hard IC that manages the data coming from ROCs and the clock distribution. The main task that have to be faced is the synchronization of the serialized readout of the 16 ROCs with the general LHC clock and its translation into a 400 $Mbit/s$ output. The internal structure of the TBM is shown in Fig. 2.13. It is composed by four major blocks: two equal TBM cores (one per module side), a Communications Control Hub, and a DataKeeper multiplexer and encoder. The latter allows to get a 4/5b encoding and to pass from a 2×160 Mbit/s to the final 400 Mbit/s.

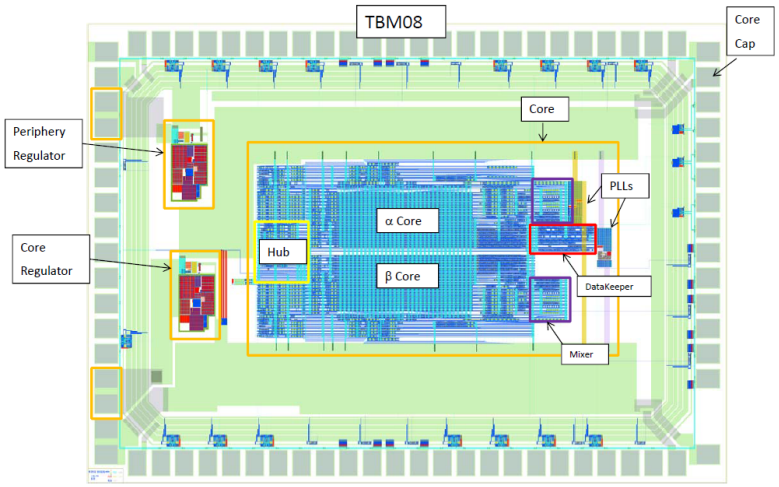

Figure 2.13: Schematic view of the Token Bit Manager (TBM).

The principle functions of the TBM include the following:

- Distribute the Level 1 trigger, and clock to the ROCs.
- Control the readout of the ROCs by initiating a token pass for each incoming Level 1 trigger.
- Write a header and a trailer word to the data stream on each token pass; the header contains an 8-bit event number while the trailer contains 10-bits of error

status, plus how many events are awaiting readout.

- Management of the stack for the Level 1 trigger; each trigger is inserted in the stack until the associated token comes back from the ROC readout.

A TBM receives three control signals: a 40 MHz clock, synchronized to the CMS beam crossing, a serial data line for configuration settings and a serial encoded trigger signal. The serial data is then transferred to each ROC for the programming via the I2C channels.

The TBM has been completely re-designed from the current version and several improvements have been implemented. The new structure is more complex and several iterations have been necessary to obtain a radiation hard chip. The main problems occurred in the synchronization of the 160 MHz and 400 MHz PLL. The final solution includes several internal registers for each single phase adjustment. In the end, the *tmb08c* has been produced and it will be installed in the layers 3 and 4. In the Layer 2, to face the higher expected data rate, the module is designed to have a double 400 $Mbit/s$ readout output. A different version of the chip, *tmb09c*, with two Datakeepers will thus be used to get two output lines. The Layer 1 is instead planned to have 2 identical TBMs per module, each one managing 8 ROCs only, and they are currently under finalization.

2.1.7 Pixel upgrade expected performances

The Phase 1 Pixel detector has been designed to improve crucial performances of the tracking system, such as tracking efficiency versus fake rate and b-tagging efficiency but, moreover, to be less sensitive to the effects induced by a higher pile-up and luminosity regime. All this combined with a reduction of the material budget. The main studies on the expected improvements have been done referring to the detector performances measured on 2011 and are reported in [47]. A simulated $t\bar{t}$ sample has been used for these simulations.

2.1.7.0.1 Material budget Since the extra pixel layer could easily increase the material of the pixel detector, all the designed has been oriented to reduce as much as possible the material budget by using ultra-lightweight support, CO_2 cooling and to relocate the services out of the tracking volume. A comparison of the material budget for the current and Phase 1 pixel detectors is shown in Fig. 2.14 as a function of η. The overall mass of the FPIX detector is estimated to be reduced by $\sim 40\%$, with a $\sim 50\%$ reduction in radiation length in the half-disks. This will bring to a 50% fewer photon conversions at $\eta = 1.5$.

2.1.7.0.2 Tracking performances The upgraded pixel detector will have excellent four-hit coverage over its whole η range. This allows for the creation of four-hit track seeds with an intrinsically lower fake rate than that of three-hit seeds and a consequent improvement of the tracking performances. The efficiency to reconstruct a charged particle track (track efficiency) and the probability that a reconstructed track is a fake track (track fake rate) are reported in Fig. 2.15. The simulated scenario considers a 25 ns collision frequency with a 50 pile-up condition and shows an improvement greater than 10% with respect to the current detector. Moreover, the tracking efficiency for the upgraded detector does not show any dependence to the PU until value of 100.

Other tracking parameters that indicate the improvement of the Phase 1 detector are the impact parameter resolution and the primary vertex resolution, as defined in 2.15. The effect of the higher pileup and the dynamic data loss is to increase the impact parameter

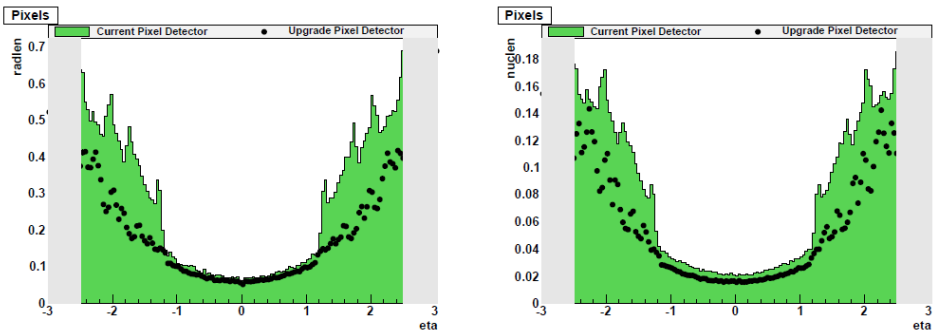

Figure 2.14: The amount of material in the pixel detector shown in units of radiation length (left), and in units of nuclear interaction length (right) as a function of η for the current pixel detector (green histogram), and the Phase 1 upgrade detector (black points). The shaded region at high $|\eta|$ is outside the region for track reconstruction [47].

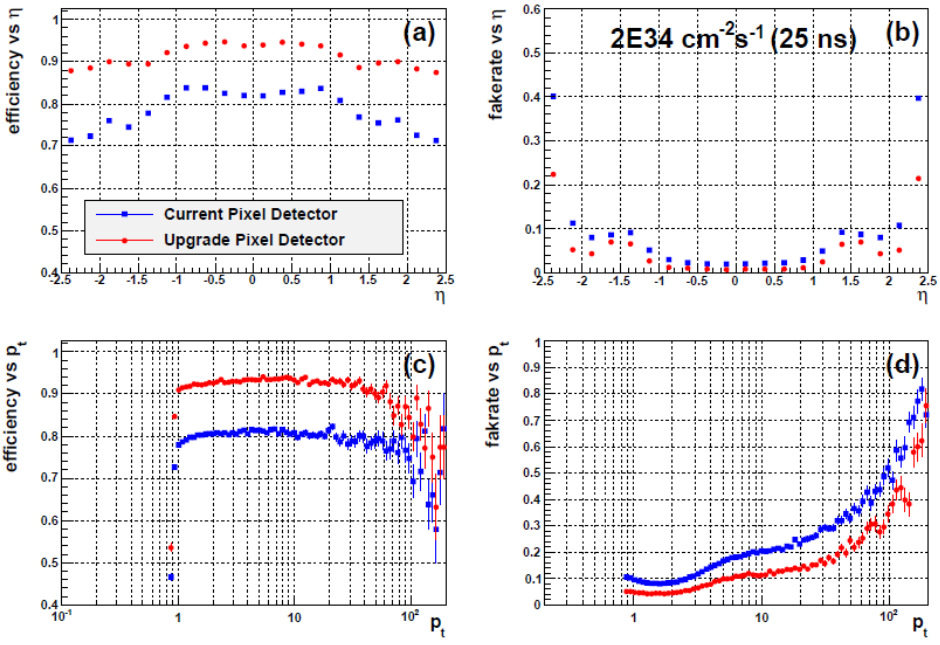

Figure 2.15: Tracking efficiency (a,c) and fake rate (b,d) for the $t\bar{t}$ sample as a function of track η (a,b) and track p_T (c,d). Results are shown for an average pileup of 50 with ROC data loss simulation expected for the current pixel detector (blue squares) and for the upgrade pixel detector (red dots).

resolutions. The expected improvement for the upgraded detector is a factor 1.5 in the zero pileup scenario, mainly at the lower momentum ranges. This factor increases in high PU scenario and it is most evident in the higher momentum regions in all $|\eta|$ ranges. The primary vertex resolution degrades at high pileup mainly because of the dynamic data loss. The expected worsening in the primary vertex resolutions is 20%-40% for the current detector while the expected improvement with the upgraded one is shown in Fig. 2.16.

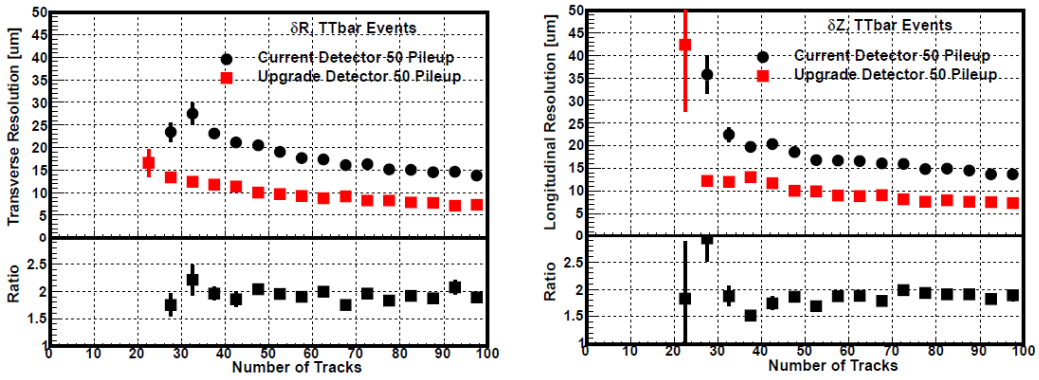

Figure 2.16: Transverse (left) and longitudinal (right) primary vertex resolutions as a function of the the number of tracks in the vertex for a $t\bar{t}$ sample with an average 50 PU. The resolutions are shown for the current pixel detector (black circles) and the Phase 1 upgrade detector (red squares). The lower part of each plot shows the ratio of the current detector resolution to the upgrade resolution.

2.1.7.0.3 b-tagging efficiency The b-tagging performance for the Phase 1 upgrade pixel detector is expected to have a strong improvement at high pileup thanks to the tracking performances shown before. The b-tagging algorithm used for this comparison is the *Combined Secondary Vertex* (CSV) algorithm, extensively studied and used during the Run 1. In the current Run 2, an upgraded version of that algorithm is used: the CSVv2, described in Sec. 1.2.8.1. It provides about a 10% improvement in the b-tagging efficiency with respect to the previous CSV. A comparison between current detector and Phase 1 detector performances, based on the new CSVv2 is not yet available. However, the results based on the Run 1 algorithm is a good baseline and the improvement factor will probably increase with the development of an upgraded algorithm. In this study, no tuning was done for high pileup or for the upgrade detector on the selection criteria for the track collections used in the algorithms. The baseline selection applied is with $p_{\mathrm{T}} > 30$ GeV and $|\eta| < 2.4$. In Fig. 2.17 the comparison between current and upgraded detector performances is shown in a zero and 50 PU scenarios. The improvement in high PU condition is evident and it is estimate to be 10% with a 10^{-2} fake rate.

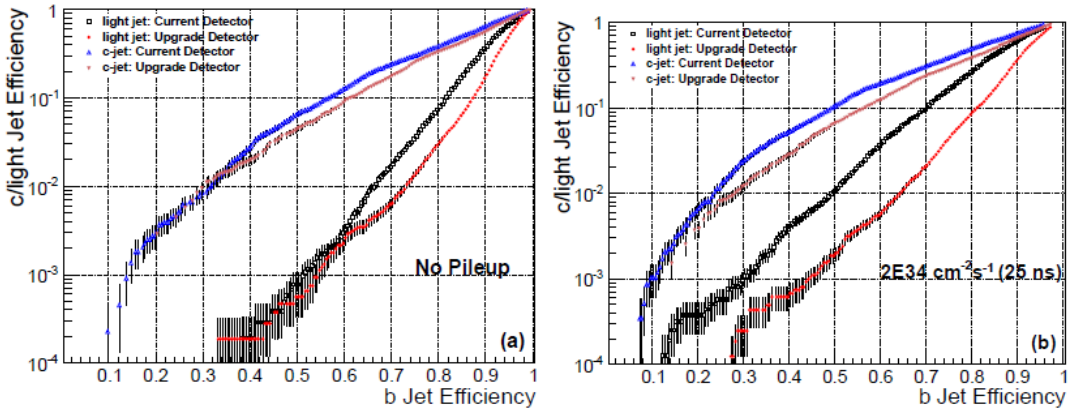

Figure 2.17: Performance of the Combined Secondary Vertex b-tagging algorithm for jets with $p_T > 30$ GeV in a $t\bar{t}$ sample with (a) zero pileup, and (b) an average pileup of 50. The performance for the current detector is shown by the open points while the solid points are for the upgrade detector. The triangular points are for c-jets while the circle and square points are for light quark jets.

2.2 Production of the new CMS pixel detector

The production of the new CMS Pixel Detector includes five main aspects: Barrel modules production; Forward modules production; mechanics design and assembly; cooling system; data acquisition system. The latter is developed by CERN together with Strasbourg and Vienna groups while the cooling system design is based on the experience achieved with the current detector as well as the mechanics design, done by the PSI group involved in CMS. The forward modules are entirely produced by U.S. consortium while the barrel modules are built in Europe. The barrel modules production will be described in details in this section.

2.2.1 The BPIX upgrade project

The barrel modules production is conducted by four main consortia composed of production centres in Switzerland, Italy, Germany and Finland-CERN. Each consortium is appointed to build one or half of a layer of the barrel pixel detector (BPIX). The official production of BPIX modules of Layers 2-4 started on March 2015 and is expected to last one year. The final modules will be collected in Zurich, by ETH group and then mounted on the mechanical structure already built at the PSI Institute.

Since the modules for layers 2-4 are mechanically almost identical to the present pixel detector, the same mounting procedure will be followed. A tool exists to pick up a module and place it on the carbon fiber without risk of damage. The modules will be fully tested in each production centres. A quick test for cross-check is also done before the mounting on the final structure.

The production of components is unique for all the consortia. ROC wafers are produced by *IBM* and tested by PSI before any kind of re-working on them. Sensor wafers are instead produced by *CiS* while TBM and HDI by *HighTec*.

The BPIX module assembly consists of several steps, each one with specific criticality. Thus, the assembly line are different among the consortia and each of them has some peculiarity in the technology applied, jigs used and in the logistics. The main differences among centres lie on the technology used for the interconnection between ROCs and sensor (bump-bonding). This is a complex process and it is usually performed by an external vendor. Only the German consortia planned to do part of the bump-bonding *in house*. The topology of the bumps varies among the centres for the bump diameter (from 25 μm to 40 μm) and for the material used (SnAgCu, SnAg, SnPb, In). All these differences obviously do not have to reflect on the module performances and a final test with a common grading is applied to verify the uniformity of the modules.

The module qualification process, together with the INFN consortium production line is described below.

2.2.2 The module qualification

Each centre performs various quality assurance tests during the assembly line. Those present minor differences and are customised in relation to the assembly procedure. The final module qualification is instead done in each centre following a precise protocol and by using the same software for module testing and for interpretation of the results.

The module qualification procedure consists in three main steps: a full test of module functionality, an x-ray fluorescence for the module calibration and an high rate x-ray test to control the hit efficiency. These tests are performed using a test-board (DTB) designed

by the CMS PSI group and a custom software developed by the CMS community, named *pXar* [56]. The ROC functional test allows to find the proper working point of the ROC (timing, digital-analog currents, etc.) by setting the programmable DACs and to check the pixel efficiency and mask bit functionality by injecting internal signals. The proper connection of the bump-bonding is also checked by comparing the read-out from internal injected signal and a signal directly injected through the sensor (Fig. 2.18). Finally the ROC is trimmed and the pulse height is optimized to exploit the whole ROC dynamic range.

Looking at the results of those tests, the module is graded following a three grades code to indicate its quality and if it can be used in the final detector. This grading takes mainly into account the electrical performances (noise,etc.), the number of defective pixel (inefficient, bad bump bonding, mask bit defect, etc.) and the sensor performance. The functional test is performed in a cooling box at two temperatures (Fig. 2.19): $-20°$C and $+17°$C. The module is also tested after 11 thermal cycles inside the cooling box (Fig. 2.20) to simulate the thermal changes that will affect the module once it is installed in the experiment. The x-ray tests allows to cross-check the defective bump bonds and to measure possible inefficiencies under high rate.

All the test results are stored in a common database [57] and the calibration obtained with the x-ray fluorescence may be eventually used as a reference during the module commissioning. Considering the modules tested so far in different BPIX consortia, they can be trimmed to a reference threshold of 35 VCal with a typical RMS of 1.1 VCal. From the x-ray calibration, the conversion is measured to be around 46 $e^-/VCal$, as shown in Fig. 2.21. This leads to a trimming threshold of 1600 e^-, in perfect agreement with the design value. The mean noise per module is also measured to be equal to 150 e^- at $+17°$C.

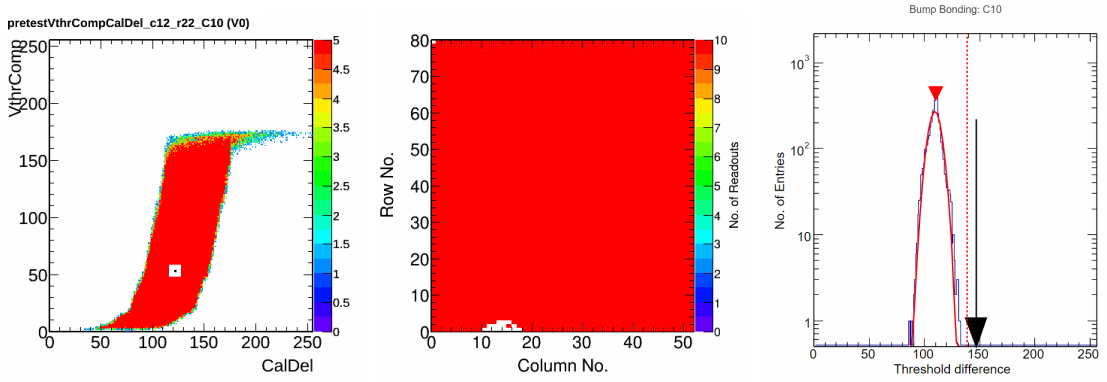

Figure 2.18: ROC timing calibration; working point is black marked (left). Pixel efficiency map for a single ROC; the white region corresponds to not responding pixels (center). Threshold difference distribution from the bump-bonding test; possible values above the 150 indicate not-connected bumps (right).

2.2.3 The INFN module production line

The BPIX module are produced by the INFN consortium following different steps distributed in 5 INFN section laboratories[1]: Pisa, Padova, Catania, Bari and Perugia. The

[1]In this thesis, the INFN laboratories will be referred to with the INFN section name only.

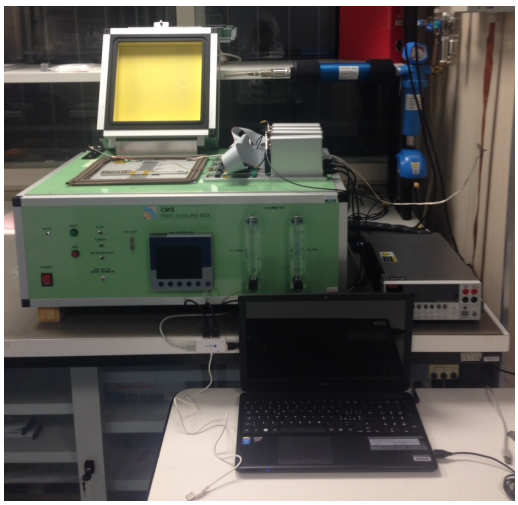

Figure 2.19: Photography of the cooling box used for the electrical qualification of the full modules produced by INFN; four modules can be tested in parallel.

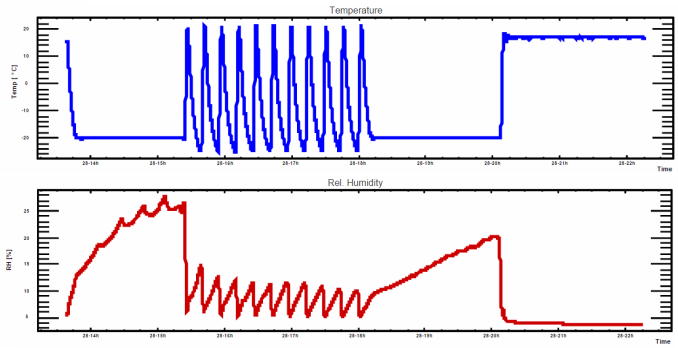

Figure 2.20: Graphs of the temperature and humidity variation inside the cooling box during a typical thermal test for the full module qualification.

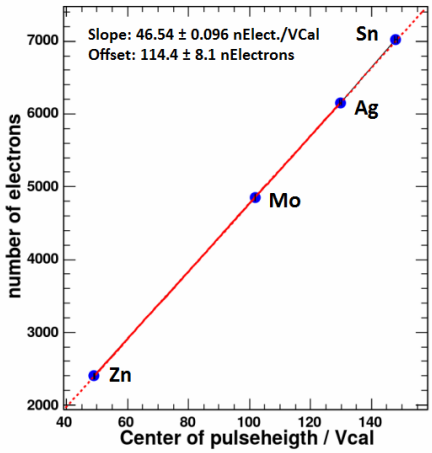

Figure 2.21: Calibration line from the x-ray fluorecence test made in INFN Perugia laboratory with four different targets [57].

components flow is described in Fig. 2.22 and the production line can be summarized into three main parts:

- Bare Module Production: coupling of 16 ROCs to one sensor, starting from ROCs and sensor wafers, plus assembly on two base strips;
- Full Module Assembly: gluing and wire-bonding of HDI, equipped with the TBM, on the bare module;
- Full Module Qualification: test of a full modules after assembly, including x-Ray and High-Rate test.

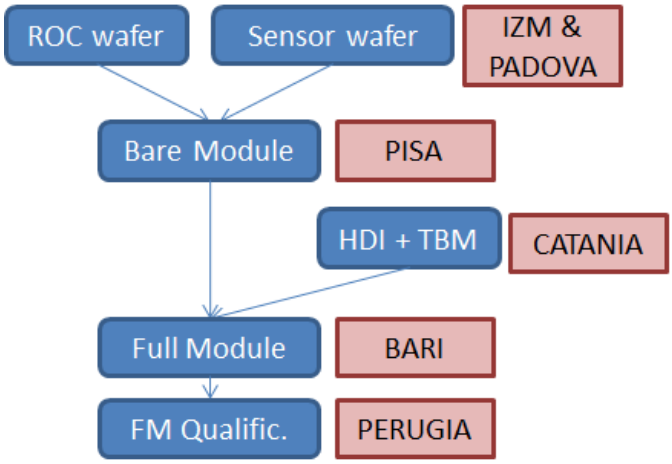

Figure 2.22: Schematic view of the INFN consortium production line.

2.2.3.0.1 Bare Module production The bare module assembly is a complex procedure that includes also thermal treatment and metal deposition on both the sensor and ROC pixel pads, and it is usually done by an external vendor. For the INFN consortium it is performed by the *Fraunhofer Institute for Reliability and Microintegration* (IZM), in Berlin.

The IZM receives ROCs and sensor on silicon wafers and, after several processes, 16 ROCs are assembled to one sensor. This process is crucial for the quality of the module and it will be described in details in Sec. 2.2.4.3. Once the bare module is assembled, it is shipped to Pisa where a quality assurance test is done.

In the event that a single ROC in the whole module is failing, due to, *e.g.*, short-cut or read-out problems, the bare module can be shipped back to IZM for the re-working process. This consists in the complete replacement of the flawed ROC with a new one thanks to a thermal treatment that allows to remove the single ROC without any damage to the sensor pixel structures.

The re-working process is robust and used by other consortia too. Otherwise, it is hardly time-consuming and it can interfere with the normal production work-flow. To minimize the faulty ROC in a bare modules, an electrical test on the ROC is performed in Padova before the module assembly. This procedure will be shown in Sec. 2.2.4.4.

The quality assurance test in Pisa includes also the measurement of the I-V curve for the sensor. To minimize the percentage of failing sensors on the bare module, the I-V test is performed also on the sensor wafer, before any processing or dicing. 324 sensors have been tested, divided in 5 different batches with an average yield of 84.5%.

Once the bare module has been qualified, it is glued on the two base strips by using

Araldite. Several precautions have been implemented to maintain a good planarity of the strips and to minimize the stress on the bump-bonds during the glue curing. In particular, the average warpage of the sensor is about 15 μm from centre to sides and it has been measured to be a native deformation coming from the *CiS* processing. Since the ROCs after assembly follow the sensors shape, it has been important to regulate the vacuum underneath the base-strips during the gluing process in order to force the base strips to be planar and not to follow the bare module bowing. This avoids stresses on the bump bonds and prevent several defects during the following assembly steps. The bare module qualification in Pisa consists thus in electrical test and I-V curve. These are shown in Fig. 2.23 for 30 bare modules.

The bare modules produced so far by the IZM are 148 and 109 of these have been tested in Pisa with a final yield of 82%. The main failures are due to I-V out of specifications after the IZM processing or to missing bump bonds in some areas of the module.

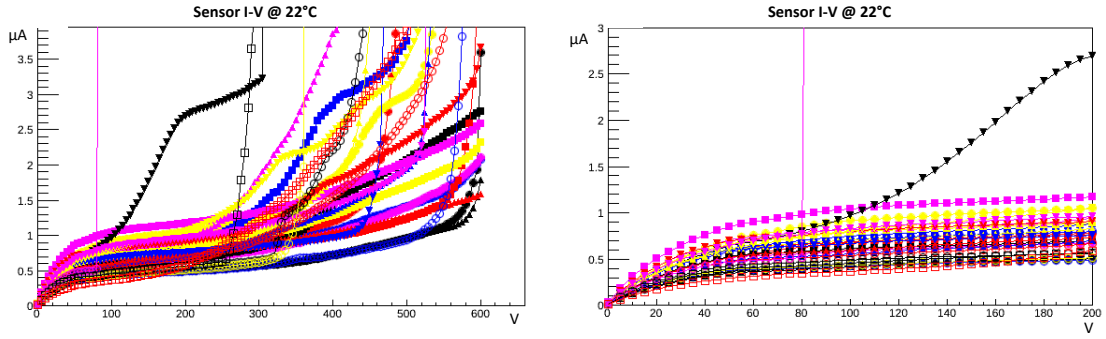

Figure 2.23: Sensor I-V curves from 30 bare modules measured in INFN Pisa laboratory; whole turn-on (left) and a zoom on the operative voltage range (right); one class C sensor is in breakdown at 80 V while another class B sensor has > 2 μm A at 150 V.

2.2.3.0.2 Full Module assembly and qualification The bare module glued on the two base strips is then shipped to Bari for the final assembly step. All these shipments are done with a commercial delivery and the modules are placed in customised module handle to minimize the mechanical stress, as shown in Fig. 2.24.

The full module assembly step consists in the mounting of the HDI on the bare module. The HDI, previously equipped with the TBM in Catania, is glued on the sensor surface with a commercial *Araldite 2000*. The curing time is 24 hours with a force applied on the HDI equal to $\sim$ 200 gr. After the curing, the pad of the HDI are wire-bonded to the ROC pads through *AlSi*(1%) wires of 25 μm diameter. In addition, the High Voltage pad in the sensor is wire-bonded to the HDI. The module is then complete and all the read-out chain can be tested. The typical time needed for a full module assembly is around two hours without considering the curing time. This process can be performed on three modules in parallel and therefore the planned throughput is three full modules per day. A first electrical test is made in Bari to check the number of defective pixels or bumps in the whole module and to control the HDI-TBM functionality. The full module is finally shipped to the INFN laboratory in Perugia to perform the full qualification.

The modules are fully qualified in Perugia, following the qualification procedure described in Sec. 2.2.2 and using the same grading criteria. An electrical test of module

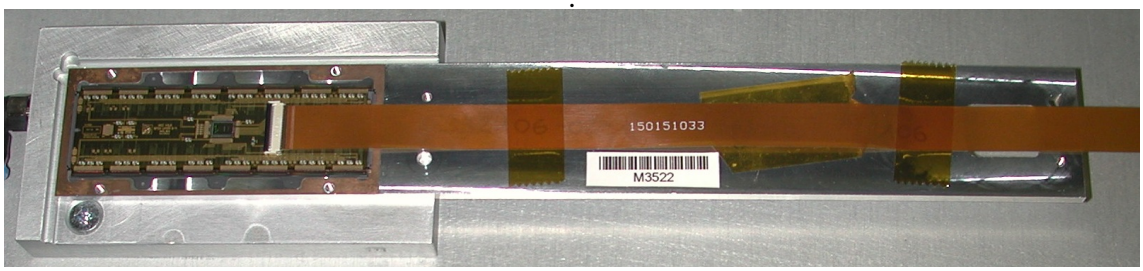

Figure 2.24: Photography of a full module produced by INFN, inserted in the custom module handle.

functionality is performed before and after the thermal cycles in the cooling box.

The fluorescence test is done by irradiating fixed target with an x-ray flux produced by a Mini-X Amptek tube (40 kV -90 μA). The target used are: Zinc (8.63 keV), Molybdenum (17.48 keV), Silver (22.16 keV) and Tin (25.27 keV). The module operates with a nominal bias voltage of -150 V. The high rate x-ray test is then performed using a 40kV tube and varying the current from 5 to 90 μA.

The full module assembly has been delayed respect to the bare module because of few problems occurred during the first part of the module production. Nearly all the first 20 modules have been down-graded because of the presence of defective pixels in some region of the modules (right and left corners of the module). This occurs systematically after the bare module test and the full module assembly. Several cross-check have been performed to debug the procedure and finally two main actions have been made: the jig for the bare module test have been changed and the custom module handle have been revisited.

The full modules assembled so far are 51. The functional qualification have been made on 36 modules with the following results: 18 grade C, 10 grade B, 8 grade A. 23 of these modules have been fully qualified with the high rate test and the final grading is: 15 grade C, 5 grade B, 3 grade A. Most of the grade C modules present cluster of not-responding pixels in particular regions, as previously mentioned. The test of modules assembled and tested with the new jigs will provide further information about the feasibility of the produced modules.

Except from these cluster of dead pixels, the performances of the modules are good and within the designed standard. The defective bumps in the INFN modules are usually less than 5 per modules, definitely lower than other BPIX production centers. A typical distribution of the threshold in the module before the trimming is shown in Fig. 2.25, together with the defective bump-bonds for one of the worst INFN module and with the hit map obtained from high rate test. The average noise per ROC and the x-ray calibration results are in agreement with the one from the other BPIX consortia.

2.2.4 ROC wafers quality assurance

The Read-Out Chip are produced by IBM in a 8 inch wafer with 244 ROCs each. The production process do not guarantee a perfect functionality of all the ROCs and a quality assurance test is obviously needed. This test is performed in the PSI laboratory for the whole BPIX project. The ROC wafer test is performed also in Padova laboratory for the INFN consortium, after the processing made by IZM. The setup is similar between the two centres and the test procedure is almost identical. I have directly collaborated with the PSI group for its development.

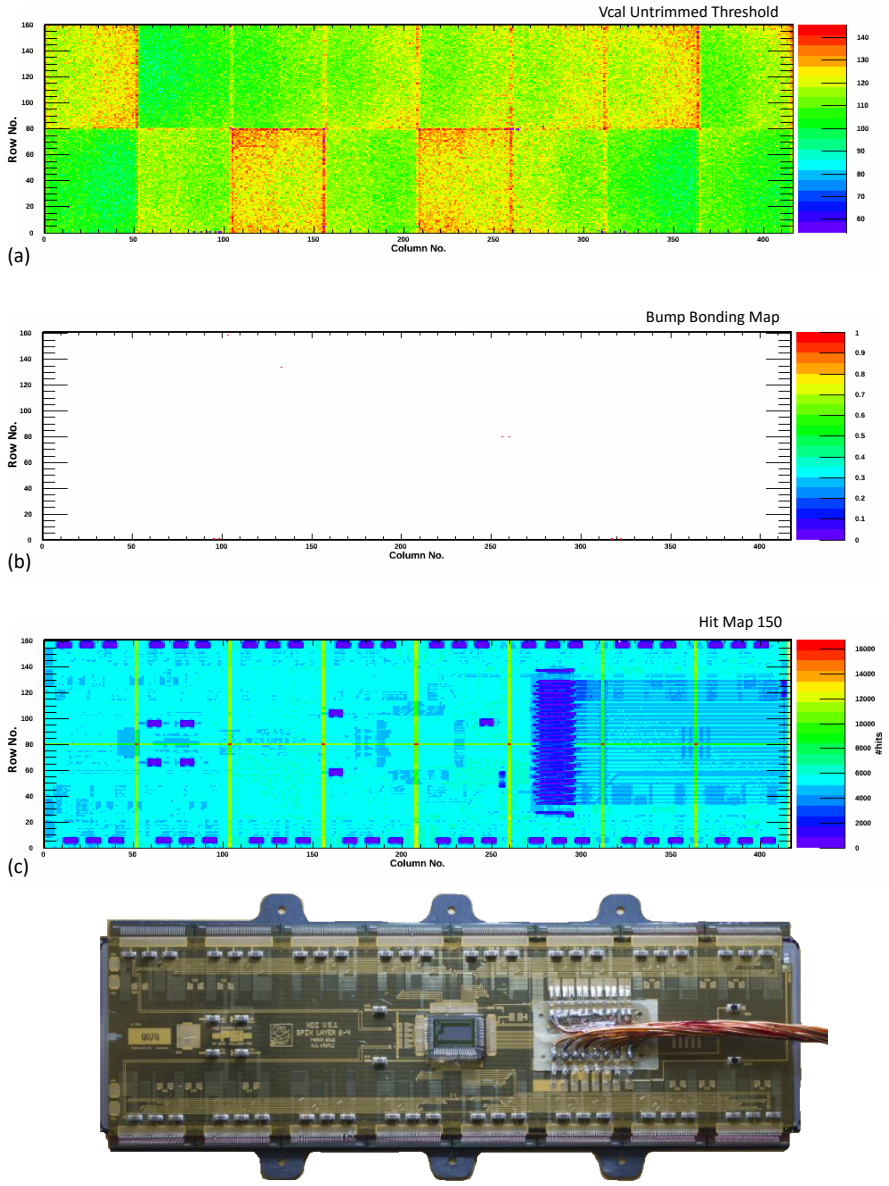

Figure 2.25: Photography of a full module plus three test maps on M3508 produced by INFN consortium: untrimmed Threshold distribution (a); Bump-Bond defects (b), the red ones correspond to not connected bumps; high rate hit map (c), the lower rate areas coincide with the structures on the HDI (glued on top of the sensor), separations between ROCs are also visible; the cable used during the test does not coincide with the final one (in the photography) [57]).

2.2.4.1 ROC wafer test description

The ROC is a complex object, as described in Section 2.1.5, and various components have to be tested to check its full functionality. Each readout chip wafer contains 61 reticle blocks with 4 ROCs each for a total of 244 ROCs per wafer. Therefore, not only the test steps but also each one speed are important in order to get a reasonable duration of the whole wafer test. The effective duration of each ROC test, after some optimizations, is around 30 seconds. The test setup and procedure is described below, together with results from PSI and Padova laboratories.

2.2.4.1.1 Test setup The ROC wafer test is performed in a clean room using a commercial probe-station that allows a controlled and automatic contact to the ROC pads, Fig. 2.26. The power ground, inputs and outputs connection to the ROC consist in 36 pads placed at the bottom part of the ROC, next to the periphery. Those pads are used to test the ROC on the wafer and after the bare module assembly. Once the HDI is assembled and wire-bonded to the ROC pads, the communication is handled by the HDI-TBM and thus the probe-station system is no more needed. The probes are held by and connected via a customised probe-card, a simple PCB for signal transfer.

The contact to the ROC is a crucial part of the test because it is necessary to not damage the ROC pads but it is also important to have a sufficient pressure to get a good connection of all the 36 probes. This is possible thanks to the probe-station automatic system and to a good planarity and alignment of the three elements involved: ROC, probes and chuck (support plate for the wafer). The wafer is placed directly on the chuck surface and vacuum is applied underneath.

A schematic view of the test setup is reported in Fig. 2.26. The Digital Testboard (DTB), developed for the entire Phase 1 Project, is used. It is connected to the probe-card via standard 68-pin SCSI ribbon cables and to a desktop computer via USB. The customised software *psi46test* [58], based on $C++$ programming language, has been developed to manage the test sequence and to interpret the DTB output. The psi46test manages also the direct communication to the probe-station via a RS-232 interface. Thus, mechanical movements of the probe-station and electrical command to the ROC are synchronized and integrated in a unique test procedure.

In a full module the communication to the ROCs is handled by the TBM and its internal 400 Mbit/s deserializer. In a single ROC test, this is replaced by a 160Mbit/s deserializer located in the DTB. The timing between the 40 MHz general clock and the deserializer is handled by a PLL. The synchronization among those components is essential and it has to be set once the setup is finalized. To do so, several signals which contain a token only are sent to the ROC and the frequency of token in the readout sequence is checked. A medium value is chosen between the possible full efficient DTB internal delays.

2.2.4.1.2 Test procedure The test starts with the placement and alignment of the wafer on the chuck and with the setting of the contact height. The timing between the testboard and the wafer are checked and fixed once per wafer. In particular, the synchronization among testboard clock and I2C signals has to be checked. It does not depend on the ROC under test and thus it is tuned only once. Then, per each ROC, the probes are moved to the contact position and a test routine starts. Depending on the result of the test routine, some ROC are tested twice to avoid rejection due to bad contact. Before this test repetition, the probes are automatically moved to separation and to contact position

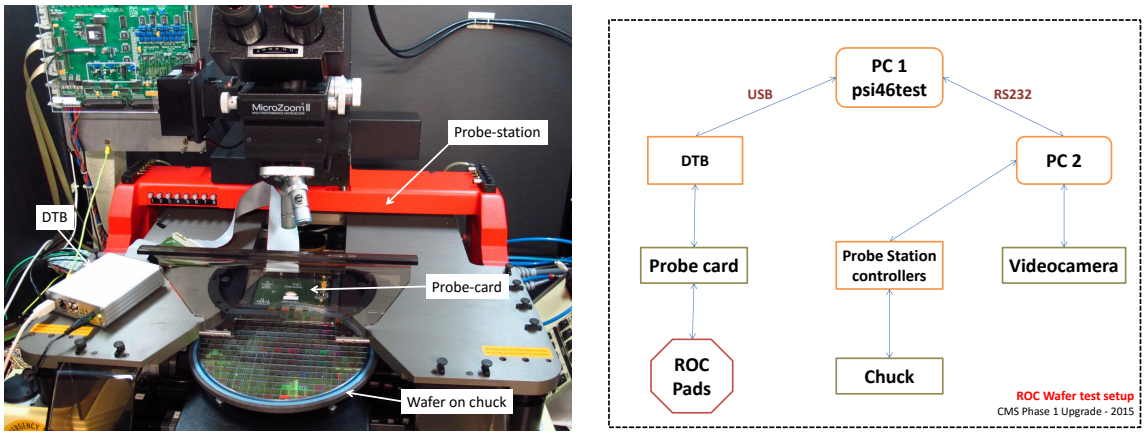

Figure 2.26: Photography (left) and schematic view (right) of the setup used for ROC wafer test.

again.

The ROC test routine can be divided into main sections:

- Power Up: the digital voltage is set to 2.5 V, the analog voltage to 1.5 V and the internal clock is set to 40 MHz. The digital and analog currents are read immediately after the contact to the ROC (*IdigOn, IanaOn,*). The ROC is programmed with default DACs value and currents are read again (*IdigInit, IanaInit*).
- Communication Check: an empty signal is sent to the ROC to check the token passage through the ROC periphery and to get a simple readout which includes the standard header only. A missing readout means a problem in the token flow inside the ROC and, since the testboard timing has been checked previously, the ROC is rejected to avoid synchronization problem once it is mounted in a module. Another check concerns the I2C communication. The internal voltage regulator (*Vana*) is increased and the current is sequentially read. A missing increment of the currents is interpreted as a problem in the I2C communication on the ROC side (since power issues are excluded due to previous check).
- Internal Setting: the Vana is trimmed to set the analog current to the design value of 24 $\pm$ 2 mA, fundamental to have the module current absorption under control (a good module should draw approximately 0.38 A (analog) and 0.48 A (digital)). Then, the full range of the register for the delay of the internal calibration signal injection (*caldel*) is scanned while an internal signal is injected. The operative value is set in the middle of the range with 100% response from the pixel. This step is necessary in any ROC test and it corresponds to one row of the plot in Fig. 2.18. In addition, the full range of the register for the internal calibration signal (*VCal*) is scanned and the relative increment of the PH is measured. This allows to check if the dynamic range of the ROC is correctly covered or if the DACs setting brings to saturation of the PH for too low value of the VCal.
- Pixel Map: this is the core of the pixels functionality check. The whole ROC is masked and each pixel is tested sequentially by unmasking and sending a internal signals. The signal is injected 10 times and the pixel response is checked. If there are less than 10 responses the pixel is marked as inefficient. The mask bit is also checked by masking the whole ROC and looking at eventual re-

sponse from each pixel after internal signal injection. Noisy pixels are checked by looking at spurious response from non-injected pixels. The pixel address decoding is firstly tested by checking the correspondence between addressed pixel and the address read in the readout sequence.

- Trim Bits Check: the trim bits are designed to allow a fine regulation of the threshold per each pixel and, as describe in Sec. 2.1.5, their functionality is fundamental to reach a uniform threshold trimming in the ROC. Each trimbit is sequentially activated and different signals are injected with incremental VCal values. The PH at which the pixel starts to respond is then read and compared with the one without that trimbit activated. A missing variation of these PH is marked as a faulty trimbit.

2.2.4.1.3 ROC grading criteria Four main defect types can be identified in a ROC: communication problems, non standard digital and analog currents, pixel defects, threshold and pulse height defects. Each of them can have a different impact on the ROC functionality and a classification of the defects has been implemented.

The list of the ROC failures is reported in Table 2.3 together with its description and corresponding class. The ROC classification is based on the one used for the current pixel detector, arranged to the new ROC features and structures. Class 5 ROCs are not usable due to lack of communication or internal short-cut. Class 4 still includes seriously damaged ROCs such as more than 40 defective pixels or mask bit defect. Class 3 includes mainly defects related to the threshold and pulse height distribution in the whole ROC. Class 2 includes only ROC with 1 up to 4 pixel defects. Class 1 instead indicates a ROC without failures detectable with this test.

The *pixel defect* in the grading includes:

- pixel inefficiency: less than 10 responses to internal signal injection;
- address defect pixel: readout address different from the one in input.
- mask defect: signal from masked pixel after a signal injection to it.
- trim bit defect: no differences between pulse height with trim bit on or off;
- noisy pixel: high signal from unmasked pixels after a signal injection to another pixel.

A grading among the possible pixel defects can be set. The mask bit allows to de-activate a noisy pixel in order to not saturate the relative double-column. Thus, a ROC with a single mask bit defect is automatically graded Class 4, such as an address defective pixel. In the Class 1 ROC instead, no defective pixels is allowed.

As for the checks on the ROC threshold, the aim is to reject ROC with anomalous differences in the pixel thresholds before the trimming (*untrimmed threshold*). All the ROCs can be trimmed to a determined threshold acting on the trim bits. However, if the differences among the untrimmed pixel thresholds are greater than 50 DAC units, it can be difficult to have a sharp and precise threshold distribution after the trimming. Thus, a cut on the untrimmed threshold standard deviation is applied. In addition, the mean untrimmed threshold of the ROC is required to be within 50 DAC unit from the average wafer value and the untrimmed threshold difference inside each single double column is also checked. Finally, requirements on the pulse height after the trimming are applied, in particular on the mean gain, the off-set and the pulse height differences inside the double columns. All the details of the grading are reported in Tab. 2.3.

The test log is analysed *off-line* using a second custom software (*grlog*[59]) to assign

Class	Failure	Description
5	shortcut	IdigOn or IanaOn >100 mA
5	IdigOn <5 mA	low current after power on
5	missing token	no token out
5	I2C error	not programmable registers
5	>4000 pix def	>4000 faulty pixels defects
4	>40 pix def	>40 faulty defects
4	mask def	1 or more pixels with defective mask bit
4	address def	1 or more pixels with defective mask bit
4	IdigOn >45 mA	high current after power on
4	IanaOn >10 mA	high current after power on
4	IdigInit	digital current not in [20-35] mA after DAC init
4	IanaInit	analog current not in [20-35] mA after DAC init
3	>4 pix def	>4 faulty pixels
3	Thr mean	ROC untrimmed threshold mean not in [85-135] DAC unit
3	Thr stdev	ROC untrimmed threshold standard deviation > 9
3	Thr col diff	Threshold difference >5 DAC unit in 1 or more DCOL
3	Ph Offset	Mean of PH for Vcal=40 not in [20-135] or its stdev >10
3	Ph Gain	Mean PH difference with Vcal=40-60 not in [30-60] or its stdev >4
3	Ph col diff	Difference of mean phdiff in two consecutive column >5
3	ID tolerance	IanaInit out of $\pm$3.5 from the ROC mean value
3	IA tolerance	IdigInit out of $\pm$6.0 from the ROC mean value
2	1..4 pix def	1 to 4 pixel defects
1	good	no failures

Table 2.3: List of the failure modes considered in the ROC wafer test.

the defined grade to each ROC, related to its specific failure. A wafer map consisting in a user-friendly color code representation of the fail and class grades is also drawn and report files are prepared as input for the official database.

2.2.4.2 PSI test results

The ROC wafers are tested in the PSI laboratory for the whole BPIX consortia to check the quality after the production by IBM. The total amount of *psi46digV2.1respin* ROC wafers produced so far for the BPIX modules production is 182, divided in 10 batches. They have been tested from October 2014 up to November 2015 using the procedure and the setup described above.

A non-diced wafer presents a regular and fixed positioning of the ROCs. This, together with particular software implementations, allows the test to be fully automatized without need of external action during the whole test. The ROC test takes around 30 seconds and a ROC wafer test takes approximately two hours. The Class 1 yield for the *psi46digV2.1respin* ROC wafers is particularly high and no criticality occurred. The average yield of the 182 tested wafers is 91.3% with a maximum of 98.4% and a minimum of 78.3%. Only 3 wafers have a yield lower than 80%, among which one wafer presents 66.8% yield, mainly due to $>$ 40 defective pixels inside $\sim$ 50 ROCs. This is the unique ROC wafer with an evident problem occurred in the production phase. The statistics of the failures is reported in Fig. 2.27 while the Class yield for the different batches can be seen in Table 2.4.

As expected, the major failure causes are related to defective pixels and short-cut inside the ROC. The average Class 1 yield variation from the different batches is 3% and this is reflected in relative classes yields. Both Class 1 and Class 2 ROCs have been used for

Class	n° ROCs	%	Batch n° 1 n° wafers = 20 %	2 23 %	4 25 %	5 26 %	7 25 %	8 23 %	9 25 %
1	39376	91.30	89.61	91.52	91.80	92.18	90.15	92.85	89.89
2	709	1.58	1.72	2.00	1.72	1.75	1.41	1.35	1.66
3	990	2.14	2.54	1.43	1.98	1.61	3.93	2.01	2.56
4	1745	4.18	4.90	4.26	3.59	3.59	3.89	2.83	5.03
5	368	0.80	1.23	0.80	0.90	0.87	0.62	0.94	0.87
Tot		100.0							

Table 2.4: Results of the 182 ROC wafers tested in the PSI laboratory; number of ROCs and relative percentage are reported per each grading Class and per batch.

the current pixel detector. Since the yield for the new ROC wafers is higher than in the past, only Class 1 ROC are used for the upgraded detector. The higher yield is surely a consequence of a more robust wafer processing made by IBM, probably combined with an improved design of the ROC and with the reduction of the number of internal programmable DACs.

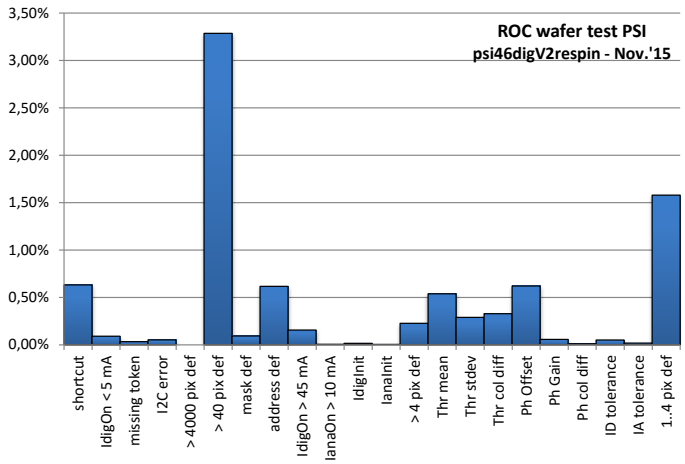

Figure 2.27: Failure modes percentage from the 182 ROC wafers tested in the PSI laboratory; failure modes are described in Tab. 2.3.

2.2.4.3 The bare module assembly process at IZM

The bare module assembly is a complex procedure to obtain a structure of 16 ROCs electrically and mechanically connected to one pixel silicon sensor. For the INFN consortium it is performed by the Fraunhofer IZM in Berlin. The IZM received 8-inch ROC wafers produced by IBM and 4-inch sensor wafer by CiS, previously tested respectively in the PSI and in Pisa laboratories.

The bare module assembly procedure is schematized in Fig. 2.28 and it can be divided in two main parts: the wafers processing and the flip-chip assembly. Several processes are performed on both the sensor and the ROCs wafers, some of them with temperatures between $22 - 250°C$. They consist mainly in the deposition of different layer of solder material on the pixel pads and on the dicing of the wafer. The octagonal AlSi pixel pad (10-15μm diam) have to be covered by the Under bump metallization (UBM) on both sensor and ROC side, while the solder bumps are deposited on the ROC pixel pads only.

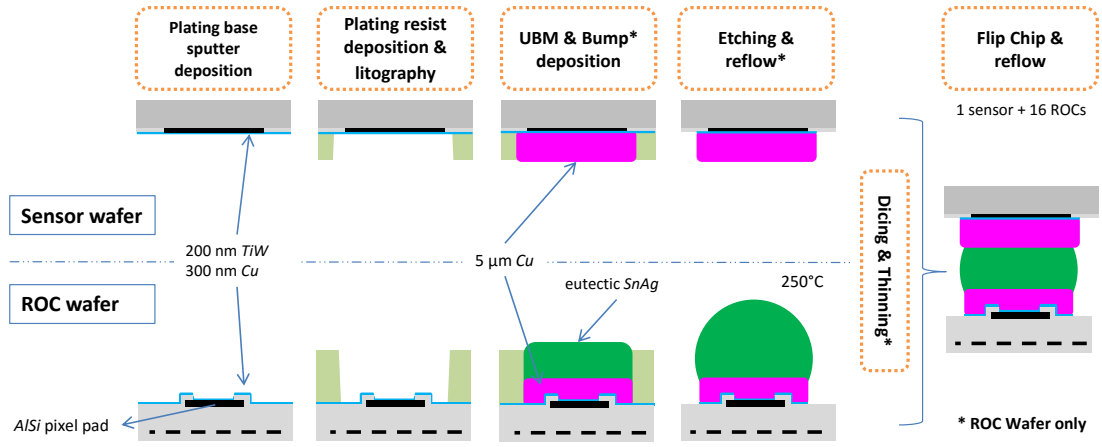

Figure 2.28: Schematic view of the bump-bonding process in IZM; the main steps are represented for one single pixel pad of both ROC and sensor wafer.

2.2.4.3.1 Sensor wafer processing A sputter deposition of the plating base, composed by 200 nm TiW and 300 nm Cu, is performed uniformly on the sensor wafer (300 μm thick), containing 3 pixel sensor. The process temperature depends on the sputtered material and other environment parameters and it is set up to a maximum of 150°C. A plating resist is then deposited on top of it and a lithography is performed to remove it from the pixel pad area. Then, a solderable Cu pad metallization layer of 5 μm height, called *Under Bump Metalization* (UBM), is deposited by electro-deposition. This is the effective contact layer on which the bump will be soldered. Finally, a wet chemical stripping/etch of the plating resist and plating base is done in order to remove the excess. The three sensor chip are diced, I-V test is performed and they are finally placed in a standard Gel Packs.

2.2.4.3.2 ROC wafer processing The ROC wafers, containing 244 chips each, need a deposition of 4160 bumps per ROC. Furthermore, the ROC wafers are initially 750-825 μm thick and have to be thinned to 175 ± 5 μm.

First processes are equal to the sensor wafer: sputter deposition of the plating base, plating resist and lithography. A 5 μm Cu UBM is deposited on the pixel pads. Differently from the sensor wafer, on the ROC pad also the bumps are deposited: a layer of eutectic solder composed by SnAg3.5. The wet chemical stripping/etch of the plating resist and plating base is done and finally the wafer undergoes the reflow.

After the deposition, this thermal process (up to 250°C) allows the formation of intermetallic compounds between UBM and solder material and to get to it a spherical shape, needed to optimize the connection with the sensor pad. The bump diameter is directly linked to the width of the deposited material and it is not equal in all the Phase 1 production centres because it mainly depends on bump material and reflow technique. Two options have been used by IZM, as it will be shown later, and the final choice is a bump diameter about 38 μm. After the reflow, an automatic bump inspection and classification is performed. The wafer is then thinned to the nominal value and diced by saw dicing. At this stage, the diced ROCs remain on the dicing-tape, approximately on the initial wafer position, and they are shipped to INFN laboratory in Padova to perform a full electrical

test and qualification.

2.2.4.3.3 Flip-chip assembly The bare module is effectively assembled with a so-called *flip-chip* mechanism. A single sensor is placed on a jig with the pixel pads on the upper side. Then, 16 ROCs are picked up from the gel-pack and placed on the sensor. This flip-chip is performed by a standard industrial tool which allows a placement accuracy of $\pm$ 3 μm. The second step is a solder reflow under reactive atmosphere with a max temperature of 260°C for less than 3 minutes. This allows a perfect soldering between the bumps and the UBM on the sensor side. A x-ray inspection is performed and the bare modules are finally placed on gel-pack and ready to be injected in the INFN production line.

2.2.4.3.4 Changes in the bump-bonding process The bump diameter is directly linked to the UBM diameter and it is not equal in all the Phase 1 production centres. The initial option for the INFN consortium was a UBM diameter of 30 μm with a consequent bump diameter of the same size. This dimension is used by the Swiss consortium and, in principle, a smaller bump is less subject to noise induction.

However, on the pre-production phase, many pixels in the ROCs were defective after the bare module assembly. It has been discovered that a crack appears underneath the ROC pixel pad starting from the end of the UBM and base plate, as shown in Fig. 2.29. Most of the cracks have been found between the passivation and the top metal layer of the ROC pixel pad. The reason of these cracks is not univocally determined and it can be associated to the increment of the thickness of the top metal option for the upgraded ROC and to a bump structure rigidity.

The nominal thickness of the top layer of the new ROC, which consumes more power, has been moved from 0.73 μm of the current ROC to 1.0 μm, and consequently the top passivation width has been enlarged by 270 nm. This probably leads the ROC pixel pad region to be more vulnerable to stress. The solution chosen is to extend the UBM up to 38 μm and thus also the bump diameter, see Fig. 2.30. In this way, the UBM does not end exactly at the end of the aluminium pixel pad and there are less longitudinal forced applied on ROC pixel pad. All sensitive circuits are well shielded and this larger metal deposition does not induce any mechanical damage.

All the final modules, produced by INFN consortium so far, are with this larger bumps. The pixel failure after the bare module assembly are no more present and the noise induced by the larger size of the bumps is negligible. However, an intrinsic rigidity of the bump is still present and it requires a careful handling of the bare modules up to the final assembly stage.

2.2.4.4 Padova test results

As described in Sec. 2.2.3, to minimize the faulty ROC in the bare modules produced by INFN consortium, an electrical test on the ROC is performed in Padova laboratory before the module assembly.

The ROC wafers are shipped from IZM laboratories after the dicing, thus the ROCs are already thinned with UBM and bumps deposited on the pixels. The reason for this is that it is preferable not to perform a cleanness process before the module assembly and the presence of dust particles in the experimental area has to be avoid. The tests are performed in a laminar flow box with controlled temperature and humidity.The wafers

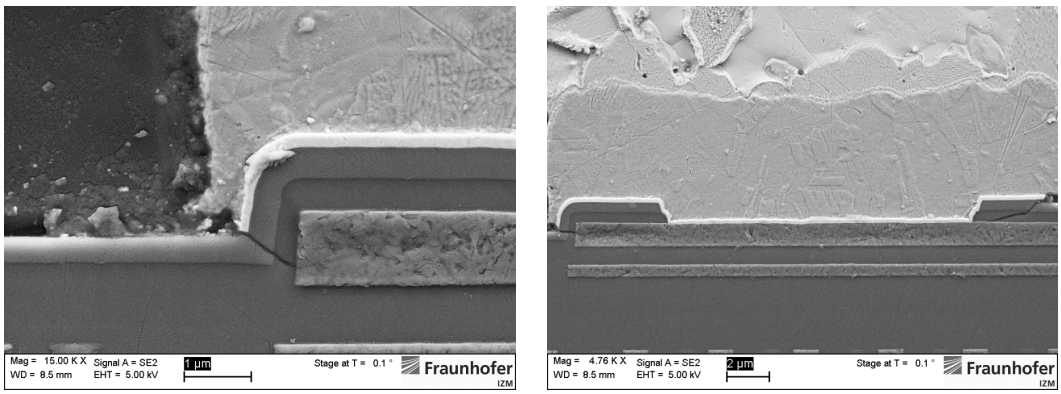

Figure 2.29: Section of a ROC zoomed on two different pixel pads (left and right) after bump deposition and reflow; the bump is a pre-production type with a 30 μm diameter; cracks are present next to the pixel pad, starting exactly at the end of the UBM and base plate; courtesy of IZM.

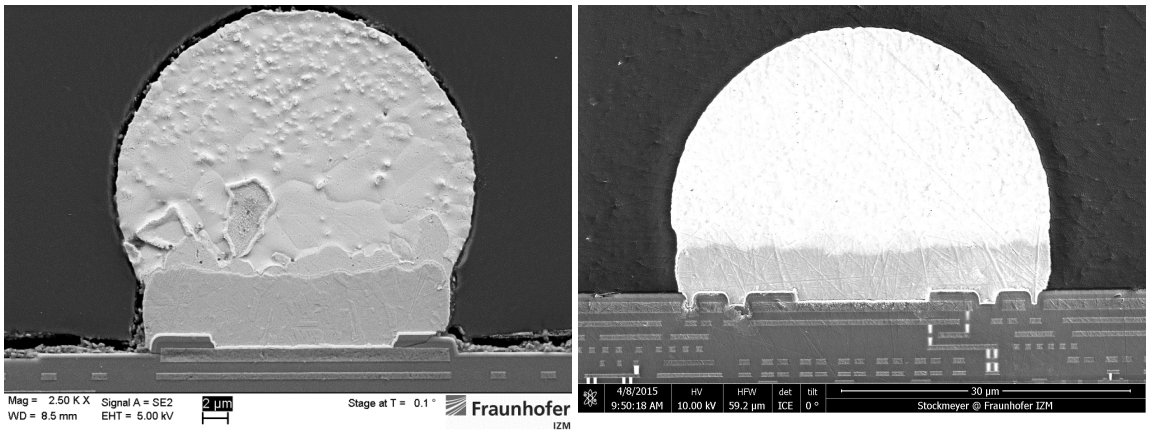

Figure 2.30: Section of two ROC zoomed on a pixel pad; one ROC has a pre-production bump with 30 μm UBM diameter (left), the other has a production bump with 38 μm UBM diameter (right); courtesy of IZM.

are handled in a dedicated area underneath these filters, see Fig. 2.31.

The ROC wafers are placed at IZM on a standard blue-tape to perform the dicing procedure. The ROCs remain in that dicing frame even for the test in Padova and they are removed only for the module assembly procedure in IZM. For the shipment, the frame is inserted in plastic case which in turn is placed in an antistatic and hermetic bag. No additional precautions are taken for the commercial shipment from and to IZM.

The test setup is similar to the one used at PSI and described above. The same probe-card and DTB are used, as it can be seen in Fig. 2.31. The main difference consists in the fact that the wafers have already been diced and there is not a regular and fixed distribution of the ROCs anymore. This leads to the necessity of a manual re-alignment between the probes and ROC pad, and therefore a full automatised procedure is not feasible. However, the dicing tape is not stretched after the dicing and the misalignment between ROCs is of the order of tens micrometers. By recording a customised maps of coordinates in the test software, it is possible to automatically move the probes on the ROC with this order of precision and the required manual alignment keep only 15-20 seconds more than the ROC test itself. The dicing tape is placed directly on the standard chuck of the probe-station and vacuum is applied underneath.

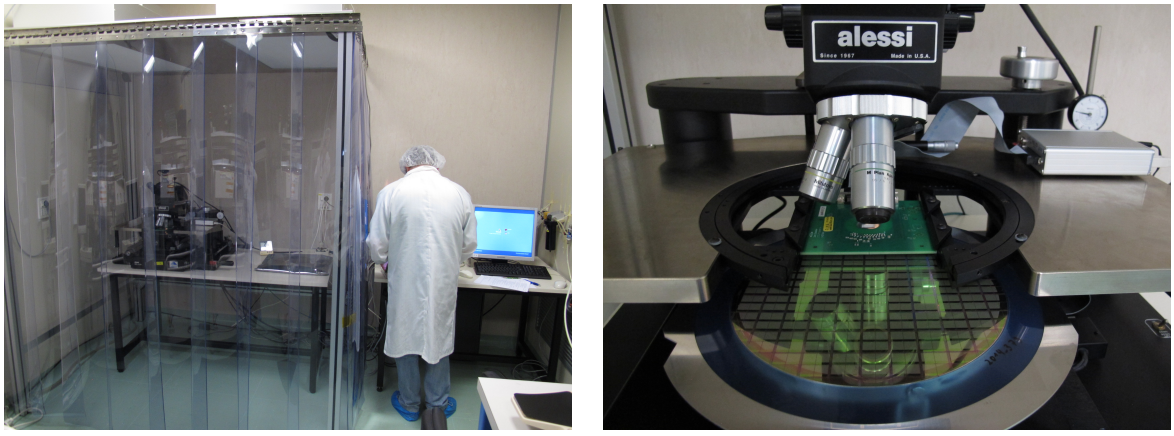

Figure 2.31: Photography of the setup used for the ROC wafer test in Padova INFN laboratory: test area (left) and probe-station with ROC wafer on (left).

The purpose of the test is to check the functionality of the ROCs after the processing made at IZM. A priori, the main damages on the ROC can be caused by the thinning and dicing processes. Thus the standard procedure is to perform a simple test to check the analog and digital currents in the ROC and the pixels functionality. However, this does not take into account possible failures coming from changes in threshold or pulse height behaviour. These can eventually consist in a worsening of previous not well-performing ROC, due to the mechanical or thermal stresses. Therefore, the choice for the test after dicing has been to perform a complete test, following the same procedure described above.

The test is performed on all the ROCs in the wafer, not only the *Class 1* from PSI. This allows a direct comparison with previous PSI test results, it gives a complete overview of each wafer and it allows to have a cross-check of the test itself. The grade criteria shown in Tab. 2.3 are used. The unique change consists in the shift of the allowed range for the mean untrimmed threshold.

A systematic shift in the mean threshold value has been observed in each wafer in

Class	n° ROCs	%
1	3805	86.6
2	100	2.3
3	165	3.8
4	246	5.6
5	76	1.7
Tot		100.0

Table 2.5: Results of the 18 ROC wafers tested in the Padova INFN laboratory; number of ROCs and relative percentage are reported per each grading Class; the whole set of ROCs is considered.

	PSI	IZM	Padova	Final
down-graded ROCs	355	47	227	629
Yield (%)	91.9	98.9	94.8	85.9

Table 2.6: Number of down-graded ROCs for the 18 wafers and relative Yield after test at PSI laboratory, IZM optical inspection, Padova laboratory.

Padova respect the value measured during PSI test. This can depends on the setup environment but also on the presence of bump structure on the pixel. Since the shift affect uniformly the whole wafer, the allowed range for the mean untrimmed threshold has been shifted of 20 dac unit and it is equal to [95-150].

The *psi46digV2.1respin* ROC wafers tested so far in Padova for the final BPIX production are 18. The faulty ROC in the test performed at PSI have a perfect match with the test results in Padova. The classes percentage of the whole set of ROCs tested in Padova is reported in Tab. 2.5. Considering only the ROC down-graded in after the Padova test, the average yield is 94.8% with a maximum of 98.8% and a minimum of 91.4%. One wafer was accidentally scratched by the SCSI cable during the test phase. Several bumps were removed on the top part of the wafer and some electrical failures also occurred with a final yield equal to 75%.

The Padova yield has to be summed also to the fraction of ROC rejected by IZM after an optical inspection. The ROCs rejected by IZM are usually 1-2 chips at the edge of the wafer due to an incomplete bump matrix in the chip corner close to the wafer edge. In Table 2.6, the average yield for PSI, IZM and Padova is reported the comparison between PSI and Padova test is shown in Fig. 2.32. Two particular wafers are reported: in the ROC wafer AWGNNTX is visible a cluster of ROCs (violet) where the mean untrimmed threshold is out of the allowed range; in the A6GNK2X a central column of the wafer present all the ROCs with a single pixel defect on the top right corner (blue), this systematic defect has been observed in this wafer only.

The statistics of failure causes for the ROC down-graded after the test in Padova is reported in Fig. 2.33. The main cause is the increase in the number of defective pixels with respect to PSI test. About 15% of the $>$40 pixel defects category are due to the accidental damage mentioned before, such as $\sim$32% of the shortcut category. The single-pixel defects are mainly due to one defective pixel placed on the top corners of the ROC.

A $\sim$10% of the down-grading is related to defect in pulse height and threshold distribution. Among these, a common trend has been detected: the four ROCs on the left part of each wafer, next to the wafer label, usually present an higher gradient of untrimmed threshold as shown in Fig. 2.34. The standard deviation of the untrimmed threshold distribution (*VTtrhStdev*) is therefore greater than 9 and those ROCs are rejected for the final production. No particular process performed on the wafer should affect the ROC in such a position. Nevertheless, the value of the VTtrhStdev are higher in the left part of the wafer also during the test made at PSI before any processing, see in the wafer map in

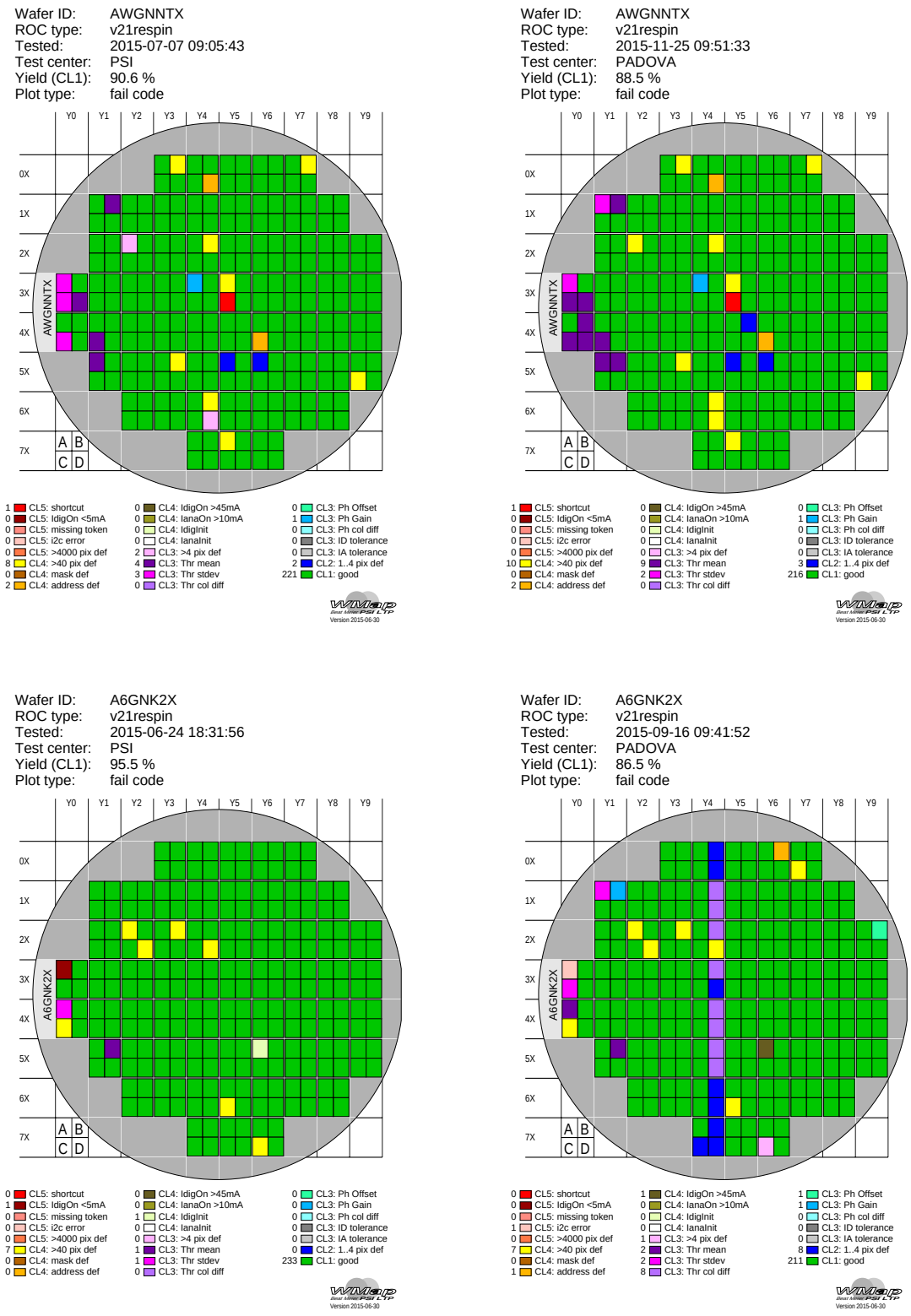

Figure 2.32: Failure map for ROC wafer AWGNNTX (up) and A6GNK2X (down); both maps from tests at PSI laboratory (left) and at INFN Padova laboratory (right) are shown; the failure mode color code is reported.

Fig. 2.35. This is an indication of an intrinsic feature of the wafer, probably due to production methodology. No other systematic change has been observed in those 18 ROC wafers.

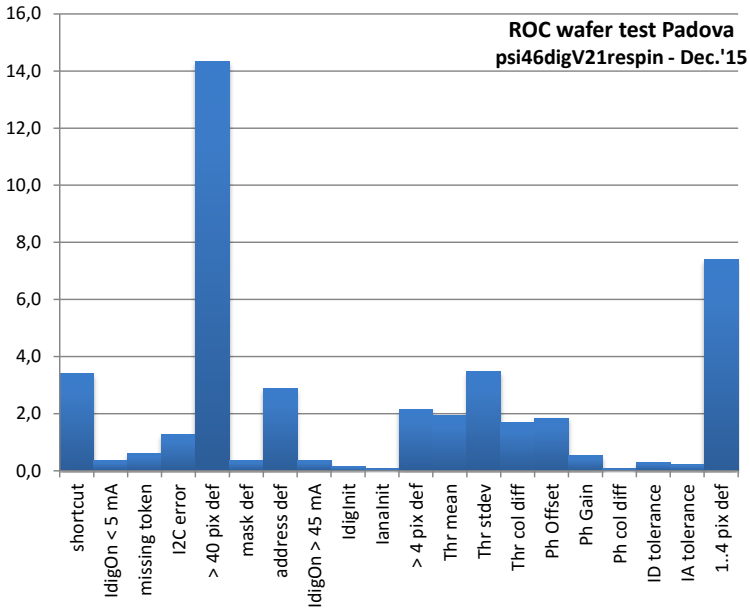

Figure 2.33: Failure modes percentage from the 18 ROC wafers tested in the Padova laboratory after the processing made by IZM; only ROCs down-graded after Padova test are considered.

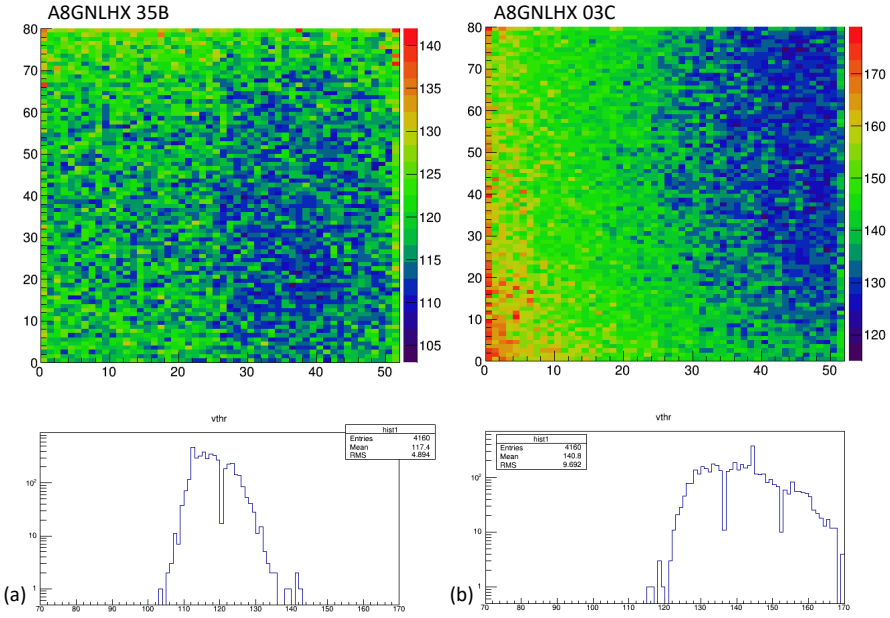

Figure 2.34: Untrimmed threshold distribution for a typical ROC (a) and for a ROC placed next to the wafer label (b); ROC maps are from test after IZM processing.

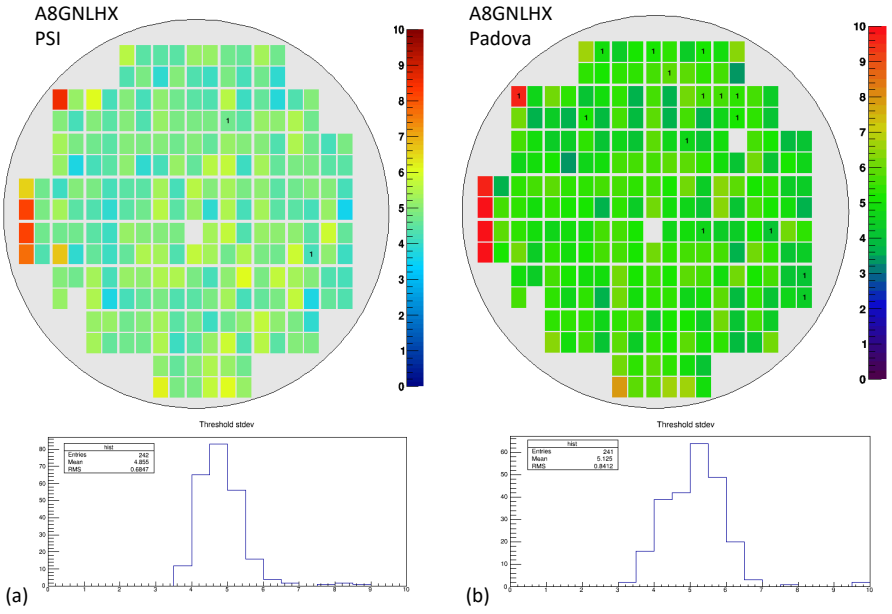

Figure 2.35: Standard deviation of the untrimmed threshold per wafer before (a) and after (b) the processing made in IZM.

Chapter 3

Higgs bosons pair production

3.1 The Standard Model

The Standard Model of particles physics (SM) classifies the elementary particles that are present in nature and their fundamental interactions: the electroweak (EW) and the strong interaction. The SM does not include the gravitational force but it still provides a comprehensive description of the nature at the subatomic scale, since the gravitation can be neglected with respect to the amplitude of the previously mentioned interactions[1].

The SM is a Quantum Field Theory (QFT) [61] and its structure relies on the invariance of the Lagrangian to the gauge transformation symmetry group G_{SM}, which determines the interactions between the fundamental particles

$$G_{SM} = SU(3)_C \otimes SU(2)_L \otimes U(1)_Y. \tag{3.1}$$

$SU(2)_L \otimes U(1)_Y$ group represents the EW interaction which comes from the theoretical unification of the weak interaction with the electromagnetic interaction, theorised in the sixties by Glashow [62], Weinberg [63], and Salam [64]. The electromagnetic interaction is based on the abelian $U(1)_{em}$ group and it is described by the Quantum Electrodynamics theory (QED) [65, 66]. The $SU(3)_C$ group is instead the base of Quantum Chromo-Dynamics (QCD) [67], which refers to the strong interactions and is assumed to be an exact symmetry.

The particles in the SM are identified as excited state of gauge field and have intrinsic properties, such as the *spin* [68] and a charge linked to each interaction: electric charge in the QED, flavour charge for the weak interaction and color charge in the QCD. The matter is described in terms of *fermions* and *bosons*. The first are half-integer spin elementary particles while the latter are spin 1 particles responsible for the mediation of the force, thus called *mediator*. Each group of symmetry, i.e. each fundamental interaction, include at least one gauge boson for a total of 12 in the SM. The electroweak interactions are mediated by the massless and electrically neutral photon γ and by the massive gauge bosons $W^{\pm}$ and the neutral Z_0. The strong force instead is mediated by eight massless *gluons* (g), which are self-interacting and with a different color charge.

The fermions are divided into 3 generations of fermions and a single spin-0 scalar, respectively represented under the G_{SM} group as *Weyl* spinors and as a complex doublet. The three fermions generations include right-handed and left-handed Weyl spinors and can be divided into 2 fundamental field types (Tab. 3.1): 6 *quarks* and 6 *leptons*.

[1] The energy scale at which quantum gravity effects are expected to become important is of the order of 10^{19} GeV, the so-called Planck scale [60].

The existence of the quarks, as the truly fundamental matter fields, has been independently postulated by Gell-Mann [69] and Zweig [70] in the 1964. In addition to the three generations, they can be divided by looking at their fractional electric charge: the *up* type quarks (u, c and t) with charge $+2/3e^-$, and the *down* type quarks (d, s and b) with charge $-1/3e^-$. The six leptons can also be divided, looking at the electric charge, into the charged (e, μ, τ) and the corresponding neutral spinors called neutrinos (ν_e, ν_μ, ν_τ). For each fermion, an *anti-particle* is included in the SM, with the same properties of the relative fermion but opposite electric charge. The fermions described so far are the basic objects of the matter, as commonly defined.

	Generation						
	First	Second	Third	Q	$U(1)_Y$	$SU(2)_L$	$SU(3)$
Leptons	$\begin{pmatrix} \nu_e \\ e \end{pmatrix}_L$	$\begin{pmatrix} \nu_\mu \\ \mu \end{pmatrix}_L$	$\begin{pmatrix} \nu_\tau \\ \tau \end{pmatrix}_L$	0 -1	-1/2	2	1
	ν_{eR}	$\nu_{\mu R}$	$\nu_{\tau R}$	0	0	1	1
	e_R	μ_R	τ_R	-1	-1	1	1
Quark	$\begin{pmatrix} u \\ d \end{pmatrix}_L$	$\begin{pmatrix} c \\ s \end{pmatrix}_L$	$\begin{pmatrix} t \\ b \end{pmatrix}_L$	+2/3 -1/3	+1/6	2	3
	u_R	c_R	t_R	+2/3	+2/3	1	3
	d_R	s_R	b_R	-1/3	-1/3	1	3

Table 3.1: The SM fermions quantum numbers under the $SU(2)_L \otimes U(1)_Y$ symmetry group, for the left- and right-handed components.

3.1.1 The strong interaction

The interaction between the quark fermionic spinor fields and the relative vector bosons is described by the Quantum chromodynamics (QCD). QCD is associated to the non abelian $SU(3)_C$ symmetry group which has eight massless spin-one gauge bosons, the gluons. They are charged mediator of color flow (i.e. carrying color and anti-color) and, due to the non-abelian nature of the QCD, they can interact with each other. Quarks and anti-quarks are the simplest representations of this group and different bound states follow from their interaction. In particular, from their product a bilinear singlet and an octect are obtained, corresponding respectively to *mesons* ($q\bar{q}$ structure) and *baryons* (qqq structure), collectively denoted as hadrons.

The QCD Lagrangian can be described by the following equation:

$$L_{QCD} = \bar{\psi} i\gamma^\mu D_\mu \psi - \frac{1}{4} G^a_{\mu\nu} G^{\mu\nu}_a \tag{3.2}$$

where ψ is a generic massless quark spinor field, and $G^a_{\mu\nu}$ is the field tensor of the fields associated to gluons. The covariant derivative of QCD is described using the λ_a Gell-Mann matrices [69], as:

$$D_\mu = \delta_\mu + \frac{i}{2} g_s \lambda_a G^a_\mu \tag{3.3}$$

where the QCD coupling constant (g_s), can also be rewritten to as $\alpha_s \equiv g_s^2/4\pi$.
Due to the renormalization process of the theory, the QCD coupling constant α_s varies depending on the transferred momentum Q, the so-called α_S running. Thus, the strength of the force between particles with non-null color charge increases with the distance, leading to a complex dynamic which cannot be described perturbatively. In a short range

distance, i.e. high-energy regime, QCD is instead well described in terms of weakly-interacting quarks and gluons allowing a perturbative description of the relative interactions. This phenomenon is the so-called *asymptotic freedom* and it is in opposition to the *quark confinement* which appears at a determinate energy scale. The characteristic energy scale at which this effect become important is $\Lambda_{QCD} \sim 1/\text{fm} \sim 200$ MeV, approximately the light hadron mass scale. Thus, a coloured object produced in a collider cannot exist individually. Pairs of quarks and anti-quarks are produced from the vacuum and combined with gluons and the original quark until formation of colourless objects such as hadrons, process called *hadronization*. Predictions for hadron formation are obtained using Monte Carlo models, tuned on experimental results. Phenomenological models are usually applied in order to describe completely the results of the hadronization process.

3.1.2 The electroweak interaction

The gauge theory of the electroweak interaction is based on the invariance under $SU(2)_L \otimes U(1)_Y$ gauge transformations. The constituent of the electroweak interaction are left-handed (L) weak isospin doublets ($T = 1/2$), while the right-handed components transforms as singlets. Charged leptons and quarks interact under the electroweak symmetry with both left-handed and right-handed components while the neutrino left-handed component only is present in the SM.

The boson fields involved in the $SU(2)$ gauge symmetry are the three W^a_μ, related to the Pauli matrices τ_a and to the gauge coupling constant g. The B_μ boson field arise instead from the $U(1)$ symmetry, with coupling $g^{'}$. The electroweak Lagrangian is written as:

$$L_{EW} = \bar{\psi} i \gamma^\mu D_\mu \psi - \frac{1}{4} W^{a\mu\nu} W^a_{\mu\nu} - B_{\mu\nu} B^{\mu\nu}, \tag{3.4}$$

where the covariant derivative actions on the generic spinor field ψ is different between left doublets (L) and right singlets (R):

$$D^L_\mu = \delta_\mu + \frac{i}{2} g \tau^a W^a_\mu + \frac{i^{'}}{g} Y B_\mu \tag{3.5}$$

$$D^R_\mu = \delta_\mu + \frac{i^{'}}{g} Y B_\mu \tag{3.6}$$

These four boson fields do not represent the observable states of the vector bosons responsible for the weak (charged and neutral) currents and the electromagnetic interaction. The physical fields A_μ, Z_μ , W^+_μ and W^-_μ, corresponding respectively to the photon, the Z_0 and $W^\pm$ bosons, are in fact described within the Glashow-Salam-Weinberg electroweak theory as linear combinations of the W^a_μ and B_μ fields:

$$A_\mu = \sin\theta_W W^3_\mu + \cos\theta_W B_\mu \tag{3.7}$$

$$Z_\mu = -\sin\theta_W B_\mu + \cos\theta_W W^3_\mu \tag{3.8}$$

$$W^\pm_\mu = \frac{1}{\sqrt{2}} \left(W^1_\mu \pm W^2_\mu \right), \tag{3.9}$$

where θ_W is the Weinberg electroweak mixing angle. The coupling constants g and $g^{'}$ are linked to θ_W and to the electromagnetic coupling constant (the electron charge e) through the relation:

$$e = g \sin\theta_W = g^{'} \cos\theta_W. \tag{3.10}$$

The A_μ field is related to the physical photon and it is parametrized to be the boson field of the abelian $U(1)_{em}$ group.

3.1.3 The EW spontaneous symmetry breaking

The invariance of the SM Lagrangian under the electroweak symmetry group requires the presence of four gauge bosons. On the other hand, the limited range of the weak interaction implies their mediators to be massive, as it has been also confirmed by the experimental observations of the $W^{\pm}$ and Z bosons [71]. However, massive gauge bosons can be described in the SM with a gauge symmetry breaking only. A possible solution to this problem has been independently proposed in the 1964 by three groups of theorists. A complex scalar field with non-zero vacuum expectation value was introduced into the Lagrangian, resulting in the breaking of the symmetry of $SU(2)_L \otimes U(1)_Y$, better known as *spontaneous symmetry breaking*.

This mechanism is called *Englert-Brout-Higgs-Guralnik-Hagen-Kibble, PhysRevLett.13.508, PhysRevLett.13.585* mechanism [72], or simply the Higgs mechanism, and it can be mathematically described by the introduction of a Higgs scalar doublet, a complex $SU(2)_L$ doublet written as:

$$\Phi = \begin{pmatrix} \Phi^+ \\ \Phi^0 \end{pmatrix} = \frac{1}{\sqrt{2}} \begin{pmatrix} \phi_1 + i\phi_2 \\ \phi_3 + i\phi_4 \end{pmatrix}. \tag{3.11}$$

A generic Lagrangian describing the evolution of the scalar field Φ can be written as follows:

$$L(\Phi) = D_\mu \Phi D^\mu \Phi^\dagger + V(\Phi), \tag{3.12}$$

where D_μ is the covariant derivative under the $SU(2)_L$ group transformation and the potential term $V(\Phi)$ is:

$$V(\Phi) = \mu^2 \Phi^\dagger \Phi + \lambda |\Phi^\dagger \Phi|^2, \tag{3.13}$$

with a mass term $\mu^2 < 0$ and the self-interaction term $\lambda > 0$. This potential is symmetric under gauge rotations in the field Φ space and it presents the well-known 'mexican hat' shape shown in Fig. 3.1.

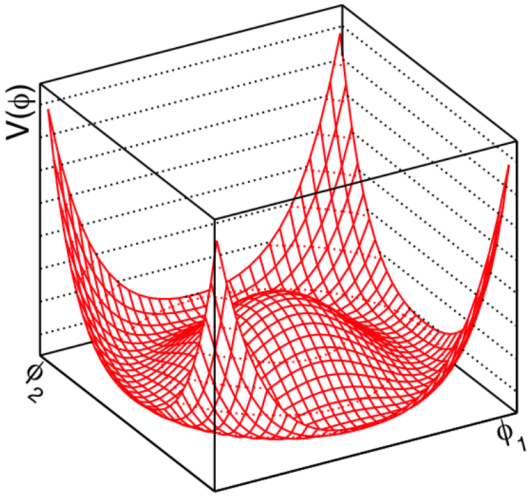

Figure 3.1: Shape of the potential of the Higgs scalar field described in Eq. 3.13.

The potential minimum is not null and a degenerate set of minima is instead present. The choice of a state in the local minima of the potential is arbitrary under gauge rotation

and it leads to the symmetry breaking. After the choice of a state in the local minima of the potential, the system state is not symmetric anymore under SU(2), and the chosen coordinate is not invariant under transformations in the (Φ^+, Φ^0) space. However, the gauge theory still remains renormalizable and its symmetry is, in a sense, still present. It is somehow hidden by the choice of the ground state which leads also to the presence of a non-null mass term. This happens without any explicit insertions of gauge mass terms in the Lagrangian, which would removed the renormalizability, that is why it is called spontaneous symmetry breaking.
The ground state can be forced to be along ϕ_0, so-called unitary gauge. The Higgs boson field is thus:

$$\Phi(x) = \Phi_0 + h(x) \tag{3.14}$$

where $h(x)$ represent a fluctuation around the vacuum expectation value. Before the spontaneous symmetry breaking of the electroweak gauge symmetry group there are four massless scalar fields ϕ, known as Goldstone bosons [73], each one with one degree of freedom. After this ground state choice, only one real scalar field $h(x)$ remains, which coincide with the physical Higgs boson.
The relative potential, defined in Eq. 3.13, can be expanded to the second order in h:

$$V(x) = V_0 + \lambda v^2 h(x)^2, \qquad v = -\frac{\mu^2}{\lambda}. \tag{3.15}$$

where the v term represents the Higgs boson field vacuum expectation value and the mass term appear to be:

$$m_H = \sqrt{2\lambda v^2} = \sqrt{2}|\mu|. \tag{3.16}$$

Since the parameter λ is unknown in the theory, the mass of the Higgs boson is a free parameter of the SM. The remaining three missing degrees are instead absorbed by the $W^{\pm}$ and Z_0 physical bosons, which in turn acquire their mass via the coupling with the $h(x)$ field, proportional to v. Applying it to the EW Lagrangian, the vector boson masses results to be:

$$M_W = \frac{vg}{2},\ M_Z = \frac{v\sqrt{g^2+g'^2}}{2}, \tag{3.17}$$

where g and $g^{'}$ are the coupling constants described in 3.1.2.
Since the A_μ field is related to a $U(1)_{em}$ gauge symmetry, the interaction with the $\Phi(x)$ field leads to a null mass term and thus to the massless photon.
The same Higgs mechanism can be applied also to the fermion and it provides mass to quarks and leptons too. The scalar Higgs field couples with fermion states (f) of opposite *helicity* and the resulting fermion mass term is:

$$m_f = \frac{g_f v}{\sqrt{2}} = \frac{\sqrt{2} g_f M_W \sin\theta_W}{e} \tag{3.18}$$

where g_f is the coupling constant between the Higgs boson and $f\bar{f}$, proportional to m_f. This direct proportionally leads to a negligible coupling of the Higgs boson to the light quarks and therefore to more difficulties in the Higgs boson discovery.

3.1.4 The SM Lagrangian

The SM Lagrangian can be obtained by summing together all the previously mentioned contributions: the EW and QCD terms, plus the additional term coming from the Higgs

mechanism and their relative interaction. The final Lagrangian is:

$$L = -\frac{1}{4}W_{\mu\nu}W^{\mu\nu} - \frac{1}{4}B_{\mu\nu}B^{\mu\nu} \tag{3.19}$$

$$+\bar{L}\gamma^{\mu}\left(i\delta_{\mu} - g\frac{1}{2}\tau W_{\mu} - g^{'}\frac{Y}{2}B_{\mu}\right)L \tag{3.20}$$

$$+\bar{R}\gamma^{\mu}\left(i\delta_{\mu} - g^{'}\frac{Y}{2}B_{\mu}\right)R \tag{3.21}$$

$$+|\left(i\delta_{\mu} - g\frac{1}{2}\tau W_{\mu} - g^{'}\frac{Y}{2}B_{\mu}\right)\phi|^2 - V(\phi) \tag{3.22}$$

$$-\left(G_1\bar{L}\phi R + G_2\bar{L}\phi_C R + Hermitian\,conjugate\right). \tag{3.23}$$

where L denoted a left-handed fermion (leptons or quark) doublet and R a right-handed fermion singlet. The first row describes vector bosons ($W^{\pm}$, Z, γ) kinetic energies and self-interactions, the second and third rows lepton and quark kinetic energies and their interactions with $W^{\pm}$, Z, γ. The fourth row describes the $W^{\pm}$, Z, γ and Higgs boson masses and couplings while the last row the lepton and quark masses and coupling to the Higgs boson.

3.2 The SM Higgs boson production and decay channels

The SM Higgs boson production cross section at colliders depend on the type of accelerated particles, on the energy of the beams and, finally, on the physical Higgs boson mass value. In proton-proton collisions, there are four main mechanisms involved:

- Gluon-gluon fusion (ggH or GF) : the gluon coupling to the Higgs boson in the SM is mediated by loops of quarks. The main contribution comes from the top quark since it is the higher mass fermions. The GF is the dominant production process at hadron colliders, given the high partonic luminosity of the gluons. The state of the art predictions include NNLO+NNLL order QCD corrections and NLO corrections from electroweak and mixed QCD electroweak terms, whose size is nonetheless small. The theoretical uncertainty on the predicted cross section from neglected higher order terms is about 8% [74].
- Vector-boson fusion (VBF) : the Higgs boson is produced through its couplings to vector bosons W and Z which are emitted by the interacting quarks in the protons interaction. Due to the mass of the mediators, a sizable fraction of the transverse momentum is transmitted to the hadronic fragments of the proton, originating a pair of energetic jets with a small angle with respect to the beam axis. This results in final states with two jets at high rapidities. The VBF cross section is about one order of magnitude lower than the GF, at least for Higgs masses up to 1 TeV.
- Associated production with vector bosons (VH) : the Higgs boson is emitted via a Higgs-strahlung from a W or Z boson produced by $q\bar{q}$ interaction. It has a production cross section smaller than VBF and the main contributions come from WWH and ZZH vertices.
- Associated production with top or bottom quarks (ttH/bbH) : it is the process with the smaller cross section. The $t\bar{t}$ H production process provides distinctive signatures such as a large amount of hadronic activity in the collision or

possibly one or more leptons from semileptonic top decays. This channel allows for a direct measurement of the Yukawa coupling between top quark and Higgs boson.

	σ[pb] 8 TeV	σ[pb] 13 TeV	σ/σ_{tot} % 13 TeV
ggH	19.24	43.92	86.2
VBF	1.579	3.748	7.4
WH	0.7028	1.380	2.7
ZH	0.4143	0.8696	1.7
$t\bar{t}$ H	0.1290	0.5085	1.0
$b\bar{b}$ H	0.2030	0.5116	1.0

Table 3.2: Higgs boson production cross section for each mode, for p-p collision at $\sqrt{s}$ = 8 TeV and $\sqrt{s}$ = 13 TeV, assuming m_H = 125.09 GeV; all cross sections are computed at NNLO+NNLL QCD and NLO EW [75].

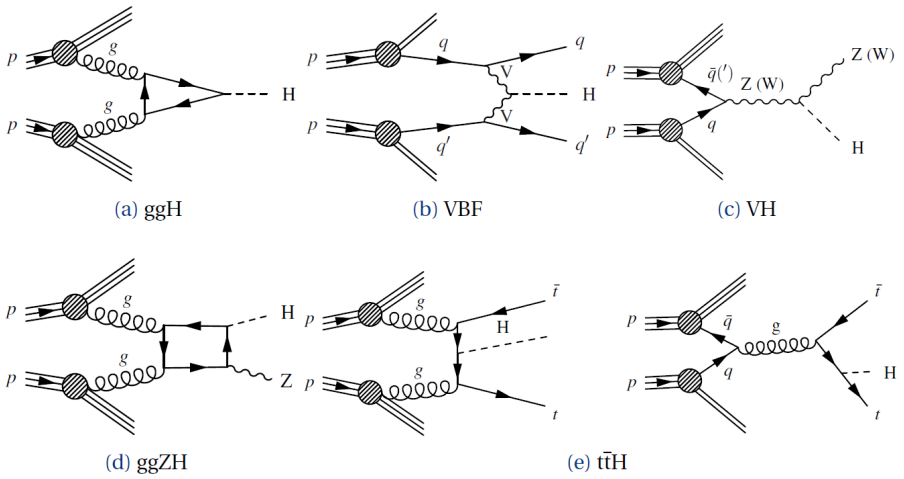

Figure 3.2: LO Feynman diagrams for different Higgs production modes with gluons and quarks in the initial state.

The Leading Order (LO) Feynman diagrams related to these processes are reported in Fig. 3.2 while the predicted values of Higgs boson cross section in p-p collisions at $\sqrt{s}$ = 13 TeV, with a m_H = 125.09 GeV[2], are reported in Tab. 3.2. An increment of a factor 2.3 from the $\sqrt{s}$ = 8 TeV is expected for the ggH mechanism. In Fig. 3.3, the different contributions of these four production mechanism are reported for p-p collisions at $\sqrt{s}$ = 8 TeV as a function of Higgs mass. The comparison of the total Higgs boson production cross section at different centre of mass energies is also reported in Fig. 3.3 as a function of the Higgs mass.

3.2.0.0.1 The Higgs boson decay channels The SM Higgs boson can be detected only through its decay products. The various decay channels present a different decay rate depending on the coupling to the Higgs boson. The Higgs boson Branching Ratios (BR) are defined as:

$$BR(H \to a) \equiv \frac{\Gamma(H \to a)}{\Gamma_H}, \tag{3.24}$$

[2]Latest value of the Higgs boson mass, as it has been measured by LHC experiments [76].

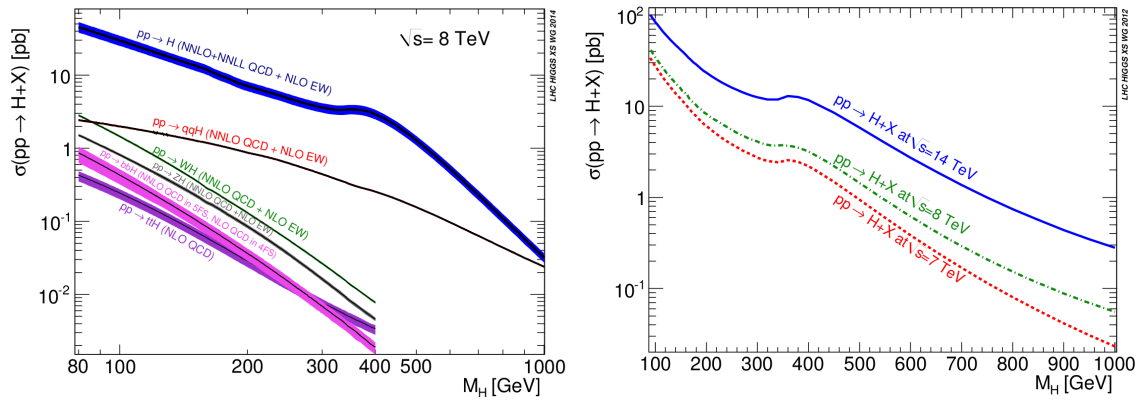

Figure 3.3: Cross section of the main SM Higgs boson production mechanisms for p-p collisions at $\sqrt{s}$ = 8 TeV as a function of Higgs mass (left); comparison of the total Higgs boson production cross section at different centre of mass energies (right) [75].

where $\Gamma(H \to a)$ is the inverse decay rate of the final state a and Γ_H is the sum over all the decay channels kinematically allowed by the SM. The Γ_H depends on the mass of the Higgs boson, considering m_H = 125 GeV it is predicted to be equal to 4.07 MeV [74]. The Higgs boson decay channels are shown in Fig. 3.4 as a function of the Higgs boson mass. At LO in the SM couplings, the Higgs boson can decay into pairs of fermions, mainly $b\bar{b}$ and $c\bar{c}$, through Yukawa interactions and into pairs of W or Z bosons through weak interactions. A gluon or photon pair can be produced by a W loop and a fermion loop, which is dominated by the top quark contribution. Decays into gluons are mediated by quark loops, being the mirror process of the gluon fusion production. Finally, the decay into a pair of leptons is allowed and $\tau\tau$ is dominating over the $\mu\mu$ channel. The Higgs boson decay branching fractions for these final states for m_H = 125.09 GeV are reported in Tab. 3.3.

	$b\bar{b}$	WW	gg	$\tau\tau$	$c\bar{c}$	ZZ	$\gamma\gamma$	$Z\gamma$	$\mu\mu$
BR (%)	57.5	21.6	8.56	6.3	2.9	2.7	0.23	0.15	0.02

Table 3.3: The Higgs boson decay Branching Ratios for m_H = 125.09 GeV [74].

3.3 The SM Higgs boson discovery in LHC Run 1

The LHC Run 1 corresponds to a great period for the high energy physics community. As described in Sec. 1.1.1, the first breakthrough has been the achievement of particle collisions at the highest centre of mass energy reached so far: $\sqrt{s}$ = 7 TeV in 2011 and sequentially $\sqrt{s}$ = 8 TeV from the 2012 with a great amount of collected data. This allowed to obtain one of the most important target of the LHC physics program: the discovery of the Higgs boson and the following measurement of its properties.

On July 4th 2012, the discovery of a new particle has been simultaneously announced by the CMS and ATLAS experiment collaborations. A new boson with a mass close to 125 GeV had been observed with a statistical significance of 5σ, after collecting approximately 5 fb^{-1} data at $\sqrt{s}$ = 7 TeV and 5 fb^{-1} at $\sqrt{s}$ = 8 TeV [1, 2]. The excess was observed in data in several different channels sensitive to the decay of a scalar boson. These can be divided into the high-resolution channels ($4l$, $\gamma\gamma$), which provide a clear signature without the presence of hadronization processes, and the low-resolution channels ($2l2\nu$,

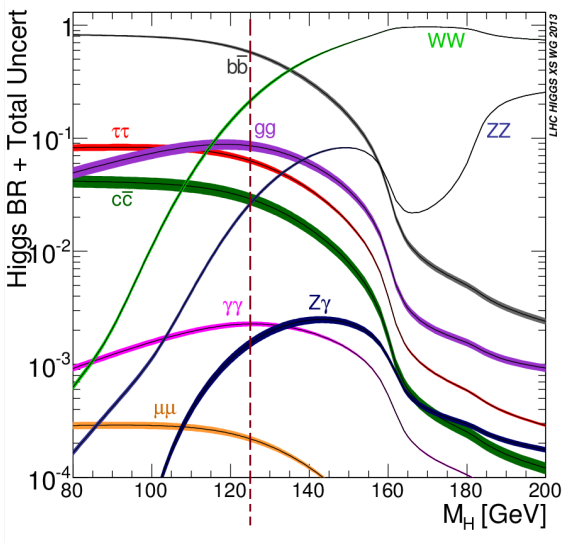

Figure 3.4: Standard model Higgs boson branching ratios for all the possible decay channels as a functions of its mass; total uncertainty is also reported [75].

$\tau\tau$, $b\bar{b}$) with the presence of missing energy or jets that worsen the reconstructed mass resolution. The $4l$ channel includes $4e$, 4μ, $2e2\mu$ and it is sensitive to the $H \to ZZ^{(*)}$ decay while the $2\nu 2l$ looks at both $H \to WW^*$ and $H \to Z^{(*)}$.

The properties of the new boson have then been studied looking at further data collected in 2012, showing that the observed particle was compatible with the expected SM Higgs boson. The measured properties are reported in Tab. 3.4, where it can be seen the good agreement between ATLAS and CMS results. Both CMS and ATLAS experiments performed the searches on the full set of data collected during the Run 1 (~ 20 fb^{-1}).
The Higgs boson properties have been studied mainly in the high-resolution channels. The mass of the new boson has been measured with a good precision by using $H \to \gamma\gamma$ and $H \to ZZ^{(*)} \to 4l$, characterized by a 1-2 GeV mass resolution, as shown in Fig. 3.5 and reported in Tab. 3.4. The Higgs boson mass measurements from ATLAS and CMS have been recently combined [76], providing this state-of-the-art value:

$$m_H = 125.09 \pm 0.21(stat) \pm 0.11(syst)\ GeV.$$

The spin-parity properties have been studied exploiting these two channels plus the $H \to WW^{(*)} \to 2l2\nu$ final state. The observed data showed the boson to be consistent with the pure scalar hypothesis, $J^P = 0^+$ as predicted by the SM, while disfavoring the vector and pure pseudoscalar hypothesis. As for the total width, since a direct measurement at the resonance peak is limited by experimental resolution (few GeV upper limit with respect to 4.07 MeV predicted from SM for m_H = 125 GeV), constraints on the order few tens of MeV are derived by exploiting the on-shell and off-shell production and decay rates to a pair of Z bosons.
The consistency of the observed state with the expectations for a SM Higgs boson (μ) has been measured exploiting different channels, as reported in Tab. 3.4. Searches for deviations of the Higgs boson scalar couplings magnitudes from those predicted for the SM have been performed, reporting no statistically significant deviations.

The evidence of a scalar boson and its compatibility with the SM Higgs boson have thus been demonstrated with the data collected in the LHC Run 1 at $\sqrt{s}$ = 7-8 TeV. All

Experiment	Property	Channel
	m_H	$ZZ^{(*)} \to 4l, \gamma\gamma$
ATLAS	125.36± 0.37(stat.)±0.18(syst.) GeV	
CMS	$125.03^{+0.26}_{-0.27}$(stat.)$^{+0.13}_{-0.15}$(syst.) GeV	
	Γ_H/Γ_H^{SM}	$ZZ^{(*)} \to 4l, ZZ^{(*)} \to 2l2\nu$
ATLAS	< 5.7 (8.5) at 95% C.L.	
CMS	< 5.4 (8.0) at 95% C.L.	
	$J^P = 0^+(0^-, 1^\pm, 2^\pm)$	$\gamma\gamma, ZZ^{(*)} \to 4l, WW^* \to l\nu l\nu$
ATLAS	97.8% C.L.	
CMS	99.9% C.L.	
	μ	$\gamma\gamma, ZZ^{(*)} \to 4l, WW^* \to l\nu l\nu, b\bar{b}, \tau\tau$
ATLAS	1.30±0.12(stat.)±0.10(theo.)±0.09(syst.)	
CMS	1.00±0.09(stat.)$^{+0.08}_{-0.07}$(theo.)±0.07(syst.)	

Table 3.4: Properties of the Higgs boson measured by ATLAS and CMS experiments with data collected during LHC Run 1. The signal strength, μ, is defined as the measured cross section relative to the standard model expectation.

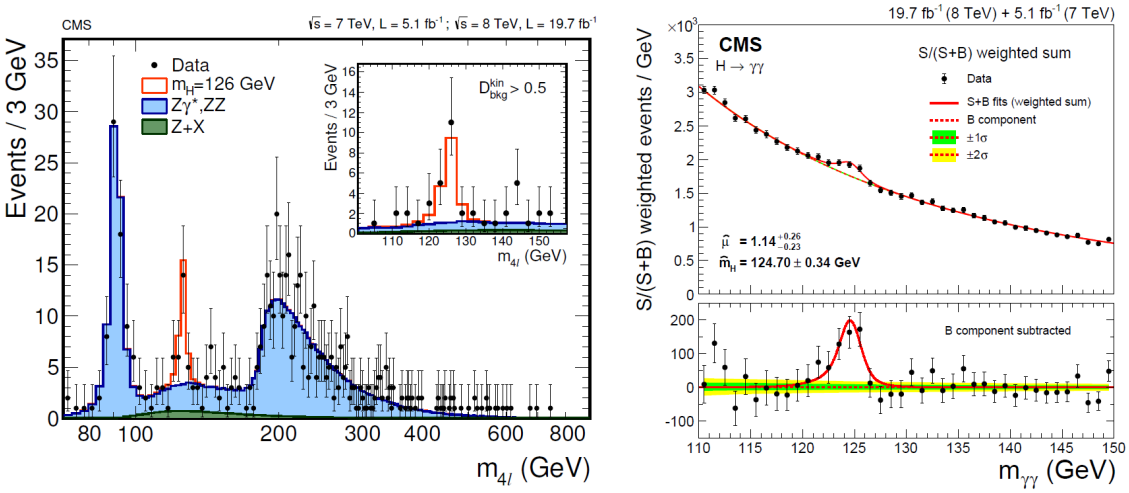

Figure 3.5: Four-lepton reconstructed mass in full mass range for the sum of the $4e$, 4μ, and $2e2\mu$ channels (left) [77]; $\gamma\gamma$ invariant mass distribution (right) [78]. A resonant peak in the 125 GeV region is evident in both distributions.

these searches will be re-done in the LHC Run 2 on data from $\sqrt{s}$ 13 TeV collisions. The data delivered by LHC in the 2015 (about 4 fb^{-1}) are not enough to reply and improve the previous measurements and the Higgs boson discovery has not yet been re-confirmed with the 13 TeV data. These are expected to come within the end of the 2016 thanks to the planned integrated luminosity of 40 fb^{-1}.

3.4 Higgs bosons pair production

The LHC Run 1 provided the discovery of the Higgs boson and its characterization. This has been an important confirmation of the validity of the SM. In the Run 2, apart from the Higgs 're-discovery', the greatest physics topics are related to the searches for unseen models and additional states coming from new physics phenomena beyond the SM. Some of these searches can be performed using the Higgs as a tool for discovery and a precise knowledge of the strength of the Higgs boson interactions with SM fields is one

of the desiderata to get more information on its origin and to re-fine the exclusion limits on the BSM scenarios.

The knowledge of the strength of the Higgs boson interactions with SM fields passes by the correct reconstruction of the Higgs potential. This includes also the measurement of the trilinear and quartic Higgs self-couplings, defined in Eq. 3.15, which are only accessible in multi-Higgs production processes at the LHC. The non-resonant production of a Higgs bosons pair (*di-Higgs*) represents the golden channel to study details of the SM Higgs potential at hadron colliders. The main production channel for SM Higgs bosons pair in p-p collision is the gluon-fusion and its predicted cross section at the centre of mass energy of 13 TeV is about 34 fb. This value is extremely low compared to the expected irreducible background, and the detection of the SM Higgs pair production at LHC is expected to be accessible only after the upgrades planned at end of the current Run 2 (HL-LHC). However, enhancement on the di-Higgs production is considered in many new physics scenarios. Tree-level couplings of the Higgs boson to fermions and gauge bosons are expected to be modified with respect to the SM prediction and to produce an enhancement of the non-resonant di-Higgs cross section production, *e.g.*, the Higgs trilinear coupling (λ) variations. The di-Higgs cross section variation as a function of the λ/λ^{SM} is shown in Fig. 3.6.

New heavy particles decaying into the pair of Higgs bosons are also predicted in BSM scenarios and they will appear as resonant state in the di-Higgs mass spectrum. Sizable modifications of the couplings can also arise in weakly-coupled extensions of the SM, such as supersymmetry, through the mixing of the Higgs boson with new states [79]. In this case one expects to produce these new particles directly at the collider. Extra dimensions theories also predict existence of a massive scalar or a spin-two particle produced by gluon fusion which could decay into a pair of Higgs bosons [80].

The search for di-Higgs production can thus be divided into two main branches: resonant and non-resonant di-Higgs production, where the latter includes also the SM processes.

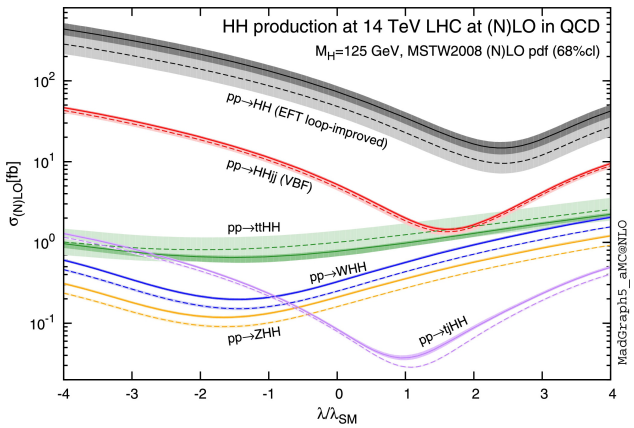

Figure 3.6: Non-resonant Higgs bosons pair production cross section for p-p collision at $\sqrt{s} = 14$ TeV for different values of the Higgs boson trilinear coupling (λ); the ratio with respect to the SM value is considered [81].

3.4.1 Anomalous couplings in the non-resonant di-Higgs production

The non-resonant Higgs bosons pair defines all the process that produces a pair of Higgs bosons without the presence of an intermediate state (resonance) in the produc-

tion chain. The Higgs boson self-interaction is allowed in the SM and thus also the production of two Higgs bosons from the same vertex. The process is strongly suppressed due to the expected value of the Higgs boson trilinear coupling. In the SM, Higgs pair production occurs predominantly by gluon fusion via an internal fermion loop, where the top quark is dominant. This assumption can be extended to BSM theories bringing to three main variations in the Higgs pair production: the presence of a BSM particle that acts in the internal fermion loop; the possibility of a direct contact interaction between Higgs and top quark; the possibility of a direct contact interaction between Higgs and gluons. This extension to BSM theories is well motivated if the Higgs sector is minimal, as it is described in [82]. The resulting processes that contribute to a di-Higgs signal in pp collisions at LO are schematised in Fig. 3.7.

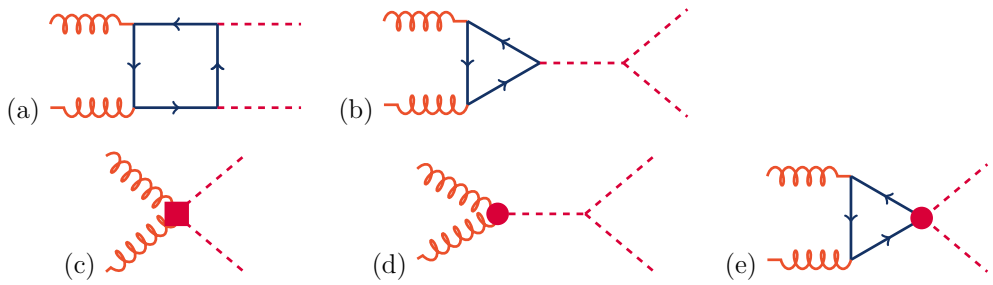

Figure 3.7: Feynman diagrams of processes that contribute to Higgs pair production by gluon-gluon fusion at LO. Diagrams (a) and (b) correspond to SM-like processes, while diagrams (c), (d), and (e) corresponds to pure BSM effects: (c) describes contact interactions between the Higgs boson and gluons, and (e) exploits the contact interaction of two Higgs bosons with top quarks.

In the absence of new light states, the gluon fusion Higgs pair production at the LHC can be generally parametrized (to leading approximation) with five parameters controlling its tree-level interactions. These five parameters are: κ_λ and κ_t, related to couplings allowed by the SM; c_g, c_{2g}, and c_2, describing BSM effects. In particular, κ_λ and κ_t are multiplicative factors that parametrize, respectively, deviations of the Higgs boson trilinear coupling (λ) and the top Yukawa interaction (y_T) from their SM values. The contact interactions of the Higgs boson with gluons and between two Higgs bosons and two gluons or top quarks are instead not predicted by the SM; they could arise through the mediation of very heavy new states and are parametrized by the absolute couplings c_g, c_{2g}, and c_2.

The relative Lagrangian can thus be written in terms of physical states, as:

$$\mathcal{L}_h = \frac{1}{2}\partial_\mu h \partial^\mu h - \frac{1}{2}m_h^2 h^2 - \kappa_\lambda \lambda_{SM} v h^3 - \frac{m_t}{v}(v + \kappa_t h + \frac{c_2}{v} h h)(\bar{t_L} t_R + h.c.) + \frac{1}{4}\frac{\alpha_s}{3\pi v}(c_g h - \frac{c_{2g}}{2v} h h) G^{\mu\nu} G_{\mu\nu} . \quad (3.25)$$

One should note that, in the case of a linear realization of electroweak symmetry breaking, it results that $c_{2g} = -c_g$ within the effective field theory (EFT) framework considered here. This describes the effects of new heavy states beyond the collider resolution via op-

erators of dimension $4 < D \leq 6$ [83, 84, 85, 86] [3]. In equation 3.25 the Higgs boson couplings to light fermions are assumed to be negligible, CP-violating BSM effects are ignored and the absence of any other light state in addition to the SM particles is excluded. In the presence of such states, the correlation between the kinematic structures induced by c_g and c_{2g} could be modified [87]. In particular, in models with an extended (non-decoupling) Higgs sector, the coupling of the Higgs boson to bottom quarks might also be enhanced in the limit of large scalar mixing. Other effects could arise in SUSY-like theories, where heavy SUSY scalars are predicted (see for example [88, 89, 90]). Nevertheless, this framework can be used if the decoupling limit leads only to heavy new states.

Since any dimension-6 EFT basis is related to the Higgs basis by analytical relations among the coefficients, the translation of this parametrization to the flavour-diagonal Higgs basis (see [91, 92]) is trivial; the automation of basis conversions is under development [93].

The kinematics of the di-Higgs process is strongly dependent on the values of these five parameters, i.e, different choices of the coupling parameters give rise to striking differences in the density functions of the kinematic observables. It has been computed that, changes in the top Yukawa parameter at LO as small as 30% and/or in Higgs trilinear coupling of $\mathcal{O}(1)$ times the SM drive modifications of the p_T^h distribution from single-peaked structures to more complex two-peaked shapes separated by $\mathcal{O}(50)$ GeV. The distribution of the di-Higgs mass for generator-level samples related to five points of the parameters space are shown in Fig. 3.8. The SM sample is peaked around 400 GeV while the maximal interference between triangle and box diagrams (Fig. 3.7) leads to a typical double peak distribution. The low mass (<250 GeV) peak comes from process associated to the triangle diagram contribution only.

The main variation in the the process kinematic are expected to be in the parameters space regions around the cross section minima.

3.4.1.1 Non-resonant di-Higgs production cross section

The contributions of the different production modes to the non-resonant Higgs bosons pair production in proton-proton collisions reflect the one for the single Higgs boson production described in Sec.3.2. The main contribution occur from the gluon-fusion and the SM cross section at $\sqrt{s}$ = 13 TeV is expected to be $\sigma_{hh}^{SM} = 34.3$ fb $\pm 9\%$ (scale) $\pm$ 2%(PDF), while at 8 TeV it is $\sigma_{hh}^{SM} = 9.96$ fb $\pm 10\%$ (scale) $\pm 2\%$ (PDF). The cross section for VBF production at $\sqrt{s}$ = 13 TeV is instead 6.8 fb while only 0.7 fb has been computed for ttH process. Those values are based on recent progress [94, 95], which use the `CT10` PDF set [96] and employ as input the mass values $m_h = 126$ GeV, $m_t = 173.18$ GeV, and $m_b = 4.75$ GeV. Regarding the dimension-six parametrization, relevant calculations are described in [97]. At LO the scattering amplitude for the $gg \to hh$ process contains terms with different loop structures, corresponding to the different BSM operators. Different groups of phenomenologists are progressing in the calculation of (N)NLO predictions matched to shower-level effects for the GF di-Higgs process, especially for the SM case; see for example [98, 99, 100, 101].

As for the 5-D parameter space, the cross section has been computed in the limit of the present computational capability as described in [102]. The full cross section of GF Higgs

[3] This normalization for the Higgs boson interaction with gluons is inspired by the SM limit of contact interactions in the limit of infinitely heavy top quark mass. The existence of a relative sign between c_{2g} and c_g in this limit is a special feature of the SM, related to the SM fermions chiral nature.

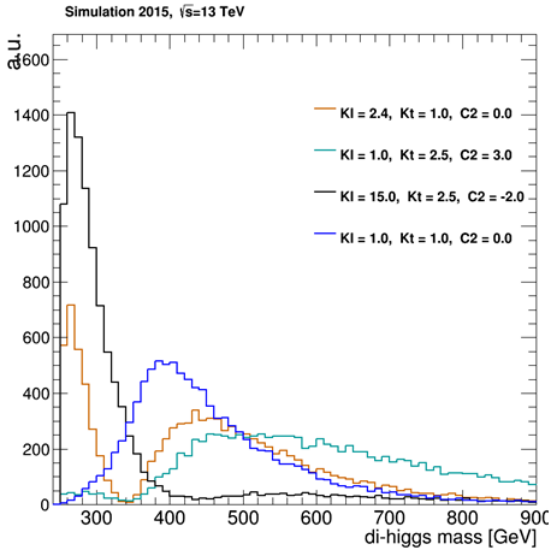

Figure 3.8: Di-Higgs mass spectrum for four different point of the parameters space ($c_g = c_{2g} = 0$) representing particular interferences between the Feynman diagrams related to Higgs bosons pair production: Standard Model like (blue); maximal interference between triangle and box diagrams, with a typical double peak distribution (brown); main contribution from triangle diagram, low mass peak (black); main contribution from box diagram, high mass bump (light blue).

pair production can be expressed by a polynomial in terms of all the model parameters as in equation 3.26 below:

$$\frac{\sigma_{hh}}{\sigma_{hh}^{SM}} = \begin{pmatrix} A_1\,\kappa_t^4 + A_2\,c_2^2 + (A_3\,\kappa_t^2 + A_4\,c_g^2)\,\kappa_\lambda^2 + A_5\,c_{2g}^2 + (A_6\,c_2 + A_7\,\kappa_t\kappa_\lambda)\kappa_t^2 \\ +(A_8\,\kappa_t\kappa_\lambda + A_9\,c_g\kappa_\lambda)c_2 + A_{10}\,c_2c_{2g} + (A_{11}\,c_g\kappa_\lambda + A_{12}\,c_{2g})\,\kappa_t^2 \\ +(A_{13}\,\kappa_\lambda c_g + A_{14}\,c_{2g})\,\kappa_t\kappa_\lambda + A_{15}\,c_g c_{2g}\kappa_\lambda \end{pmatrix} \tag{3.26}$$

The resulting cross section in some 2-D planes of the parameters space are shown in Fig. 3.9.

This Lagrangian parametrization, shown in Eq. 3.25, has been used in both the cluster analysis and the non-resonant di-Higgs searches that are object of this thesis.

3.4.2 Higgs bosons pair, searches at LHC

The Higgs bosons pair searches have been performed in the LHC Run 1 and they have been included in the current search programs of both ATLAS and CMS experiments. The resonant di-Higgs production has been mainly studied in the LHC Run 1, due to the higher feasibility of that search. The high mass (> 1.5 TeV) and low mass di-Higgs resonant searches are also on-going on the first data collected during 2015. Preliminary searches have been performed on the non-resonant di-Higgs production but this scenario will be extensively investigated within the end of the LHC Run 2 only.

The $H \to b\bar{b}$ is the Higgs decay channel with the highest branching fraction (Fig.3.10). Thus, since the production cross section of the Higgs bosons pair is low, one Higgs boson of the pair is always reconstructed looking at this decay channel by both ATLAS and CMS experiments. The decay into a b, γ, τ or W pair is considered for the second Higgs boson. The search in the four b-quark final state has a consistently higher branching ratio but it suffers from the high irreducible background coming mainly from QCD processes. The

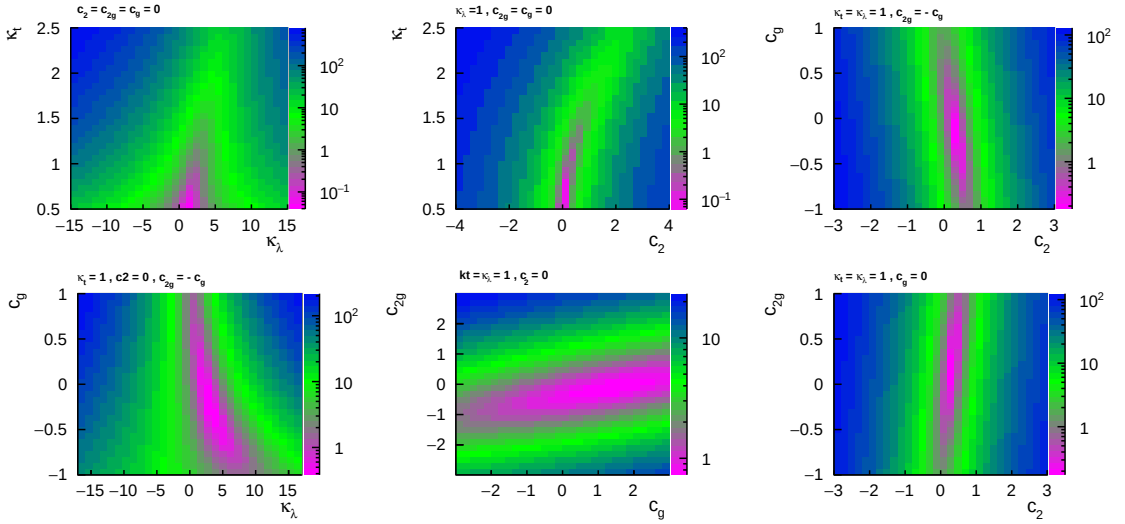

Figure 3.9: Cross section ratios (σ_{BSM}/σ_{SM}) in selected slices of the parameter space. Left column: the plane of SM parameters, k_t: k_λ, as well as allowing a Higgs contact interaction with gluons, c_g: k_λ. Middle column: comparing one- and two-Higgs interactions with top quarks and with gluons, respectively, k_t: c_2 and c_{2g}: c_g. Right column: comparison between gluon and top-quark interactions, c_g: c_2 and c_{2g}: c_2, always for selected values of the other parameters, where the relation c_{2g} = -c_g is broken in the last plot.

final state in $b\bar{b}\,\gamma\gamma$, despite the low BR($H \rightarrow b\bar{b}\gamma\gamma$ = ~0.3%), is quite promising thanks to the excellent invariant mass resolution for the $\gamma\gamma$, a very low QCD background and the large efficiency to reconstruct both b-quarks and photons (60% and >90% respectively).

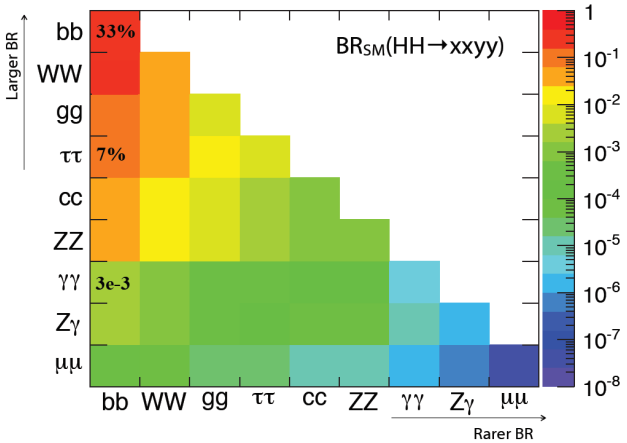

Figure 3.10: Possible final state combination in the di-Higgs production and relative branching ratio.

3.4.2.1 Resonant Higgs bosons pair searches at LHC

The resonant Higgs bosons pair defines the presence of Higgs boson pairs that are produced exclusively from the decay of an higher mass state: $X \rightarrow HH$. This leads to a narrow-width resonance in the four bodies (two Higgs decay products) mass spectrum in correspondence to the X state mass value. This process implies the presence of one or more new states and their consequent mixing to the Higgs boson with sizable modifications of the couplings. The resonant Higgs pair production is thus not compatible

with SM and it derives from several BSM models. On one hand, radion or Kaluza-Klein gravitons are expected in the Randall-Sundrum (RS1) model of warped extra dimensions [80]. On the other hand, the 2 Higgs-Doublet Models introduce five Higgs bosons and the possibility of a higher mass composite Higgs boson.

These resonance states can be produced with a cross section higher than the SM process and they could in principle be probed already with the data collected on LHC Run 1 or Run 2 data taking. In Fig. 3.11, the full set of results from the LHC Run 1 data analyses by both CMS and ATLAS is shown. The resonance mass spectrum has been covered from 250 GeV to 3000 GeV and no excess has been measured. The irreducible background decreases in function of the four bodies mass and thus also the upper limit are more tight in the very high mass region.

Both ATLAS and CMS experiments searched for resonant di-Higgs looking at the $b\bar{b}\gamma\gamma$ [103, 104] and $b\bar{b}\ b\bar{b}$ channels [105, 106]. The $b\bar{b}\tau\tau$ channel has also been exploited by the CMS collaboration and the results are under publication. Generally speaking, the search in $b\bar{b}\gamma\gamma$ channel can be more sensitive to structures in the low mass region (up to 250-300 GeV) of the four bodies mass and it is instead limited by the low branching fraction above the 400 GeV. The $b\bar{b}\ b\bar{b}$ can instead progressively discard the QCD background in the higher mass region and thus it can be more sensitive thanks to the higher branching fraction. The resonant mass distribution reconstructed in this channel in the signal region between 400 and 900 GeV is shown in Fig. 3.12. Several factors have to be added to these principle limitations and the final upper limit depends also on the analysis methods, thus, large mass spectrum is investigated in both decay channels. These searches will be performed also on the LHC Run 2 data and further decay channels will be considered, such as $b\bar{b}WW$.

A particular scenario appears in the high mass region (> 1.2 TeV) because the products of the Higgs decay show a different physical structure. The golden channel for this region is the fully hadronic one, in particular $b\bar{b}\ b\bar{b}$, where the two jets produced by each Higgs decay are spatially very close. This is the, so-called, boosted regime and the two jets can hardly be identified as two separated objects by the standard techniques. Additional algorithms have been implement to improve the jet identification in the boosted regime and new searches are on-going on the data collected in the 2015. The great advantage of this region is the almost null expected background, thus the possibility to get a discovery/set tight upper limit with relatively low statistics.

3.4.2.2 Non-resonant Higgs bosons pair searches at LHC

Looking at data collected during the LHC Run 1, the CMS collaboration searched for the non-resonant production in the $b\bar{b}\gamma\gamma$ channel, while ATLAS looked at both $b\bar{b}\gamma\gamma$ and $b\bar{b}b\bar{b}$ channels [107]. An observed 95% confidence level upper limit on the production cross section of the process has been set to a value $\sigma(pp \to hh \to b\bar{b}b\bar{b})/\sigma_{SM} \sim 56\%$ by ATLAS and $\sigma(pp \to hh \to b\bar{b}\gamma\gamma)/\sigma_{SM} \sim 74\%$ by CMS. CMS results are currently in review phase.

The CMS collaboration has considered also the BSM scenarios using the parametrization described in Sec. 3.4.1. As mentioned before, there are substantial cross section variations as a function of Higgs boson anomalous couplings and the sensitivity to some regions of the 5-dimensional parameters space is much higher with respect to the SM process. The results of this search on $\sqrt{s} = 8$ TeV data are shown in Fig. 3.13 and 3.14. The 95% confidence level upper limit have been set on 124 points of the three-dimensional parameters space ($c_{2g} = c_g = 0$). The excluded points in the theory parameters space are

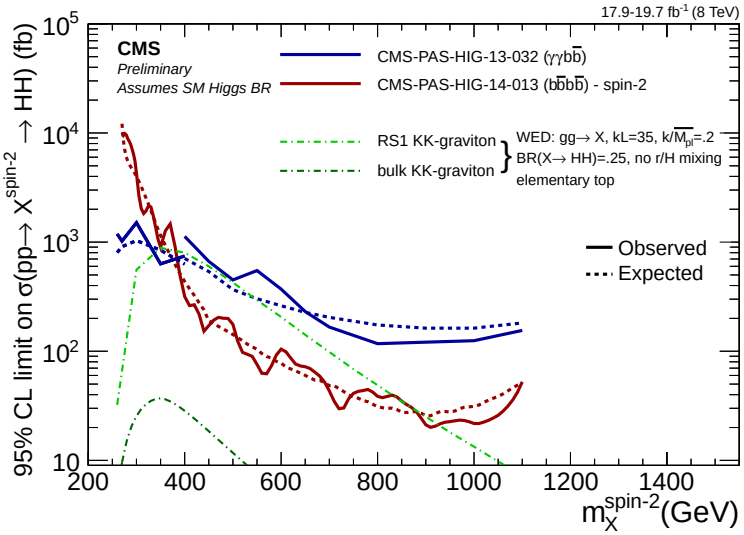

Figure 3.11: Resonant di-Higgs production cross section upper limit set by CMS collaboration in the LHC Run 1 data analyses; upper limits are reported as a function of the resonant mass and for different decay channels searches [104].

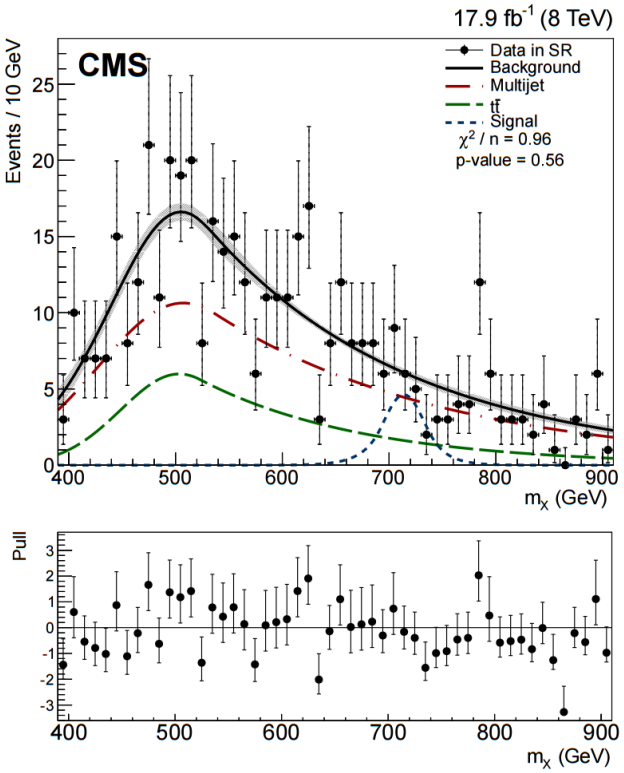

Figure 3.12: The resonant mass distribution in data in the signal region between 400 and 900 GeV as reconstructed by CMS with the whole LHC Run 1 dataset. The fit is to the background-only hypothesis and the relative contributions of the QCD multijet (dashed-dotted red) and tt (dashed green) processes are shown [106].

the ones with cross section markers surrounded by small black boxes. All k_λ values are excluded below -17.5 and above 23. Other combinations of c_2, k_λ, or k_t parameters have been excluded. Since the signal efficiency can change significantly with interference pattern, a linear interpolation between the limits obtained for simulated signal samples may bias the result. Thus, only the discrete limit values have been given as final results.

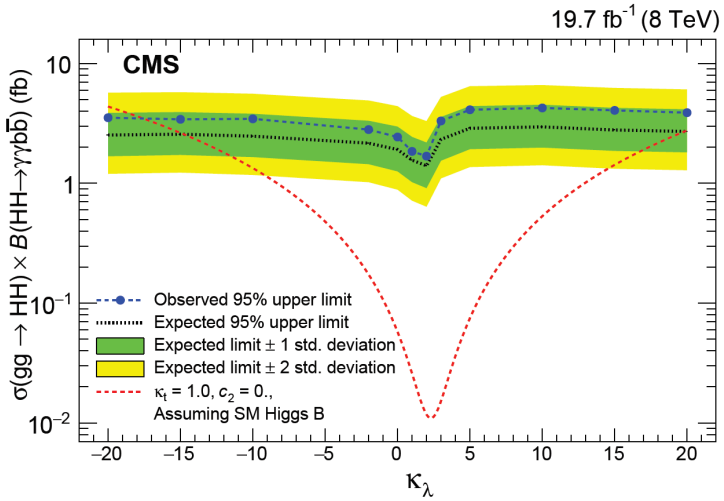

Figure 3.13: Observed and expected 95% CL upper limits on the product of cross section and the branching fraction $\sigma(gg \to HH) \times B(HH \to b\bar{b}\gamma\gamma)$ for the BSM-like analyses, performed by CMS on the LHC Run 1 data; only the Higgs trilinear coupling (k_λ) is varied; private communication.

As for the LHC Run 2, improvements in the upper limit for the SM are expected due to the 3.4 incremental factor of the process cross section. The BSM scenario is still the main topic of the non-resonant searches relaying on the assumption that any kind of coupling deviation from the SM Higgs sector is a proof that the SM is not complete. Therefore all possible Higgs boson couplings should be considered BSM and the parametrization used for the Run 1 data will be extended to a 5-dimension space, as described in Sec. 3.4.1.

As it has been seen with the Run 1 data, the sensitivity is higher in some regions of the parameters space and further exclusion limits can be set looking at $\sqrt{s}$ = 13 TeV data. For that to happen the observable features of the final state need to be exploited in an optimized way, given the huge cross section of irreducible backgrounds processes. This is hard to achieve if one takes the approach of parametrizing the signal cross section in bins of observable final state variables, once the efficiency of a baseline analysis selection is folded in, as one then loses the ability to exploit the signal characteristics and their multi-dimensional densities in an optimal way. To avoid this, a cluster analysis technique has been developed in 2015 in order to identify a manageable and small set of benchmark points which are maximally representative of the 5-dimension parameters space. This technique is described in the following chapter and its results will be used by the CMS collaboration in the present LHC Run data analyses.

All the accessible di-Higgs decay channels will be investigated by the CMS collaboration in the Run 2 also for the non-resonant searches. The same considerations on the features of the different channels made for the resonant searches can be applied also for the non-resonant ones. A preliminary searches for non-resonant $HH \to b\bar{b}b\bar{b}$ has been performed looking at data collected by CMS in 2015 at $\sqrt{s}$ = 13 TeV and it will be described in Chapter 5.

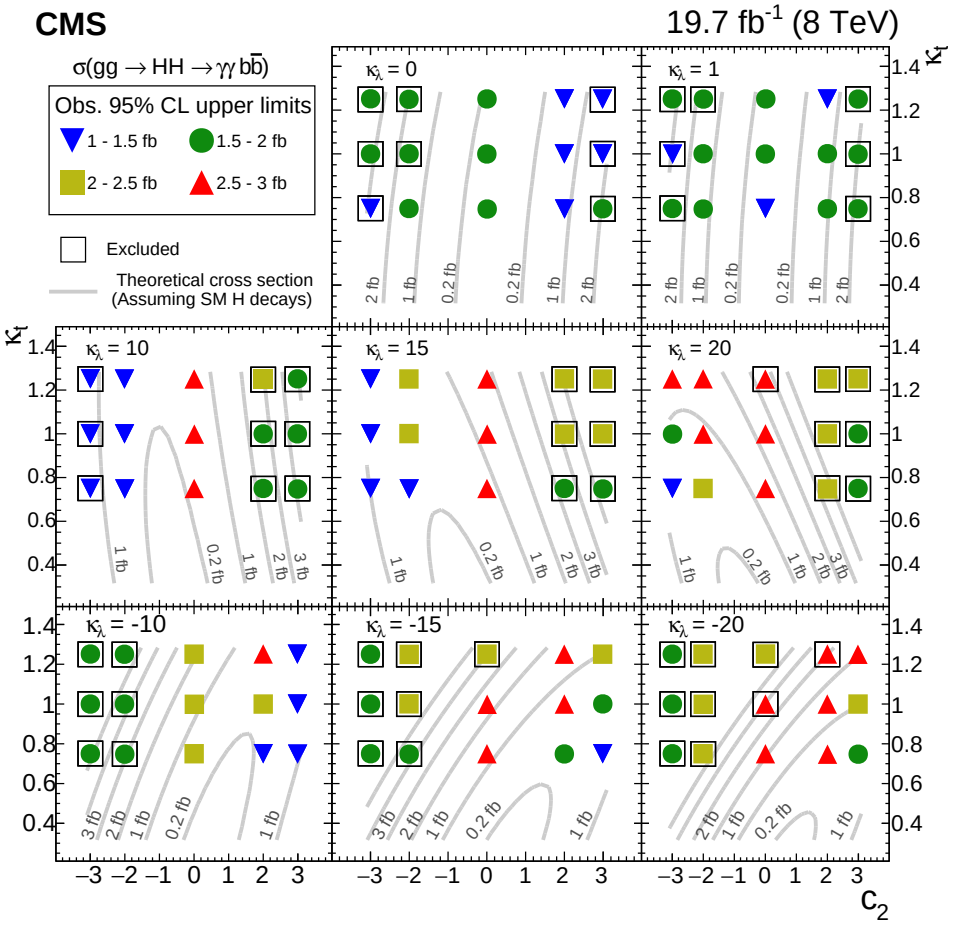

Figure 3.14: Observed limits for non-resonant two-Higgs production in BSM scenario described in Sec. 3.4.1; analysed points in the c_2 and k_t planes for different values of k_λ; the results are compared to the theoretical prediction. The gray lines represent contours of equal cross section. The boxed-in cross section markers give the combination of parameters excluded at 95% CL.; private communication.

Chapter 4

Cluster analysis for the selection of benchmark models

4.1 Motivations

A new physics model usually presents several degrees of freedom and the related parameters space to be investigated by experimental study is wide. A selection of significant parameters space points, namely benchmarks, is thus necessary. The collection of benchmarks should in principle offer an exhaustive representation of the varied final state composition and topologies that the new physics model may give rise to. The choice typically falls on those which are, or are expected to be, within the sensitivity reachable by the experimental search and their production cross section is considered as main criteria to identify the benchmarks. This guarantees a short-term impact but it does not allow a more general investigation of the parameters space.

The gluon fusion Higgs bosons pair production at the LHC offers a peculiar situation that fits perfectly with this scenario. As described in Sec. 3.4.1, the SM cross section of the Higgs bosons pair production at LHC is low to expect a measurement of the process from the data collected in the Run 2. The presence of Higgs boson anomalous couplings from Beyond Standard Model (BSM) scenarios leads to variations of the cross section of the process and of the kinematics of the final state. Furthermore, the anomalous couplings processes brings to homogeneous final states, there is no variation of the final state composition depending on the exact choice of theory parameters, as for other BSM scenarios.

This makes it an ideal ground for a more quantitative approach to the choice of benchmark points. The problem is thus taken from the side of shape information, rather than normalization, by partitioning the parameter space into homogeneous regions, identified as clusters. A custom technique, named *cluster analysis*, has been developed to perform this task and to provide a selected list of final benchmarks that simplifies the problem of investigating a large and unconstrained model space. Once the method is finalised, the selected benchmarks and the parameter space clusterisation will remain useful as the integrated luminosity collected by the LHC experiments grows from tens to hundreds of inverse femtobarns.

The description of this cluster analysis and its application to the searches for the non-resonant Higgs bosons pair production in BSM scenario is reported in this Chapter.

4.2 The method

The key idea of the cluster analysis is to identify sets of parameters which yield similar final state kinematics, to group them together in a cluster and to identify the final benchmarks. The cluster analysis method is composed by six main steps:

1. Definition of the parameter space and its allowed range.
2. Production of *generator-level* simulated samples that cover the parameters space.
3. Identification of the variables which completely describe the kinematic of the process.
4. Two-Sample test statistic identification and computation to define a metric of the kinematic similarity of the samples.
5. Perform an algorithm to group the samples in different clusters by looking at their relative distance represented by the two-sample test value.
6. Check the homogeneity of the kinematical distributions of the samples inside each clusters and define the optimal final number of clusters.

4.2.1 The parameter space definition

The case study for this cluster analysis has been the searches for non-resonant Higgs bosons pair production at LHC in BSM scenario. The parameter space is defined by the Lagrangian reported in Eq. 3.25. This leads to the previously mentioned five parameters: k_λ, k_t, c_2, c_g, $c_{2\mathrm{g}}$. The first two are related to SM processes and are defined as a ratio to the SM value. In particular, k_λ is linked to the Higgs boson trilinear coupling (λ) and it is defined as $k_\lambda = \lambda/\lambda^{SM}$, while k_t is an expression of the Yukawa coupling (y_t) [108] and it is defined as $k_\mathrm{t} = y_t/y_t^{SM}$. The other three parameters are referred to pure BSM processes: $t\bar{t}$ HH non-linear interaction and gluon contact interaction. The Feynman diagrams related to these processes are reported in Fig. 3.7.

The range of the five-dimensional parameters space can be defined by looking at upper limits set by previous data analysis. Measurements of single Higgs boson production performed so far at the LHC already constrain the κ_t and c_g parameters. The combination of those results using the κ formalism [109] shows that by marginalising over all other Higgs couplings the allowed values of κ_t are constrained at 95% C.L. in the region between 0.5 and 2.5. The ranges for the parameters have thus been chosen to be: $|k_\lambda| < 15$, $k_\mathrm{t} \in [0.5, 2.5]$ and $|c_2| < 5$. In addition, since the degeneracy between c_g and $c_{2\mathrm{g}}$ can only derive from a dimension 8 operator, they are expected to be small effects and the selected values are $\mathcal{O}(1)$ for both the parameters.

A samples grid is then defined to cover the resulting 5-dimensional space. Ideally one would like to start with a regular and homogeneous sampling of the parameter space. However, any meaningfully-spaced regular grid would require a prohibitive number of simulated data samples. The guideline to build the initial grid is thus to do a regularly coarse spaced grid and to increase the density of points in the regions of parameter space where the probability densities of the final state observables exhibit the fastest variability with parameter variation. These regions are identified with the local minima of the production cross section. The resulting population of the five-dimensional grid includes 1507 points of the 5-D parameter space. The detail of the grid composition is summarized in these three steps:

- a geometrically well-spaced grid in the planes reported in Fig. 3.9, identified by values of $k_\lambda = 0$, ±1, ±2.4, ±3.5, ±5, ±10, ±15; k_t from 0.5 to 2.5 in steps of 0.25 when $|k_\lambda| < 5$, and steps of 0.5 elsewhere; c_2 between -3.0 and 3.0 in steps of 0.5; c_g and c_{2g} between -1.0 and 1.0 in steps of 0.2.
- a strong cancellation between the different operators in the threshold m_{HH} region has been pointed out in some regions of parameter space (specially with $c_2 = 0.5$ and $c_{2g} = \mathcal{O}(1)$); this leads to topologies where a high m_{HH} tail is evident. In order to have a better kinematic description of this topology (and as well of the cancellation pattern between operators) one slice of parameter space with $c_2 = 0.5$ and $k_\lambda = k_t = 1$ is added to the grid, maintaining the previous binning in the c_2- c_{2g} plane.
- a purely three-dimensional grid of points in the hyperplane defined by $c_g = c_{2g} = 0$, which is described by the parameters k_λ, k_t, and c_2, is also considered. The points are identified by all possible combinations of the following parameter values: $k_\lambda = \pm1$, ±2.4, ±3.5, ±5, ±7.5, ±10, ±12.5, ±15; k_t from 0.5 to 2.5 in steps of 0.25; c_2 between -3.0 and 3.0 in steps of 0.5. An increased density of points is allocated near the point corresponding to the SM hypothesis ($c_2 < 1$).

Once the 5-D grid is defined, a simulation with 20,000 events of proton-proton collisions at 13 TeV centre of mass energy is generated per each point of the grid. The simulated samples are produced by using a setup developed by the authors of [110]. The Leading Order (LO) process is already at one-loop level; as for the approach followed in [110], loop factors are calculated on an event-by-event basis with a `Fortran` routine on top of an *aMC@NLO* [111, 112] effective model; the `NN23LO1` PDF set [113] is used. Those simulations represent the state-of-the art in the description of BSM di-Higgs production.

In order to retain generality of the results to any final state of gluon fusion di-Higgs production, and invariance to further analysis cuts and/or analysis techniques, the event topology is studied as it results from the production of the two Higgs bosons their decays and without a simulation of initial-state radiation. The simulated samples do not include any initial-state radiation effect and the process is thus a $2 \to 2$ process at LO.

The two Higgs bosons are produced at LO with identical transverse momenta, back-to-back in azimuth. The kinematic of the process can thus be defined by two variables in this study: the invariant mass of the di-Higgs system (m_{hh}) and the modulus of the cosine of the polar angle of one Higgs boson with respect to the beam axis ($|cos\theta^*|$). Since only parton level information are used, this last variable is equivalent to the polar angle in the Collins-Soper frame ($|cos\theta^*_{CS}|$) [114], which is commonly used in experimental analysis.

4.2.2 Two-sample test

In order to define a metric to classify physics models based on the similarity of the event kinematics they describe in the parameters space, a general statistical framework has to be chosen as well as a suitable two-sample test statistic. A two-sample test statistic (TS) can be the best candidate to estimate the degree of similarity among the samples. There exists a large variety of two-sample tests that could be used for this task, *e.g.* the Anderson-Darling test, the Kolmogorov-Smirnov test, the χ^2 test, the T test, or others. Those are usually single-dimensional tests because they are meant to compare two single-dimensional distributions; their extension to multi-dimensional data is not always straightforward, as it is subject to implementation choices that call for detailed power

studies. In a multi-dimensional setup possible choices also include the Energy Test [115] or unbinned nearest-neighbour-based metrics. Such multi-dimensional test statistic may be the right choice in situations when the statistics of the samples to be compared are very small, or when the dimensionality of the problem is large. However, in the specific case of non-resonant di-Higgs production a likelihood ratio based on Poisson counts in a set of 2-dimensional bins has been identified as the TS with the best trade off between computational requirements and power to detect localized differences in the kinematic distributions.

4.2.2.1 The Likelihood ratio Test Statistic

A binned likelihood ratio has been employed as test statistic for this application. The number of bins in m_{hh} and $|\cos\theta^*|$ are chosen such that the main kinematic features of the distribution are properly modelled while retaining sufficiently populated bins. The appropriate binning for this application has been found to be fifty 30-GeV-wide bins in m_{hh} in the range from zero to 1500 GeV and five 0.2-wide bins in $|\cos\theta^*|$ from zero to one.

The case in which the two samples under test share the same parent distribution is firstly considered to define the test statistic. The corresponding likelihood function is the product over the bins of the probability to observe $n_{i,1}$ and $n_{i,2}$ event counts in bin i from the two samples S_1 and S_2. This probability is given by the product of two Poisson distributions

$$Pois(n_{i,1}|\hat{\mu}_i) \times Pois(n_{i,2}|\hat{\mu}_i), \tag{4.1}$$

where $\hat{\mu}_i = (n_{i,1} + n_{i,2})/2$ is the maximum likelihood estimate for the expected contents in bin i. However it can be shown that

$$Pois(n_{i,1}) \times Pois(n_{i,2}) = Pois(n_{i,1} + n_{i,2}) \times Binomial(n_{i,1}/(n_{i,1} + n_{i,2})). \tag{4.2}$$

It is clear that the first term in the right-hand side of the decomposition does not contain any information about the contrast between the two samples shapes. The retained binomial term is explicitly

$$Binomial(n_{i,1}/(n_{i,1} + n_{i,2})) = \frac{(n_{i,1} + n_{i,2})!}{n_{i,1}!n_{i,2}!} \left(\frac{1}{2}\right)^{n_{i,1}} \left(\frac{1}{2}\right)^{n_{i,2}}. \tag{4.3}$$

To obtain a likelihood ratio, the case in which the two samples are equal is considered, a so-called *saturated hypothesis* [116]. The appropriate single bin content probability can be obtained from Eq. 4.3 by imposing $n_{i,1} = n_{i,2} = \hat{\mu}_i$, yielding

$$Binomial(n_{i,1} = n_{i,2} = \hat{\mu}_i) = \frac{(2\hat{\mu}_i)!}{(\hat{\mu}_i!)^2} \left(\frac{1}{2}\right)^{2\hat{\mu}_i}. \tag{4.4}$$

Calling L the likelihood obtained from the distribution in Eq. 4.3 and L_S the one from Eq. 4.4 we define the log-likelihood ratio test statistic (TS):

$$TS = -2\,log\left(\frac{L}{L_S}\right) = 2\sum_{i=1}^{N_{bins}} log(n_{i,1}!) + log(n_{i,2}!) - 2log\left(\frac{n_{i,1} + n_{i,2}}{2}!\right), \tag{4.5}$$

which, up to a minus sign, is χ^2 distributed as stated by Wilks' theorem [116, 117]. Thanks to this property this TS can be directly used as an ordering parameter to perform a cluster

analysis. The values TS_{ij} and TS_{kl} obtained respectively by testing the compatibility of samples ij and kl are suitable to determine *e.g.* if samples S_i and S_j are more similar to each other than are samples S_k and S_l, this is the case if $TS_{ij} > TS_{kl}$.

In addition, the above TS is particularly sensitive to small-scale features of the distributions under analysis, feature that suits well to the samples under test since they exhibit bi-modal structures in the studied spectra (see for instance Fig. 3.8). TS which are more sensitive to large-scale structure may give precedence to the latter when used as an ordering parameter in a clustering procedure. It has been observed that such behaviour gives rise to unwanted results, whereby bimodal and single-modal distributions are clustered together.

It is worth mentioning that, a generic not distribution-independent test statistic can not in principle be used as an ordering parameter; one is then forced to study the probability density function under the null hypothesis of the TS for each pair of tested distributions, comparing p-values derived from tail integrals of the TS. Besides being extremely CPU consuming, this also requires to use part of the data to construct the null distribution of the TS for each sample pair. This is not true for the case under study and the good properties of the selected binned likelihood ratio are then used to clusterise the parameters space.

4.2.3 The clustering technique

The clustering procedure exploits the previously computed TS in an iterative way, producing a grouping of the parameter space points into a given number of clusters (N_{clus}) based on the kinematical densities of the corresponding final states. It allows also to univocally identify the most representative sample in each cluster, which is called a *benchmark*, chosen as the sample which is the most similar to all the other samples associated to the same cluster. The procedure is based on an algorithm graphically described in Fig. 4.1 and defined as follow:

1. Consider each of the initial sample (N_{sample}) as one-element clusters.

2. Define the cluster-to-cluster *similarity* as $TS^{min} = min_{ij}(TS_{ij})$, where i runs on all elements of the first cluster and j runs on all elements of the second cluster.

3. Identify the benchmark sample in a cluster as the element k with the highest value of $TS_k^{min} = min_i(TS_{ki})$ between the clustered samples, where i runs on all elements of the cluster except k (if more elements have the same value of TS_k^{min}, the first one is taken by convention).

4. Find among all the possible pairs of clusters the two with the highest value of TS^{min}; merge the two clusters into one, and recompute the resulting benchmark.

5. Repeat step 4 above until N_{clus} clusters are left, keeping a record of all intermediate results.

For any given choice of the number of clusters the procedure returns the optimal clustering and the benchmark in each cluster. Of course, this implies the presence of a trade-off between intra-cluster homogeneity and the value of N_{clus}: as the latter decreases, more and more discrepant elements are clustered together; accordingly, the benchmark becomes less and less representative on the whole of the subset that contains it.

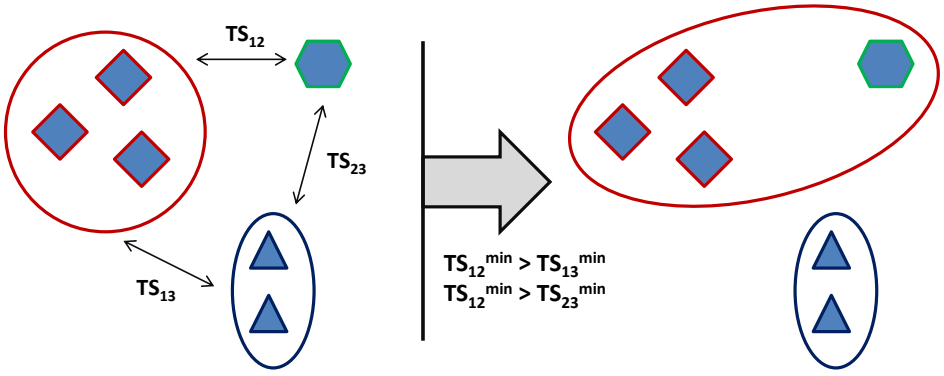

Figure 4.1: Graphical description of the clustering procedure; TS is the test statistic value described in Sec. 4.2.2; each circle identifies a cluster.

4.3 Results

The cluster analysis has been performed on the 1507 simulated samples, defined in Sec. 4.2.1, relying on m_{hh} and $|cos\theta^*|$ to characterize the final state kinematics produced by different values of anomalous Higgs (self-) coupling parameters. The previously described likelihood ratio TS has been computed among each pair of samples and the clustering algorithm has been performed in order to group those samples. The uniformity of the kinematic distributions inside each cluster is then used as parameter to identify the best choice of the final number of clusters.

4.3.1 Evolution of clustering with number of clusters

The total number of required clusters (N_{clus}), and therefore the total number of regions into which the parameter space is divided, is the only free parameter in the clustering procedure described in Sec. 4.2.3. The uniformity of the kinematical distributions within each cluster is a qualitative criterion which can be used to choose the target value of N_{clus}. A large number of clusters provides a finer sub-division of the parameter space and improves the uniformity of the kinematical distributions within each cluster. However, a too large number of benchmarks puts a heavy load on the experimental treatment of the data to probe the full parameter space. On the other hand, a too small N_{clus} can exhibit marked differences in the samples grouped together such that the corresponding benchmark does not appear suitable to accurately represent their behaviour.

In this specific application, it has been observed that strong discrepancies inside the clusters appear when N_{clus} becomes smaller than 12, while for $N_{clus} > 12$ the differences between the kinematical distributions of the samples included in different clusters start to become small enough to have a limited impact on the analysis design and corresponding selection strategy. At each iteration of the clustering algorithm the number of final clusters is reduced of one unit and two clusters are merged into a unique one, as shown in Fig. 4.2. In particular, the passages from $N_{clus} = 13$ up to $N_{clus} = 9$ are shown. It is evident that from $N_{clus} = 13$ to $N_{clus} = 12$ there is not a strong worsening of the distribution uniformity within the cluster.

Considering also the good uniformity of the distributions in each cluster, $N_{clus} = 12$ is the value chosen for the cluster analysis of the selected 1507 samples, a reasonable

trade-off between homogeneity and numerosity of the final clusters.

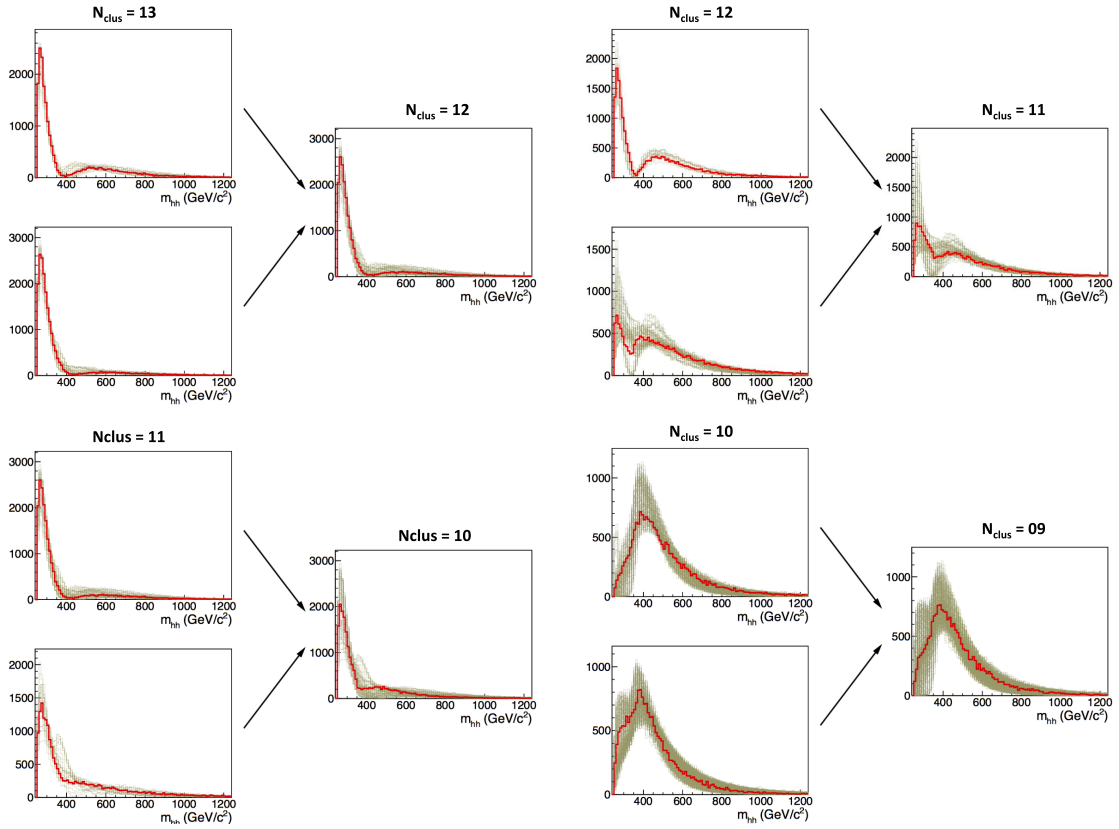

Figure 4.2: Distribution of the invariant mass of the Higgs bosons pair for samples grouped into a cluster, for different values of N_{clus}. The red distribution is the benchmark of the cluster. The merge of clusters due to the reduction of N_{clus} is highlighted. It is evident that the uniformity of the distributions inside the merged cluster remains good in the passage from $N_{clus} = 13$ to $N_{clus} = 12$.

4.3.2 Final results with $N_{clus} = 12$

The final number of cluster for this analysis has been set to twelve. The uniformity of the kinematic inside each of the 12 clusters can be seen in Fig. 4.3 for the m_{hh} and $|cos\theta^*|$ distributions. The Cluster 3 includes the SM point while the Cluster 4 includes the sample with unique contribution from the box diagram (k_λ = 0.0, k_t = 1.0 and $c_2 = c_g = c_{2g}$ =0). The Cluster 8, which presents the characteristic doubly peaked m_{hh} distribution, includes the sample with the maximal interference between the box and triangle contributions in the SM couplings scenario, i.e. the point defined by (k_λ = 2.4, k_t = 1.0 and $c_2 = c_g = c_{2g}$ = 0).

The clustering is clearly driven by m_{hh} variable. The impact of $|cos\theta^*|$ is expected to be small because all the different operators in our parametrization are predominantly s-wave (see for example [118]). This is evident in Fig. 4.3, where only few samples exhibit a non flat structure in $|cos\theta^*|$. These correspond to points of parameters space where there is a maximal interference between , *e.g.*, the box and triangle contributions, as in the Cluster 8.

In Fig. 4.4, the distribution of the higher Higgs boson transverse momentum among each pair (p_T^h) and the longitudinal momentum of the Higgs boson with the highest energy in the laboratory frame ($|p_z^h|$) are showed. Figure 4.3 and 4.4 visually confirm that the m_{hh} and $|cos\theta^*|$ constitute a robust choice to fully describe the kinematical features of the $2 \rightarrow 2$ process: no strong discrepancy in the momentum distributions is observed inside the clusters. The m_{hh} and $|cos\theta^*|$ distributions for $N_{clus} = 20$ can eventually be found in [119].

The parameter space values of the twelve final benchmarks are listed in Table 4.1. The benchmarks distribute rather evenly in the space of model parameters, without concentrations in specific corners of phase space; furthermore, both samples with and without Higgs-gluon contact interaction (c_g, c_{2g}) are represented in the set.

The choice of $N_{clus} = 12$ is not driven by any requirement on the position of the benchmarks in the parameter space nor on a particular sample to be represented as benchmarks. Even if there is no samples hierarchy in the cluster analysis, there is one sample of the parameter space which has to be taken as baseline in experimental searches: the one corresponding to the SM prediction. For the $N_{clus} = 12$ choice, the SM point is in Cluster number 3 and it is well represented by the relative benchmark. However, due to the intrinsic meaning of that sample, it is suggested to study all the twelve benchmarks plus the SM point, thus it has been added to Tab. 4.1.

Benchmark	κ_λ	κ_t	c_2	c_g	c_{2g}
1	7.5	1.0	-1.0	0.0	0.0
2	1.0	1.0	0.5	-0.8	0.6
3	1.0	1.0	-1.5	0.0	-0.8
4	-3.5	1.55	-3.0	0.0	0.0
5	1.0	1.0	0.0	0.8	-1
6	2.4	1.0	0.0	0.2	-0.2
7	5.0	1.0	0.0	0.2	-0.2
8	15.0	1.0	0.0	-1	1
9	1.0	1.0	1.0	-0.6	0.6
10	10.0	1.5	-1.0	0.0	0.0
11	2.4	1.0	0.0	1	-1
12	15.0	1.0	1.0	0.0	0.0
SM	1.0	1.0	0.0	0.0	0.0

Table 4.1: Parameter values of the final benchmarks selected with $N_{clus} = 12$. The third cluster is the one that contains the SM sample.

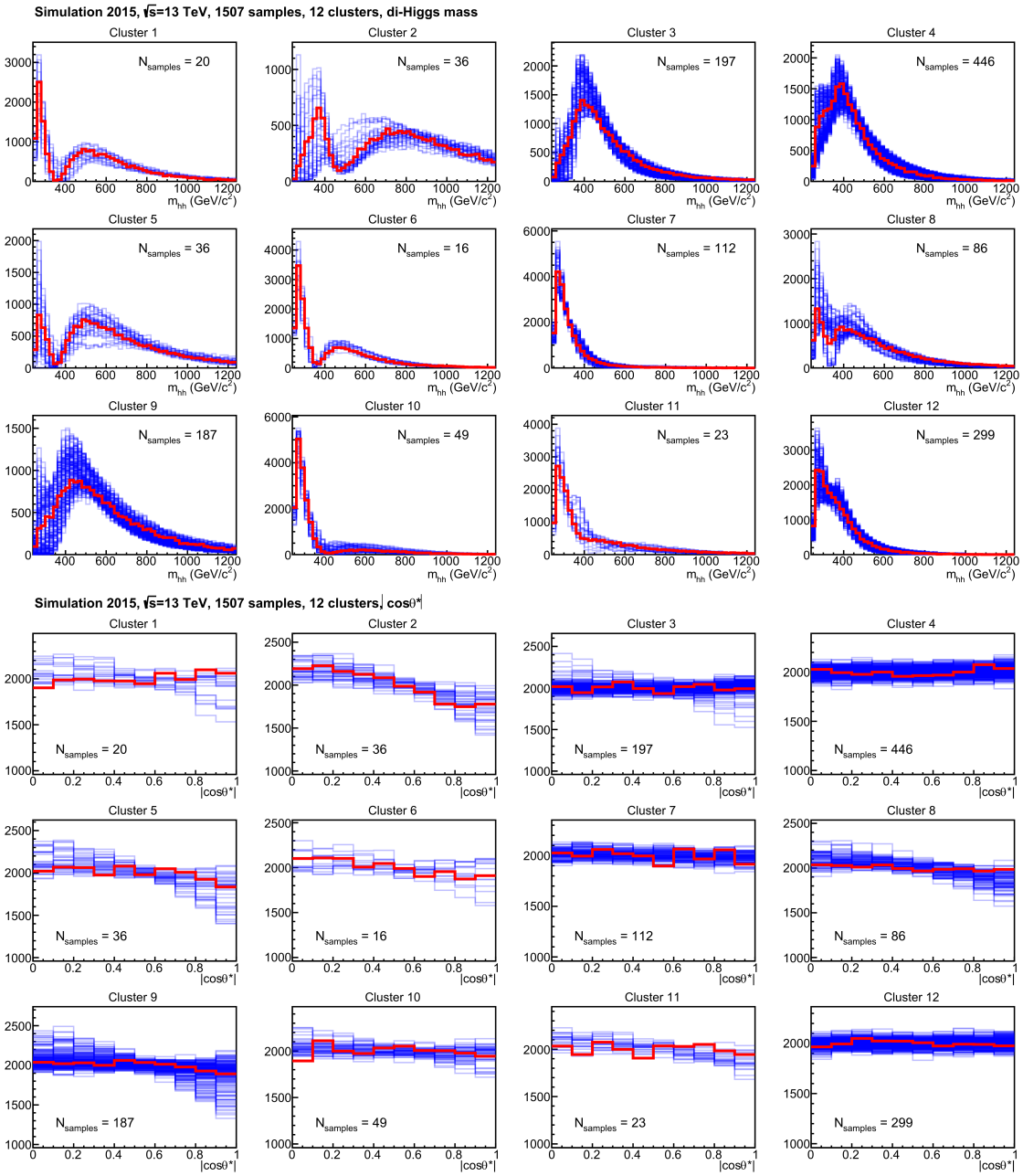

Figure 4.3: m_{hh} and $|cos\theta^*|$ distributions within each cluster for the final choice of $N_{clus} = 12$. The red distribution represents the benchmark sample while the blue ones are the other members of the cluster. Cluster 3 contains the SM sample.

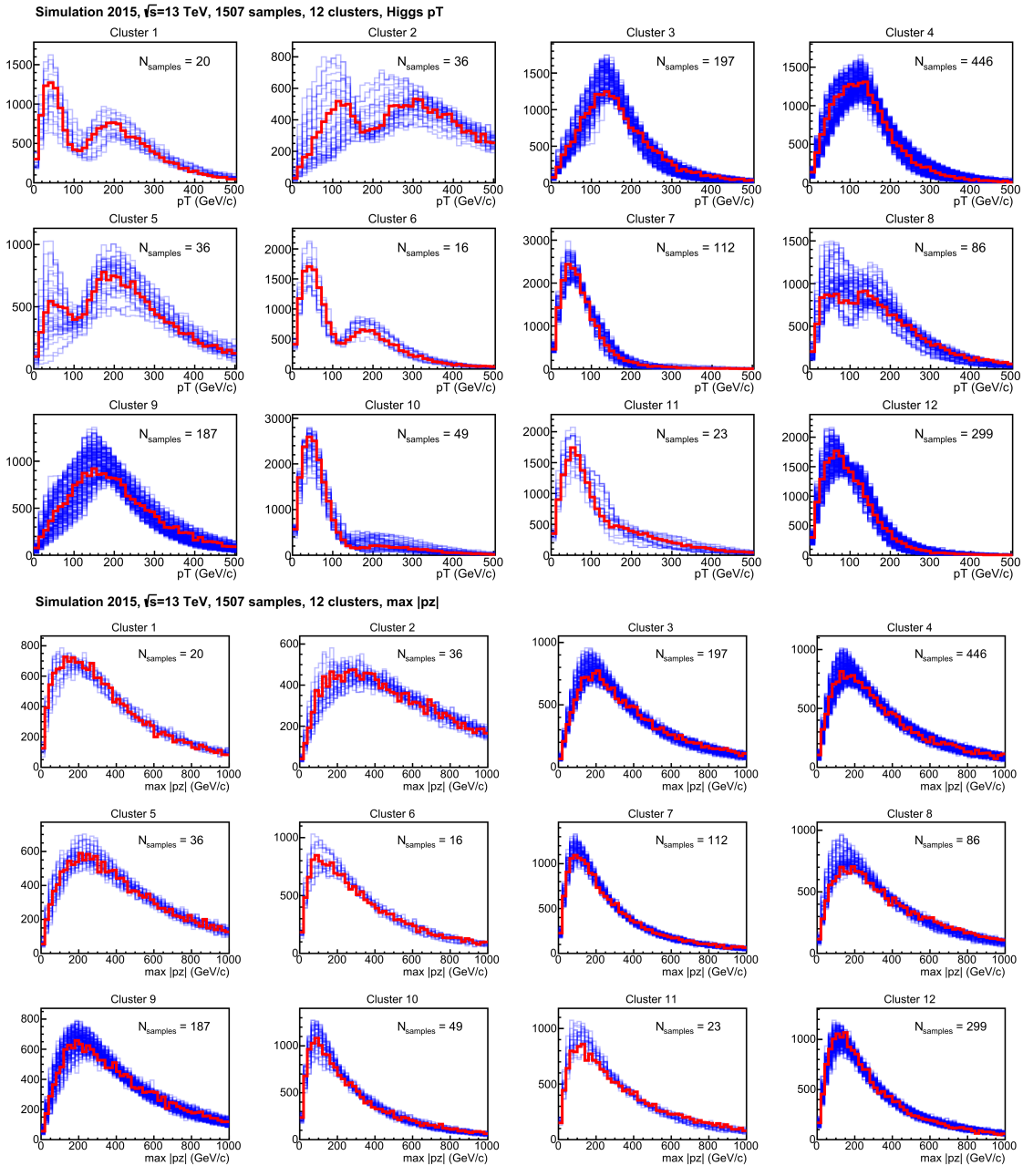

Figure 4.4: Higgs p_T and $|p_z^h|$ distributions within each cluster for the final choice of $N_{clus} = 12$. The red distribution represents the benchmark sample while the blue ones are the other members of the cluster. Cluster 3 contains the SM sample.

4.3.3 Maps of the clusters in the parameter space

The distribution of the twelve selected clusters in the parameter space is here described. To allow a graphical representation of the 5-D space, the space is divided into two-dimensional planes and the relative samples are plotted following a color code related to the final clusters. The shapes and colors of the markers have been chosen to describe how clusters and kinemtical distributions spread into the different parameter space regions. There is no logical ordering in the numbering of the clusters. The cross section iso-contours are also reported in gray.

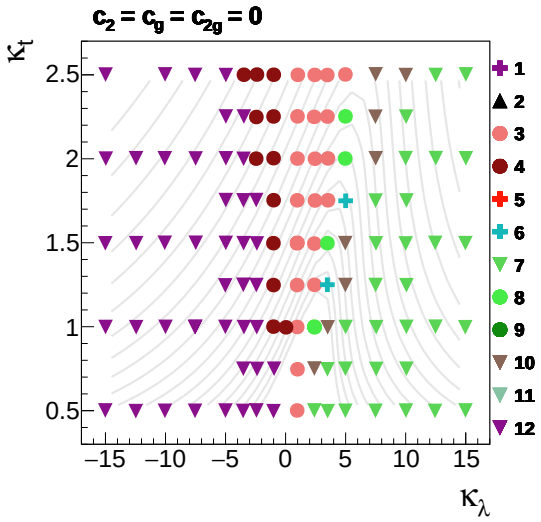

Figure 4.5: Distribution of clusters in the $k_\lambda \times k_t$ plane that contains the SM point. Cross section isolines are reported in gray. Triangles pointing downward symbolize clusters where the benchmark has Higgs p_T peaking at around 50 GeV or a smaller value. Circles describe clusters whose benchmark has Higgs p_T peaking around 100 GeV. Triangles pointing up describe clusters where the benchmark of the cluster has Higgs p_T peaking around 150 GeV or more. Finally, the crosses describe clusters that show double peaking structure in the m_{hh} distribution.

Figure 4.5 shows the clusters distribution in the $k_t \times k_\lambda$ plane, which is referred to as the *SM-like* plane. The SM point is located near a cross section minimum, where there are fine cancellations between triangle and box diagrams. The cluster analysis results confirm the kinematic variations next to the cross section minimum mentioned before.

Figure 4.6 shows the map of clusters in the $k_t \times c_2$ planes for different values of k_λ for the investigated points with $(c_{2g}; c_g) \neq 0$. The remaining parameter space regions are mapped in Fig. 4.7.

Finally, Fig.4.8 shows the relative variation of the value of the TS in three different planes with the superimposition of cross section iso-contours. The correlation between the TS maximal variation and the cross section minima is visible.

4.4 Summary of benchmarks study

The cluster analysis method described in this chapter has been developed to measure the kinematic similarity of samples in a wide parameter space. In particular, the GF Higgs bosons pair production at $\sqrt{s}$ = 13 TeV p-p collisions have been studied. The 5-dimensional parameters space, related to Higgs boson anomalous couplings, has been

analysed and twelve benchmarks have been identified. Moreover, the kinematical similarity in the parameters space have been described and possible singularities or regions with main variability have been checked.

The benchmarks are the most representative samples of the selected parameters space and they are sufficient to describe, up to a reasonable level of approximation, the possible different kinematic densities that may arise from arbitrary combinations of the parameters. Experimental study which focuses on these should not leave unexplored regions in the parameters space kinematic.

Furthermore, one can in principle extrapolate the results of an experimental search performed on a benchmark point to all the other points of the relative cluster. Whether that appealing plan is feasible remains to be proven, as it depends on the homogeneity of the intra-cluster kinematics. The first option can be the association of a systematics to the limit extrapolated from the benchmark study. The systematic computation can be based on the distance (TS) of the selected parameters space point from the benchmark but this is not guaranteed to be exhaustive. Further studies are under development, such as the idea to perform a full analysis on the two points per cluster that are kinematically farthest from the benchmarks to get an indication of variation based directly on the final limit.

The cluster analysis has been performed on the generator-level samples, whose production is extremely less time consuming than the full simulated ones. In an ancillary study, several samples belonging to the same cluster have been fully simulated and their kinematical similarity has been verified. This lead a confirmation of the validity of this cluster analysis technique.

To retain generality of the cluster analysis, the Higgs boson decay modes are not considered in this study. The list of benchmarks is thus valid for all the final state searches. The $\gamma\gamma b\bar{b}$ final state of HH decay is expected to be the most sensitive one to local changes in the m_{hh} spectra; however other decay channels, such as the fully leptonic $WWb\bar{b}$ or $b\bar{b}$ $b\bar{b}$, could in principle be equally sensitive to small shape variations in different regions of hard sub-process energy, especially with the development of multi-variate analysis techniques. With increased statistics of the analysable data, fine structures in the kinematics -in particular in the m_{hh} distribution, *e.g.* in clusters 4, 6, and 7 - will become more interesting and may call for a more specific study of the corresponding regions of parameter space.

This cluster analysis approach has been approved by the LHC Higgs Cross Section Working Group [120] and the results will be used as a guideline for the searches of non-resonant di-Higgs production in the LHC Run 2. This study has been reported in [102], currently in editorial review for publication on JHEP, and it will be also included in the next official report of the LHC Higgs Cross Section Working Group.

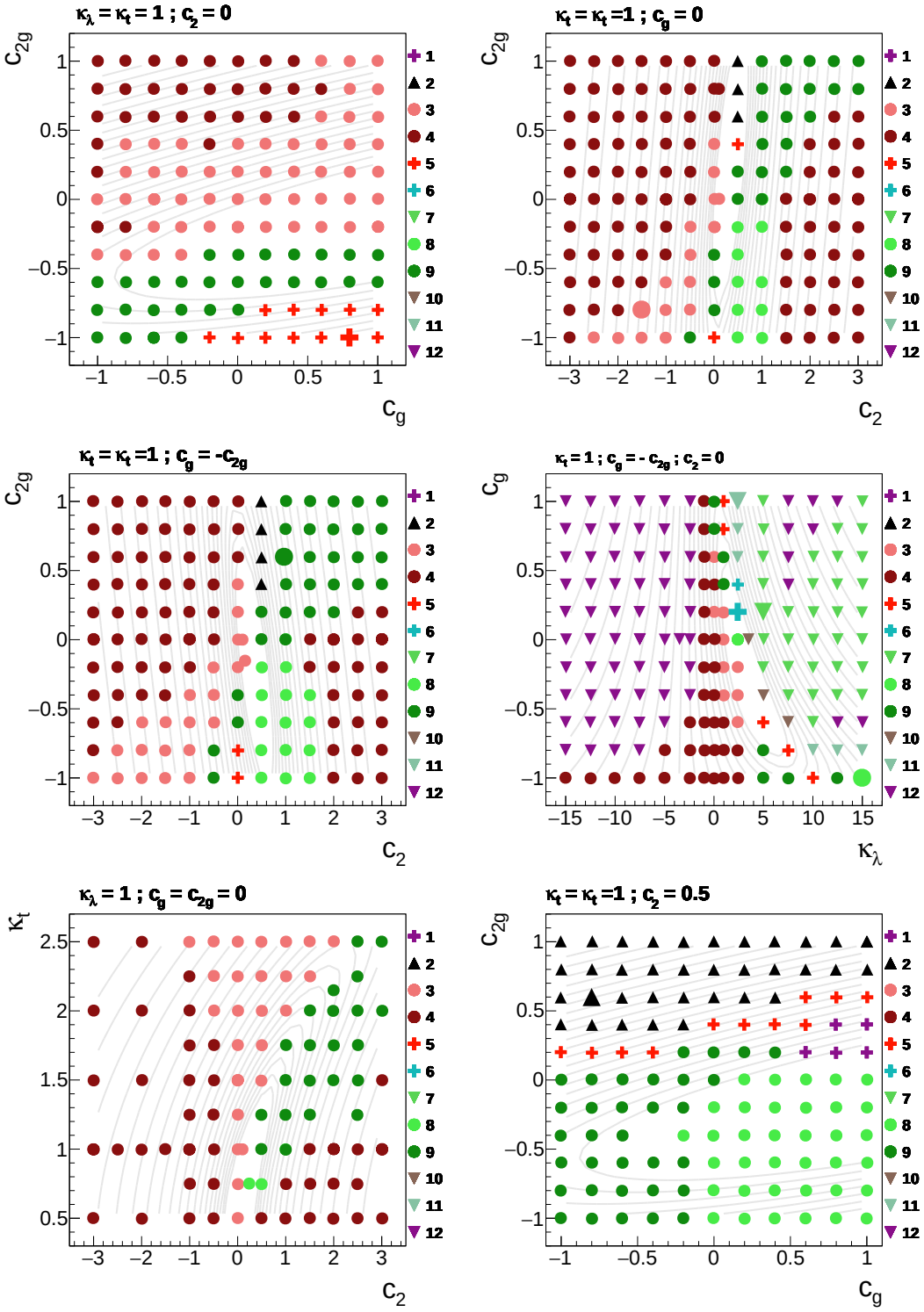

Figure 4.6: Distribution of clusters in various sliced of the 5-D parameters space. The different shapes of the markers represent different regimes of Higgs boson p_T, as described in the caption of Fig. 4.5.

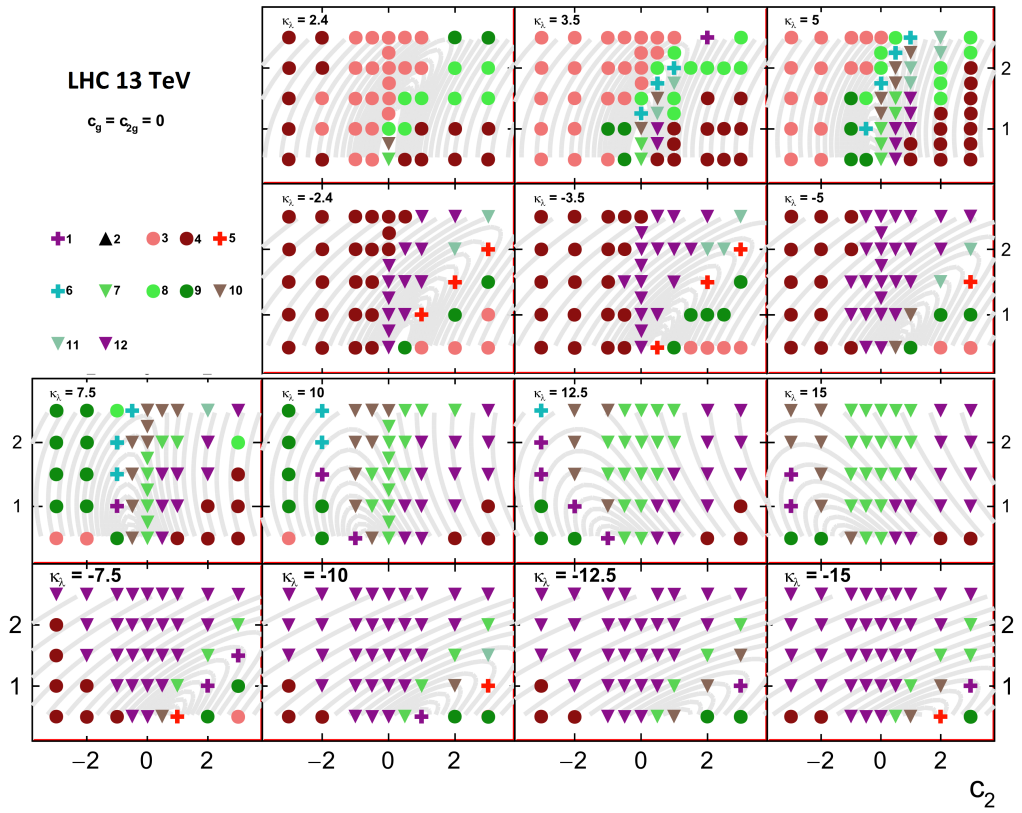

Figure 4.7: Distribution of clusters in the in the $c_2 \times \kappa_t$ parameters plane for different values of κ_λ when $(c_g, c_{2g}) = (0, 0)$. The different forms represent different regimes of Higgs boson p_T, as described in the caption of Fig. 4.5.

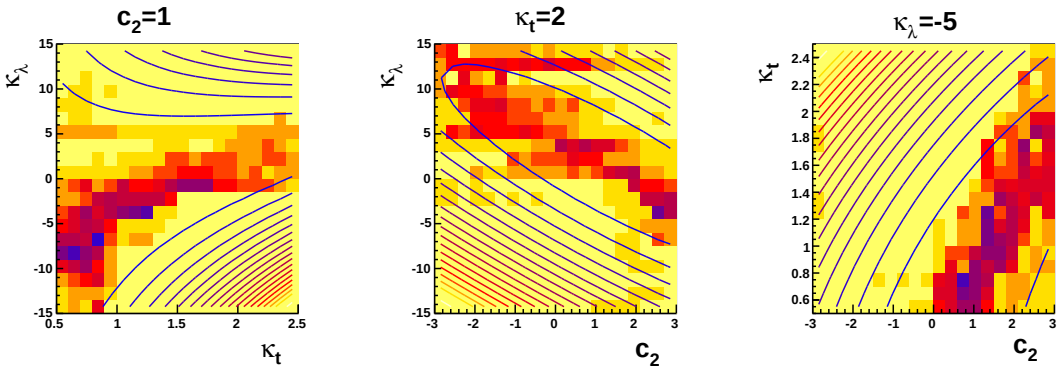

Figure 4.8: Superposition of isolines of cross section and colour maps of the speed at which the likelihood test statistic described in Section 4.2.2 varies as one moves around in three selected two-dimensional surfaces of the five-dimensional parameter space of BSM theories. The cross section decreases in the direction where the density of isolines decreases. Blue and red tones in the colour maps indicate the highest variation in the TS values; the colour scale is arbitrary. The behaviour observed in the graphs is common to all investigated two-dimensional planes.

Chapter 5

Study of the non-resonant hh $\rightarrow b\bar{b}\,b\bar{b}$ channel

A preliminary study of non-resonant Higgs bosons pair production on the data collected by the CMS experiment in 2015 in p-p collisions at $\sqrt{s}$ = 13 TeV is here reported. The process has been studied looking at the full hadronic decay channel, with both Higgs bosons decaying into b-quark pairs. The comparison of the performances of three methods for the jets selection and pairing, and a preliminary data-driven background estimation method are shown. Future prospects are also described.

5.1 Introduction and analysis strategy

The production of Higgs bosons pairs (*di-Higgs*) represents the golden channel to study details of the SM Higgs potential and to directly access to the Higgs self-coupling. The di-Higgs production in a non-resonant final state has not been observed yet and it is expected to be a rare process accordingly to the SM. The predicted SM cross section in p-p collision at $\sqrt{s}$ = 13 TeV is equal to 34.3 $\pm$ 1.0 $\pm$ 0.7(PDF) fb [94, 95]. The low production cross section, together with an elevated irreducible background, make the process accessible only with a huge amount of collected data ($\mathcal{O}(1)ab^{-1}$) and thus the measurement, in the SM hypothesis, is not expected with data collected by the CMS experiment so far. As described in the Section 3.4.1, the non-resonant production cross section can be enhanced if the process occurs via anomalous couplings not expected by the SM. By exploiting the data collected by the CMS experiment it is thus possible to set up a search strategy that, in case of no signal excess, may allow to set upper limits on the SM di-Higgs non-resonant production cross section and to exclude some region of the parameters space related to BSM couplings.

The four b-quarks final state presents the highest branching fraction and it is potentially the best channel to search for with this low amount of collected data, as it has been confirmed by ATLAS experiment in the Run 1 searches [107]. In the CMS experiment, the $b\bar{b}b\bar{b}$ searches can exploit the high tracking efficiency and the good b-tagging performances shown in Sec. 1.2.8.

The main challenge for this analysis is the presence of multi-jet processes with a cross section several orders of magnitude larger than the signal one. Such events represent an irreducible background, which differs from the signal only for the di-jet invariant mass and different distributions in some kinematic variables, such as the p_{T} spectra of the jets. The multi-jets background is mainly due to QCD interactions. A contribution from $t\bar{t}$ production is also present ($\mathcal{O}(10)$%). A requirement on the number of b-tagged jets in

each event can reduce the amount of multi-jets background events but the contamination from that process still remains considerable also because of the b-tagging algorithm misidentification rate. Furthermore, an irreducible $b\bar{b}b\bar{b}$ contamination from multi-jets QCD process is present. An accurate prediction of the multi-jet background yield and shape is required to preserve the sensitivity of the analysis, but simulation is not reliable for a quantitative background determination because of the uncertainties and imperfect modelling of multiple b jets production in gluon splitting and flavour excitation processes. For these reasons, a background prediction technique based on data, so-called data-driven method, needs to be developed.

The multi-jets background, together with the PU, lead to an high number of events with more than four jets and a source of background comes also from the mis-identification of the two final jets pairs. Thus, the optimization of jets selection and pairing is another key element of the di-Higgs search in the fully hadronic final state since it can minimize this combinatorial background.

A feasibility study for the search of the $hh \rightarrow b\bar{b}b\bar{b}$ non-resonant production is here reported. Preparatory studies have been performed to identify the best data selection on which perform a two dimensional shape fit in order to extract the signal over the irreducible background.
The planned analysis strategy is summarized as follow:

1. Trigger and kinematic acceptance requirements
2. Four b-tagged jets selection and pairing
3. Data-driven estimation of the background
4. Multi-variate technique to increase the significance
5. Bi-dimensional unbinned shape fit
6. Upper Limit extraction via a maximum likelihood fit

Details of the first three steps are described in the next sections.

5.2 Data and simulated samples

The signal and background samples have been produced with the Monte Carlo (MC) simulation tools used by the CMS collaboration.

The signal sample corresponding to non-resonant SM $hh \rightarrow b\bar{b}b\bar{b}$ has been simulated with 300000 events. The signal sample has been generated using the setup developed by the authors of [110]. It is based on MADGRAPH 5.1 [121] plus a `Fortran` routine on top of an *aMC@NLO* [111, 112] effective model; the `NN23LO1` PDF set [113] is used. The response of the CMS detector is modelled using GEANT4 [122].

The background contributions to the signal signature come from multi-jet production via non-resonant processes such as QCD and top pairs production. Simulated samples have been generated for both QCD and $t\bar{t}$ processes. MADGRAPH 5.1 is used to generate the $t\bar{t}$ samples while QCD multi-jet samples are simulated with PYTHIA [123]. The response of the CMS detector is modelled using GEANT4.

These multi-jet events are dominated by QCD processes due to the extremely large cross section of those reactions. The main QCD production processes for four b-jets are shown in Fig. 5.1.

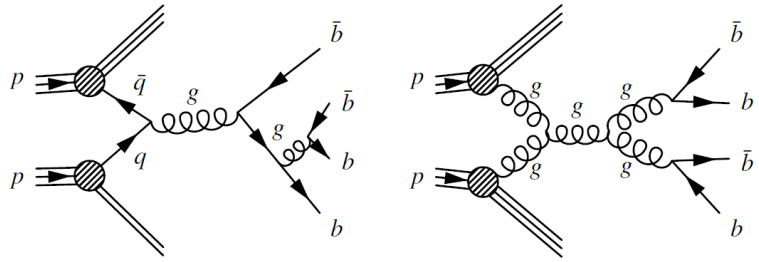

Figure 5.1: Example of lowest order Feynman diagrams for QCD multi-jet production with quarks and gluons in the initial state contributing to the four b-jets final state.

The events with four b-tagged jets with relatively high p_{T} are a small fraction of the entire QCD multi-jet processes, thus a large statistics in the QCD MC sample is needed to finally get a reasonable amount of events in the region of interest. Furthermore, the MC simulation of QCD multi-jet events does not present a good agreement with data due to difficulties in the modelling of QCD processes. Thus, large scale factors have to be applied to the MC to take into account these discrepancies. This said, the simulated samples are taken as a reference but not exploited in the analysis where a data-driven technique have to be implemented to model this irreducible background.

The analysis is performed on the data collected during the whole 2015 corresponding to a total integrated luminosity of 2.19 ± 0.09 fb^{-1}. Full hadronic events are selected in both data and MC samples by using the triggers described below.

5.3 Trigger

Standard multi-jet triggers have been developed by CMS to identify event topologies that include the presence of jets. These can not be easily used for the specific four b-jets final state due to the immense rate of QCD multi-jet events. The multi-jet trigger usually present a relatively high cut on the p_{T} of the jets and this does not fit with the requirement of the analysis here presented. In order to have low jet p_{T} thresholds and an acceptable rate, the b-tag information has been exploited at HLT level. The use of b-tagging at trigger level also reduces the multi-jet QCD contribution to the selected data sample. Actually, the multi-jets production is estimated to be higher for the $\mathrm{b\bar{b}}$ $\mathrm{c\bar{c}}$ and $\mathrm{b\bar{b}}$ jj (being j a light quark) with respect to the $\mathrm{b\bar{b}}$ $\mathrm{b\bar{b}}$. This leads to an additional background contribution if both the light jets are misidentified as originated from a b-quark. An off-line b-tagging selection with a medium working point allows to reduce this contribution.

Two paths have been implemented and were operating during the 2015 data taking period: *QuadJet45_TripleCSV0p67* and *DoubleJet90_Quad30_TripleCSV0p67*. These HLTs are based on the CMS trigger structure and jet reconstruction algorithm, described respectively in Sec. 1.2.9 and 1.2.8. The two HLTs differ essentially from the requirements on the transverse momentum of the jets. The cut on the b-tagging is applied to three jets in both paths. This requirement has been changed with respect to the HLT used on the resonant di-Higgs searches at LHC Run 1 [106], where the b-tag were required on 2 jets only. This change was driven by the necessity to improve the trigger performances for low region of the four body mass spectrum ($\sim$ 200-300 GeV), i. e., to keep low the selection threshold on jets p_{T}.

The two paths are based on a Level 1 (L1) trigger where two, three or four jets clusterized with anti-k_t algorithm and reconstructed with Particle Flow algorithms. Events with four HLT jets above optimized p_{T} thresholds are selected, and then a loose b-tagging for three of the four E_T-leading jets at HLT Level 3 (L3) is required. The trigger employs the on-line version 2 of the Combined Secondary Vertex algorithm (CSVv2), described in Sec. 1.2.8.
The details of the two HLT structures are reported below.

DoubleJet90_Quad30_TripleCSV0p67:

- L1 logical combination of different triggers:
  - L1_DoubleJet100, two central jets with $p_{\mathrm{T}} > 100$ GeV.
  - L1_Triple_Jet92_76_64, three central jets with $p_{\mathrm{T}} > 92$, 76, 64 GeV respectively.
  - L1_HT175 or L1_HTT100 or L1_HTT125 or L1_HTT150.
- Reconstruct anti-k_T ($\Delta R = 0.4$) CaloJets:
  - 4 jets with $|\eta| < 2.6$ and $p_{\mathrm{T}} > 30$ GeV
  - 2 jets with $|\eta| < 2.6$ and $p_{\mathrm{T}} > 90$ GeV
- Update Fast Primary Vertex Reconstruction
- CSV computation (8 jets L3):
  - 3 CaloJets with CSV > 0.67
- PF Jet ID
- PF Reconstruction Sequence
  - 4 PF jets with $|\eta| < 2.6$ and $p_{\mathrm{T}} > 30$ GeV
  - 2 PF jets with $|\eta| < 2.6$ and $p_{\mathrm{T}} > 90$ GeV

The Fast Primary Vertex algorithm reconstructs the primary vertex using only the CaloJets and the hits from the pixel sub-detector, before the full tracks reconstruction is available. Then, once the strip detector information is available, the algorithm reconstructs only tracks which are compatible with the reconstructed primary vertex. This algorithm reduces by a factor 3 the time needed by an algorithm that starts without primary vertex information.

QuadJet45_TripleCSV0p67:

- L1 logical combination of different triggers:
  - L1_QuadJet60, four central jets with $p_{\mathrm{T}} > 60$ GeV.
  - L1_QuadJetC40, four central jets with $p_{\mathrm{T}} > 40$ GeV.
  - L1_HTT100 or L1_HTT125 or L1_HTT150 or L1_HTT175.
- Reconstruct anti-k_T ($\Delta R = 0.4$) CaloJets:
  - 4 jets with $|\eta| < 2.6$ and $p_{\mathrm{T}} > 45$ GeV
- Update Fast Primary Vertex Reconstruction
- CSV computation (8 jets L3):
  - 3 CaloJets with CSV > 0.67
- PF Jet ID
- PF Reconstruction Sequence

- 4 PF jets with $|\eta| < 2.6$ and $p_T > 45$ GeV

In order to get a further reduction of the event rate, the last requirement on the particle flow jets has been added after the selection on the CaloJets. Particle flow jets, which are used in the offline analysis, in fact are reconstructed with a better resolution with respect to CaloJets.

Studies on the trigger efficiency are currently on-going. The efficiency for the various steps of each triggers are factorized and separately computed. Figure 5.2 shows, as an example, the turn-on curves related to the cuts on the CaloJets in *DoubleJet90_Quad30_TripleCSV0p67*.

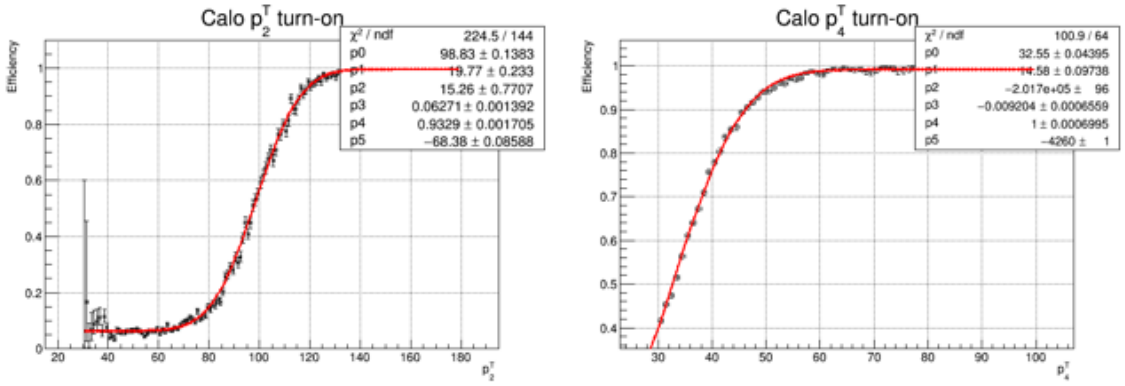

Figure 5.2: Trigger efficiency after the requirement of 2 CaloJet with $p_T > 90$ GeV (left) and 4 CaloJet with $p_T > 30$ GeV (right).

Additional *soft-leptons* triggers can be considered for future developments. These triggers are based on b-tagging algorithm which searches for one lepton produced in a semi-leptonic B decay. The soft-leptons algorithm can allow to reject a good fraction of multi-jet background but it has still a too lower b-tagging efficiency with respect to the CSV algorithm.

5.4 Events reconstruction and selection

The $hh \rightarrow b\bar{b}b\bar{b}$ search with the CMS experiment is based on jets reconstruction technique and jet b-tagging algorithm described in Sec. **??**. The Combined Secondary Vertex version 2 (CSVv2) algorithm is used to identify jet produced by a b-quark hadronization.The standard CSVv2 working points are used: 0.605 for loose b-tag, 0.890 for medium b-tag and 0.970 for tight b-tag. Accordingly to the CMS convention, they correspond respectively to a 10%, 1% and 0.1% probability of misidentifying a light jet as a b jet. The events of interest are identified and recorded by using the triggers previously described. The trigger efficiency on the signal selection is 30%. Loose kinematical cuts are then applied on all the reconstructed jets in each event:

$$p_T^{jet} > 20GeV, \qquad |\eta_{jet}| < 2.5. \tag{5.1}$$

The cut on η selects central jets only. This is in line with what is required on-line by the trigger algorithm and, in fact, the presence of this cut leads only to a 0,2% reduction of the signal accepted by the trigger selection. The cut on p_T is considered as a baseline to not reject possible low energy jets with a consequent signal reduction.

At least four jets are finally required in the event and the jets b-tagging is considered. Only events with at least three medium b-tagged jets are selected. The fraction of events

that passes these preliminary selection is equal to 17%. The choice of a medium b-tag cut with respect to a tight b-tag relies essentially on the necessity to not heavily reduce the signal acceptance. A request of 3 jets with tight b-tag leads in fact to only a 5% of the signal while a 26% results from the choice of three loose b-tag. The percentage of mis-tagged jets with the loose b-tag is too high to be considered as a baseline selection for this analysis, extremely influenced by a combinatorial background. The reduction flow for the SM like signal is reported in Tab. 5.1. This cut-flow is applied to both the SM signal and the data.

	Trigger	4 Jets in Acc.	3 med b-tag
Efficiency	30.0%	29.7%	17%

Table 5.1: Cutflow efficiency for the SM like signal. The "Jets in Acc." are required to have $p_T >$ 20 GeV and $|\eta| < 2.5$. The medium b-tag correspond to CSVv2 = 0.890 .

A selection on the b-tag value of the fourth jet is not considered in this baseline cut-flow. This cut will be in fact used to discriminate signal like and background like data. In particular, the *3 b-tagged* category will require a medium b-tag on three jets before the final selection while for the *4 b-tagged* category a loose b-tag request of the fourth final selected jet will be added.

The number of jets per event is on average ~ 7, as shown in Fig. 5.3. It is reduced after the baseline selection but the number of events with more than four jets is still high. The fourth jet selection and the following jets pairing are thus extremely important to avoid the possible combinatorial background. The probability to select a jet not coming from the decay of the Higgs boson is not negligible and different methods to perform this selection have been studied, as described below.

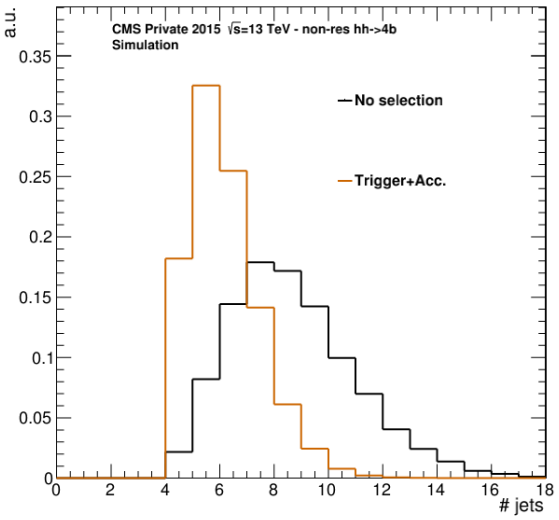

Figure 5.3: Jets per event multiplicity for SM like signal in events with $p_T^{jets} < 15$ GeV (black) and after trigger and acceptance cuts (ochre); at least four jets are required in both distributions and a normalization to unity is applied.

5.4.1 Four jets selection and pairing

Different selection methods have been compared in order to minimize the presence of combinatorial background.

The study has been performed on signal MC in order to exploit information coming from generator level particles. The *purity* of the selection is defined as the fraction of the selected jets which corresponds to the MC truth, i.e., to the B hadron at generator level. To measure the selection purity, the angular distance $\Delta R = \sqrt{(\Delta\eta)^2 + (\Delta\phi)^2}$ is measured between each reconstructed jet and the four generated B hadrons. If $\Delta R < 0.5$, the reconstructed jet is marked as matched with the relative generated B hadron. The jet with lower ΔR is taken if more than one jet is below 0.5. This ΔR criterion allows to identify the matching of a reconstructed jet with a generated B hadron.

The four selected jets are then paired into two final di-jets and the validity of this pairing has also to be considered to compute the final purity. It is thus checked if the generated B hadron, which matches with the two paired jets, are the decay products of the same Higgs boson.

The selection of the four jets can be based on several jet level information, such as the CSVv2 discriminator value or kinematical variables of the jets (p_T, η, etc.). The b-tagging is surely the most powerful tool to look at. The proper matching of the three jets with the highest value of CSVv2 discriminator in each event is equal to the 76%. In particular, in 28% of the events the first jet in CSVv2 is not matched, 33% for the second jet in CSVv2 and 45% for the third. This 76% purity is a good baseline for the selection and thus the three reconstructed jets with highest value of CSVv2 per event are selected, referred to as *final jets*.

Three different methods have instead been considered for the selection of the fourth jet per event:

- 4 highest CSV (4HighestB): take the jet with the fourth highest value of CSVv2.
- 3 highest CSV + 1 free (3HighestB): do not apply any selection on the 4th jet.
- 3 highest CSV + Relative Likelihood (RL): implement a multi-dimensional binned relative likelihood method to select the fourth jet by looking at the distribution of its kinematical variables.

Once the four final jets are selected, their pairing is performed by looking at the invariant mass of the two di-jets candidates Δm_{jj}. All the combinations are checked and the one which presents the minimal difference in mass between the two di-jets is considered as final. This scan is performed among the fourth selected jet for the 4HighestB and RL methods while all the other jets in the event (in addition to the three selected) are considered in the 3HighestB method. The purity of the selection depends strongly on this pairing option. In fact, only a 40% of the events that present well matched jet are also well paired. This value depends on the method used for the fourth jet selection but its variation is around 5%.

5.4.1.1 Relative Likelihood method

The RL method has been developed to maximally exploit the information related to the fourth jet. The general idea is to extract the value of a set of variables for the fourth jet candidate and to compare them with the typical distribution for a matched jet. This can be implemented through a relative likelihood approach as follows.

Firstly, half of the MC signal sample is considered to compute the binned likelihood. The following steps are performed in each event:

1. The three jets with highest value of b-tag discriminator are selected.

2. The matching with a generated B hadron is checked for all the remaining jets in the

event, the so-called fourth jet candidates. The $\Delta R < 0.5$ criterion has been used to identified the matched jet.

3. A binned matrix is then filled accordingly to the value of selected variables related to the fourth jet. Two matrices are filled, one for the matched jet and one for the not matched jets.

Once the first half of the signal sample has been analysed, the ratio between those matrices is computed and the relative binned matrix is filled. This ratio represents the likelihood for a fourth jet to be matched with a B hadron and it is exploited once the RL method is applied.

In the RL method application phase, in each event:

1. For all the fourth jet candidates, accordingly to the values of the considered variables, the ratio in the relative bin is associated to the jet.

2. The jet with maximum value of R is taken as the final fourth jet.

This method has been applied on the SM signal, half of the sample has been used for the computation of the ratio and half for the application and testing.

The main tool of this method is the identification of the jet variables to be exploited. Several possible variables related to the fourth jet have been scanned. The most discriminant ones, shown in Fig. 5.4, have been found to be the p_T, $|\eta|$, CSVv2 value and the charge multiplicity. The latter is defined as the number of reconstructed charged particles in each jet. The value of the jet b-tag discriminator is considered in the categorization of data and thus it is preferable to not use it as fourth jet selection criterion.

The size of the bins have been modified in order to optimize the RL performances and the following binning has been implemented: 10 bins in p_T, 9 uniform up to 270 GeV and 1 above; 4 bins in $|\eta|$ [0-1],[1-1.5],[1.5-2],[>2.5]; 6 bins in charge multiplicity, 5 uniform up to 20 and 1 above.

5.4.1.2 Methods comparison

The three methods have been applied to the SM signal sample and the purity has been measured on both 3 b-tagged and 4 b-tagged categories, as reported in Tab. 5.2.

The 4HighestB method provides the highest purity for the 3 b-tagged category. The purity obviously increase for the 4 b-tagged category and the 3HighestB method results to get the higher purity value, about 56%. However, the event reduction in the 4 b-tagged category is too large and the collection of all selection requirements with the 3HighestB leads to only a 6.8% of the initial events.

4th jet selection	jets pairing	Purity (3 b-tagged)	events 4 b-tagged	Purity (4 b-tagged)
4HighestB	min Δm_{jj}	40.9%	31499 (11%)	49.5%
3HighestB	min Δm_{jj}	33.5%	18764 (6.8%)	56.4%
RL	min Δm_{jj}	33.4%	10174 (7.4%)	54.2%

Table 5.2: Purity of the jets selection for three different methods to select the fourth jet; purity is reported for the 3 b-tagged and 4 b-tagged category, together with the final number of events.

In Fig. 5.5, the distribution of the reconstructed di-jets are shown, together with the relative fraction of matched di-jets. The two possible di-jets are classified accordingly

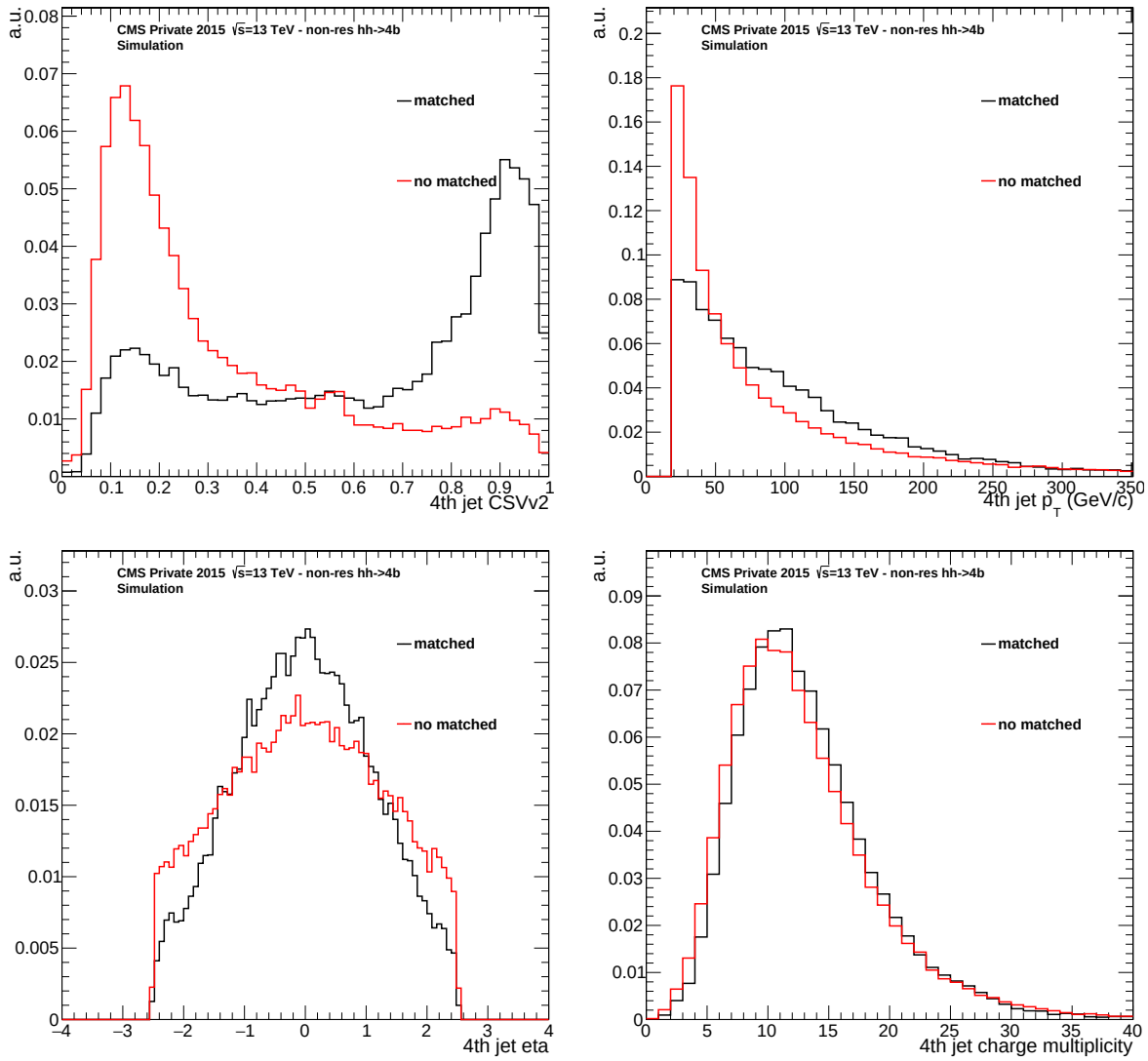

Figure 5.4: Distribution of the CSVv2 discriminator, p_{T}, $|\eta|$, charge multiplicity of the fourth jet; the last three have been used in the RL method; jet matched with a generated B hadron and all the other possible jets are shown; distributions are normalized to unity.

to their invariant mass in leading di-jet and trailing di-jets. From those distribution, it is evident that the mis-matching leads to a tail to higher mass value, especially with the RL method. The distribution of the leading di-jets is peaked around 125 GeV as a consequence of the choice of the ”minimal mass difference” as paring criterion. The distribution for the trailing di-jets presents a low mass tail too. This is present in both matched and non-matched di-jet and it depends on jet recontruction resolution effects. Those can be partially corrected by applying jet regression techniques **[jetReg]** which reduce the width of the mass distribution.

The final purity of the selection and pairing allows to compare those three methods but can not be considered as the unique figure of merit to define the best option. This study indicates that the four jets with the highest b-tag probability present a good purity and allow a relative small signal rejection in the 4 b-tagged category. A more detailed description of the signal statistics as a function of these three methods is presented in the next section and will be considered for the final choice.

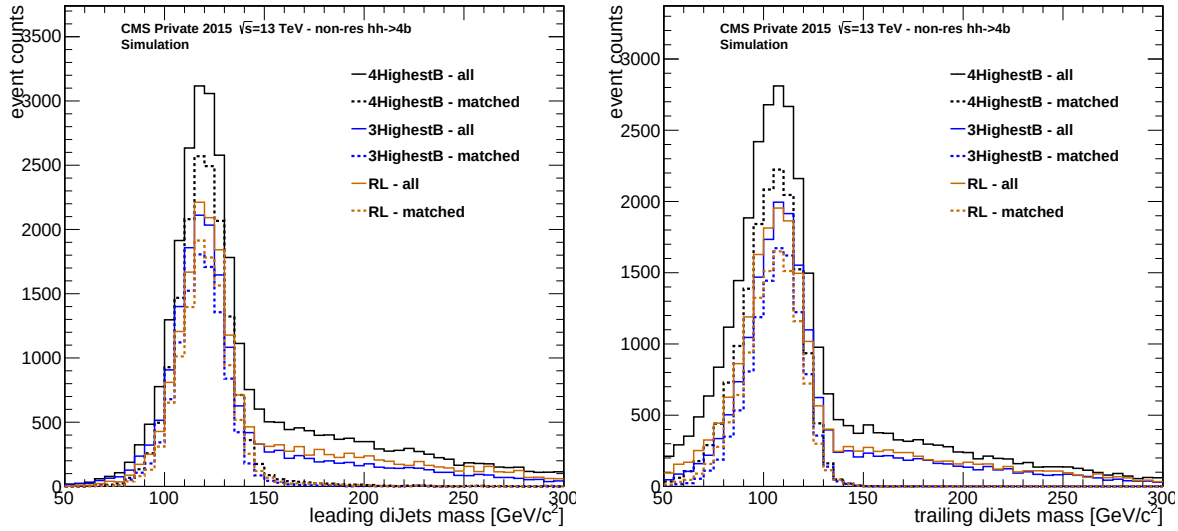

Figure 5.5: Distribution of the invariant mass for the leading (left) and trailing (right) reconstructed di-jets. The three methods for the 4th jet selection are compared and the relative fraction of matched di-jets is also shown.

5.5 Signal region description

The signal is not expected to present a peaked distribution in the four body mass spectrum due to the non-resonant nature of the process. This broad signal distribution lies over an irreducible background whose shape is quite similar, so the signal extraction can not be based on the fit to this 1-dimensional four body mass distribution. The mass of each Higgs boson is more reliable for the signal extraction and it allows to perform a shape fit on a 2-D plane, which is a more powerful tool.

The 2-D plane selected to perform the final shape fit is composed by the masses of the two Higgs candidates. The two candidates, i.e. the two di-jets are divided in leading and trailing depending on their invariant mass. This brings to an increment of the statistic in each 2-D bin and the resulting plane is shown in Fig. 5.7.

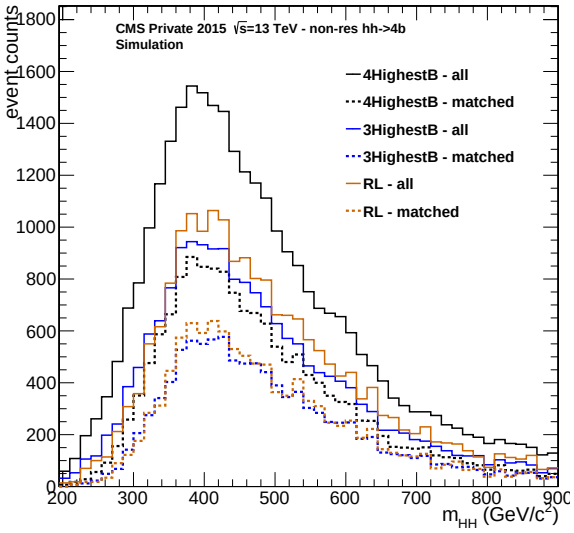

Figure 5.6: Distribution of the four body invariant mass from the reconstructed di-jets in the 4 b-tagged category. The three methods for the 4th jet selection are compared and the relative fraction of matched di-jets is also shown.

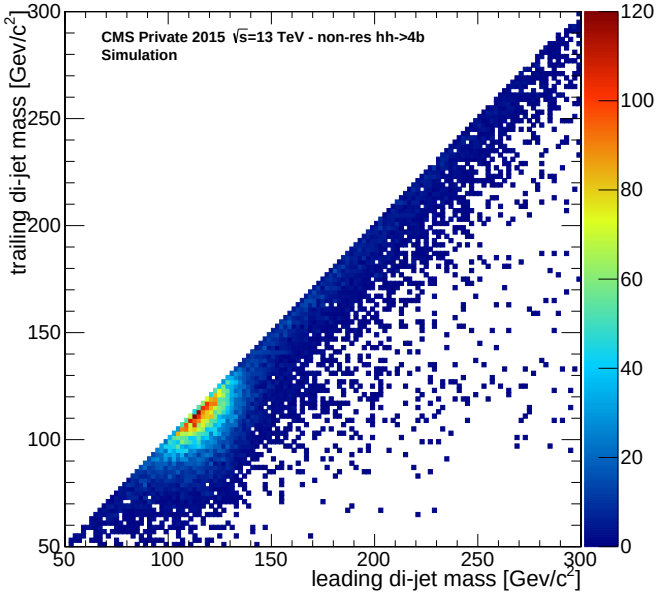

Figure 5.7: 2-D plane for the SM signal in the 4 b-tagged category, as resulting from the 3HighestB selection method; number of entries per bin is on the z-axis.

The significance in the whole 2-D plane is expected to be extremely low and a region with the highest fraction of the signal has to be identified. In this region, which will be referred to as signal region, the shape fit will be performed. The complementary region of the 2-D plane will then be exploited to perform the data-driven background estimation. The background modelling will be extracted looking at this region, thus the fraction of the signal outside the SR needs to be as low as possible.

This signal region has been defined as an ellipse with the focuses on the plane diagonal, as shown in Fig.5.8. Since the di-jets mass distributions are not centred to the nominal Higgs mass value (125 GeV), the ellipse has been centred on the mean of the trailing di-jets, corresponding to 113 GeV. The size of the ellipse has been optimized to get the higher fraction of signal in it and final value of radius has been set to r=40 and R=60.

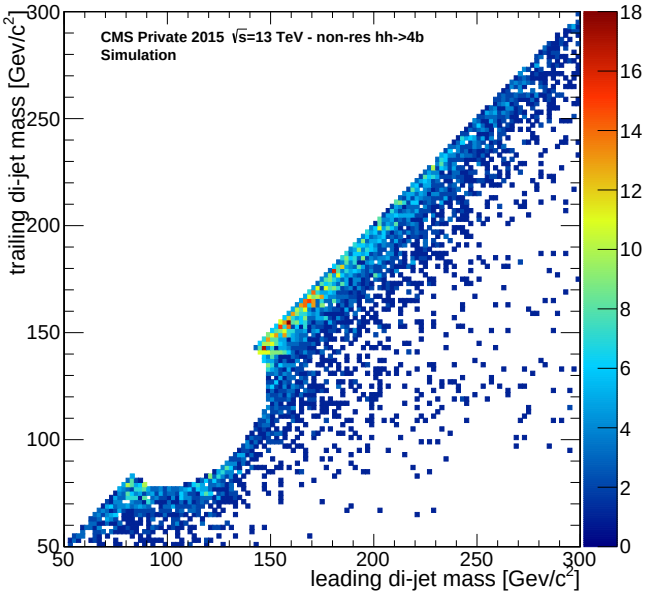

Figure 5.8: 2-D plane for the SM signal in the 4 b-tagged category, as resulting from the 3HighestB selection method; only events out from the SR are shown; number of entries per bin is on the z-axis.

The number of signal events and the purity in and out of the SR are reported in Tab. 5.3 for the selection with the three different methods.

4th jet selection	jets pairing	events in SR	purity in SR	events out SR	purity out SR
4HighestB	min Δm_{jj}	17084 (6.2%)	79.5%	14415 (45.7%)	14%
3HighestB	min Δm_{jj}	12503 (4.5%)	78.9%	6261 (66.6%)	11.5%
RL	min Δm_{jj}	5766 (4.2%)	84.9%	4408 (43.3%)	14.1%

Table 5.3: Purity and number of events in and out of the SR for three different methods used for the fourth jet selection.

As seen also in Tab. 5.2, the 4HighestB leads to the higher statistics and this is refleted in the SR too. However, it presents the lowest purity among the three. The 3HighestB method is the one with the highest purity in the SR and also with the lowest fraction of signal out from the SR. Thus, it ends up to be a good compromise between the purity and the signal statistics. Furthermore, it does not exploit the b-tag of the fourth jet and this

is fundamental for the background estimation. Thus, the 3HighestB method has been chosen to select and pair the four final jets in each event.

The result of the application of the 3HighestB selection method to the SM signal in the 4 b-tagged category is shown in Fig. 5.9, 5.10 and Fig. 5.11. In Fig. 5.12, the 2-D mass plane is shown after a re-binning to get a 15 GeV/bin, almost equivalent to the current experimental resolution. The SR has been also modified to suit into the new binning, taking the previously mentioned ellipse as a baseline. The resulting statistics for the SM signal is: 12633 events (67%) in the SR and 6131 out from the SR. These numbers are of course not normalized to the SM cross section yet.

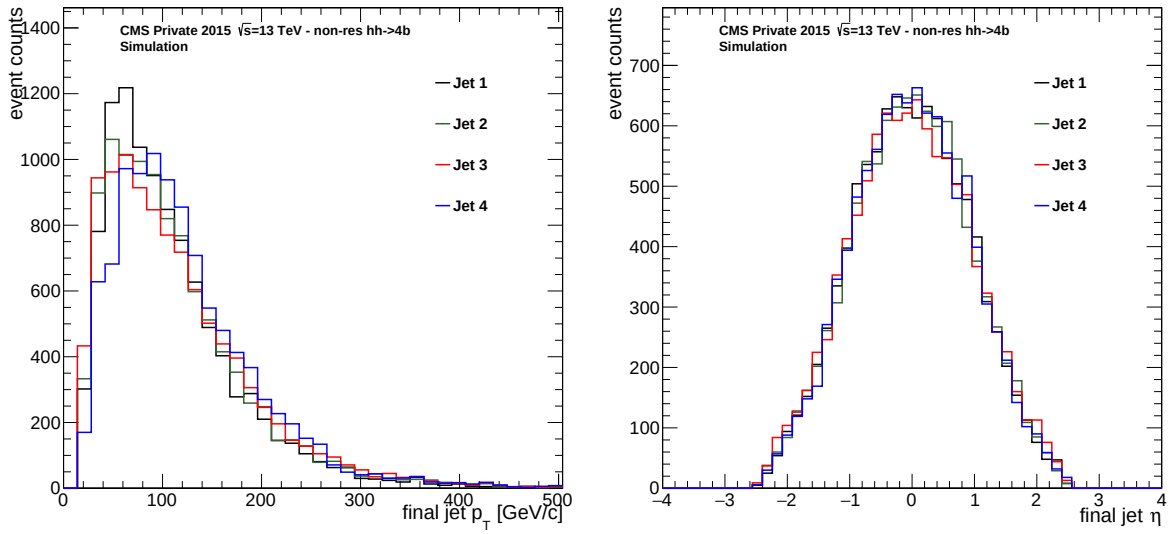

Figure 5.9: Distribution of the p_{T}, $|\eta|$ for the four final selected jets in the 4 b-tagged category.

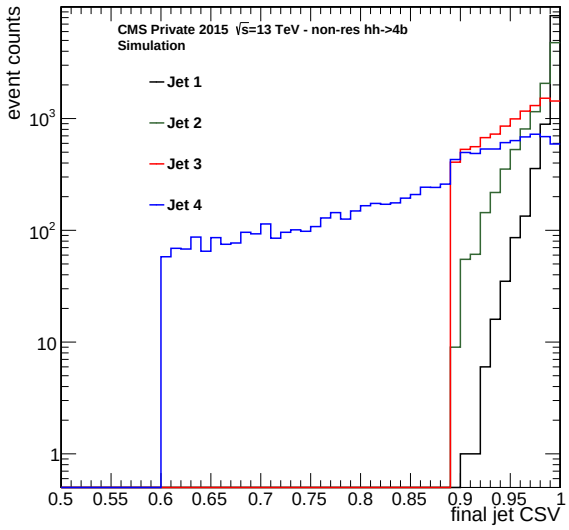

Figure 5.10: Distribution of the CSVv2 discriminator for the four final selected jets in the 4 b-tagged category.

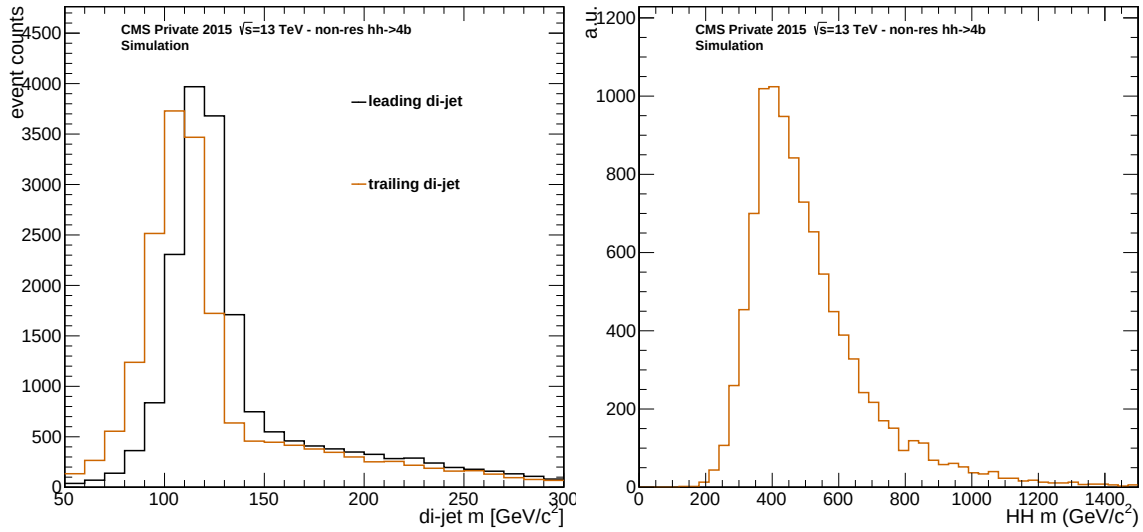

Figure 5.11: Distribution of the two di-jets invariant mass (left) and of the four body mass for the SM signal in the 4 b-tagged category.

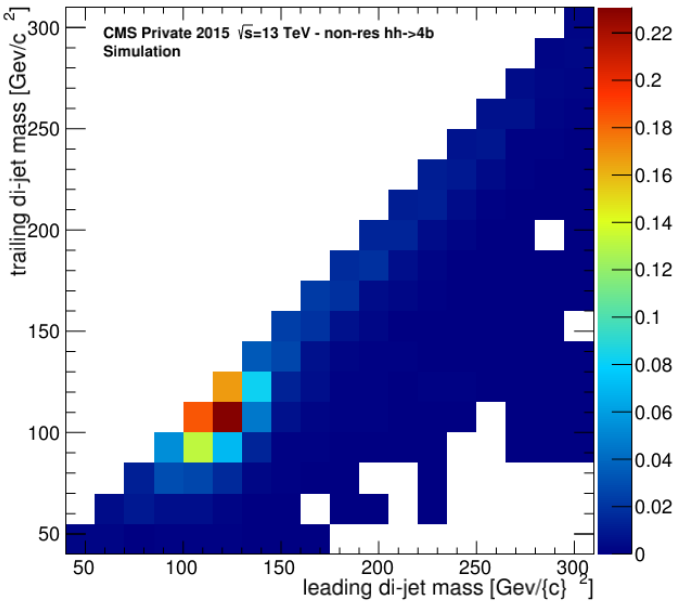

Figure 5.12: Re-binned 2-D plane for the SM signal in the 4 b-tagged category, as resulting from the 3HighestB selection method.

5.6 Background modelling study

The multi-jet irreducible background has to be modelled in the SR in order to perform the shape fit. A template which is as close as possible to the background shape in that region is needed. In addition, also the multi-jet processes yield need to be predicted with a certain accuracy in order to fix the background normalization. Since the MC simulations are not reliable for a quantitative multi-jet background determination, a data-driven method has to be developed.

The number of b-tagged jets can be used as a discriminant to get a set of background dominated data. Considering as signal category the 4 b-tagged one, the background template can be extracted from the data with 3 b-tagged jets only. Data with three b-tagged jets present in fact a kinematics which is very similar to the one in the signal category. This can be a good start for modeling the backgrounds since the QCD multi-jet present on average less b-tagged jets than the signal. The multi-jet background is expected to be dominant in a 2 b-tagged category and the signal to noise fraction in a 3 b-tagged category is estimated to be a factor 3 less than for 4 b-tagged.

A preliminary study on background estimation have been performed on data collected during the Run 1 at $\sqrt{s}$ = 8 TeV. The signal category included data with 3 b-tagged jets (2 on-line CSV in the trigger) while the background was extracted from data with 2 b-tagged jets only. However, the data-driven background was not predicting the right 2-D shape so large systematics had to be included. In that study, the plane considered for the final shape fit was the output of a Boosted Decision Tree versus the average mass of the two reconstructed di-jets, as shown in Fig. 5.13. The same plane has been reconstructed for the Run 2 data. The shape differences between the 4 b-tagged category and the 3 b-tagged category has been measured to be higher than 4 sigma with a non uniformity in the 2-D plane. Thus, this plane selection has not been considered for a shape fit in the $\sqrt{s}$ = 13 TeV data analysis.

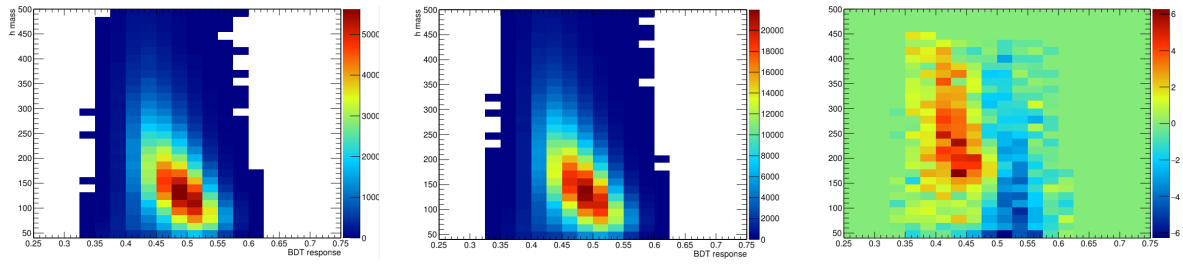

Figure 5.13: Signal and background templates in a 2-D plane from a preliminary study on LHC Run 1 data; the residues are shown in the plot on the right.

The 2-D plane defined by the masses of the two di-jets candidates is considered, as described in Sec.5.5, and it is shown in Fig. 5.14 for 4 b-tagged and 3 b-tagged categories in data. The SR has been modified to suit in the new binning, considering as a baseline the ellipse previously described. A greater uniformity with respect to the 2-D plane shown in Fig. 5.13 is evident. However, the distribution of the 3 b-tagged category in the SR can not be simply taken as background template for the 4 b-tagged.

To get a more reliable background template, the data-driven method can be improved with an estimation of the kinematical changes introduced by the cut on the fourth jet b-tagging. A reweighing procedure has thus been developed to correct the effect of the b-tagging with a factor which accounts for the per jet kimematic differences.
The main target of the method is to estimate the probability densities functions as a func-

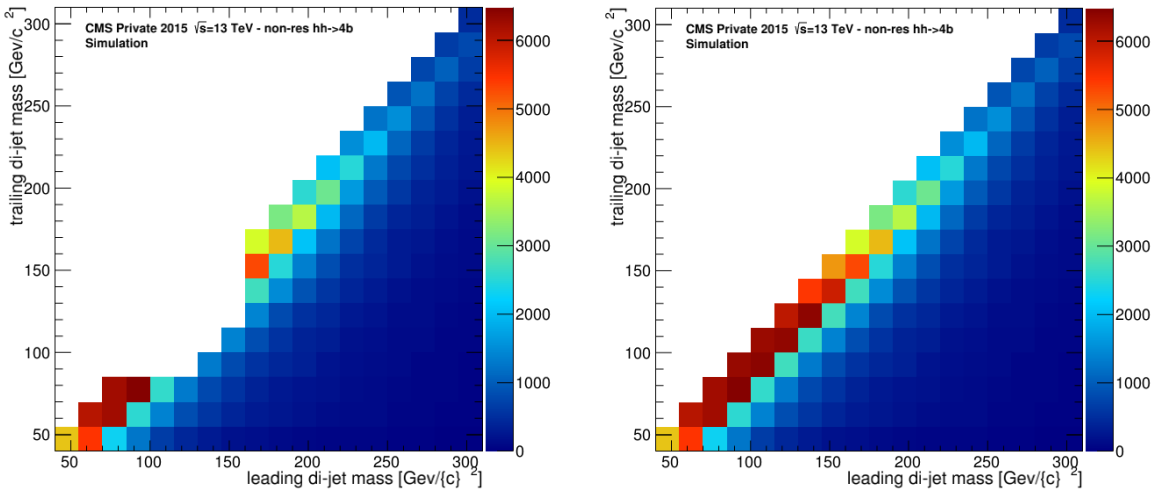

Figure 5.14: 2-D plane for 4 b-tagged (left) and 3 b-tagged (right) categories; in the 4 b-tagged only events out from the SR are shown; number of entries per bin is on the z-axis.

tion of a set of variables both for tagged and non-tagged jets. A 2-D binned matrix with the values of p_T and the $|\eta|$ of the jet has been filled looking at the events of the 3 b-tagged data category which are outside the SR. The optimal binning on the two variables has been set to: p_T [20., 50., 80., 120., 180., 300., 500.], $|\eta|$ [0., 0.5, 1., 1.5, 2.5]. Two matrices have been filled, one for b-tagged and one for non-b-tagged jets (loose CSVv2 working point). The event weight has then been obtained from the ratio of these two matrices. The distribution of these two variables is shown in Fig. 5.15, while the ratio is reported in Fig.5.16.

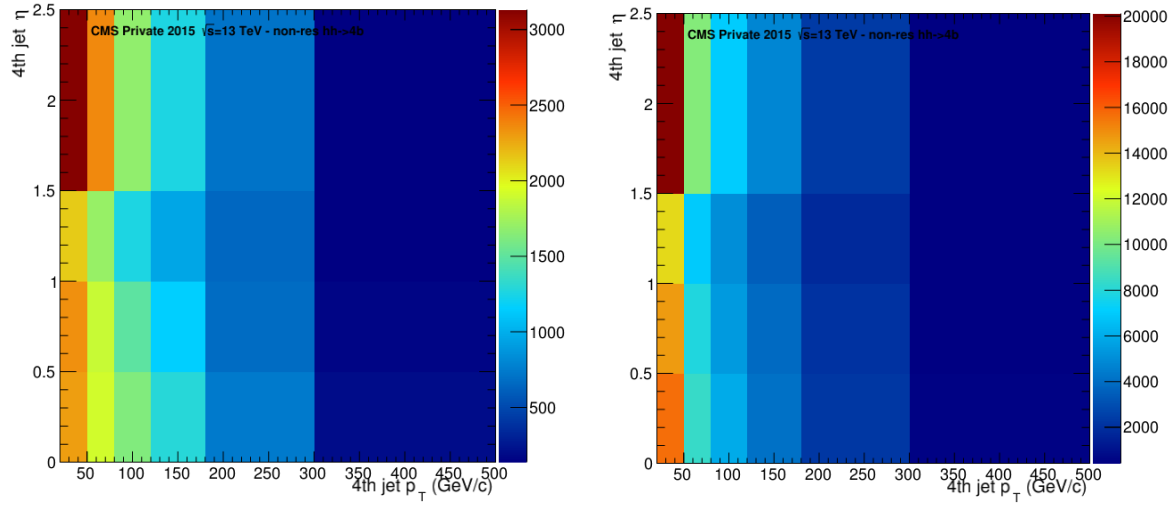

Figure 5.15: Fourth jet p_T versus $|\eta|$ distribution for the additional jets in the 3 b-tagged category in the data; fourth jet b-tagged (loose CSVv2) are considered in the plot on the left, jets not b-tagged in the plot on the right.

Each event in the 3 b-tagged category can be reweighed with the value of the ratio in the bin related to the fourth jet p_T- $|\eta|$. This reweighed data sample can then be used to extract the background normalization in the SR and to model the background shape for the 2-D fit.

To check the similarity of this reweighed 3 b-tagged data and the effective background

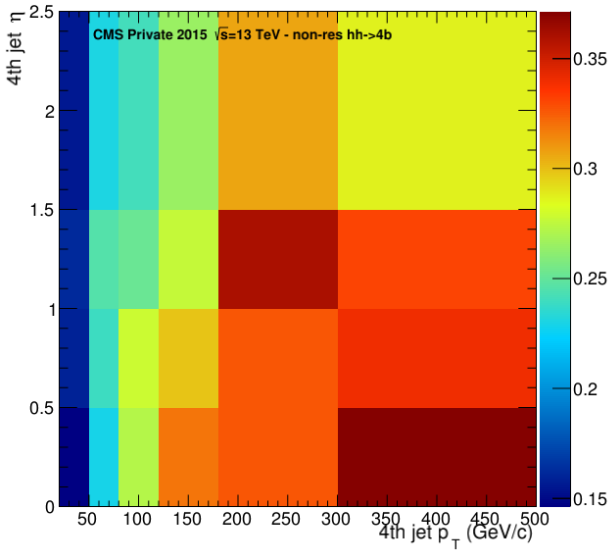

Figure 5.16: Ratio of the two p_T- $|\eta|$ plane shown in Fig.5.15.

in the SR, a pseudo-data sample has been created. This has been based on $t\bar{t}$ simulated background sample since the simulated multi-jet QCD samples do not have enough final statistics. A good agreement has been measured from this comparison and it is evident also in the residuals distribution shown in Fig.5.17.

This preliminary study indicates a feasibility of this kind of data-driven estimation. The presence of signal out from the signal region surely influenced the background extraction and the method can be improved by considering smaller side-band regions for the estimation of the weights.

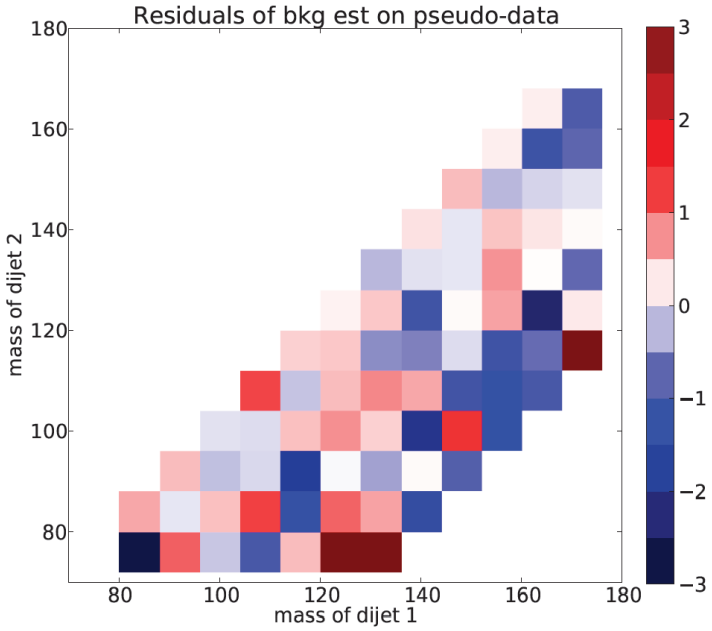

Figure 5.17: Residuals of the background estimation on the pseudo-data sample; z-axis is in sigma unit.

5.7 Results and prospects

In this chapter, a preliminary study of the di-Higgs pair production in the 4-b-jet final state have been discussed, using data collected by the CMS experiment in the 2015 run. The small amount of collected data at $\sqrt{s}$ = 13 TeV does not allow to extract meaningful results in terms of SM predictions, but the data can still be used to set up a search strategy that will be used to analyze the larger datasets expected in the next few years.

The presence of a very large multi-jet background from QCD interactions requires a tight selection which employs the b-tagging information of all the four leading jets produced in the decay of the Higgs boson pairs. In order to properly interpret the kinematics of the selected events, a choice has to be operated on the assignment of jet pairs to Higgs decay candidates. Three methods have been studied and their performance has been evaluated by considering the true generator-level information. A preliminary data-driven method has been developed in order to estimate the background shape and normalization in the region of interest.

A multivariate technique will be considered to increase the significance and, finally, a two-component fit can be used to extract a signal contamination from a signal-enriched region of the plane constructed on the two di-jet masses.

This preliminary study defined the basis for this searches that will be fully developed in the current year in order to exploit the higher amount of data that will be collected by the CMS experiment within the 2018.

Conclusions

This thesis presents the development and production of the new CMS Pixel Detector in the context of the CMS Phase 1 upgrade and the preliminary study of a physics case which will get a strong advantage by an improved Pixel Detector.

The design and features of the new readout chip (ROC) for the pixel detector have been shown. The pixel module test result have been illustrated together with the ROC wafer test results before and after the post production re-working. The target of the ROC wafer test has been to identify possible failures which occur during the wafer re-working (metal deposition, thinning, dicing). A failure grading of all the ROCs is also provided. The test has been performed before and after the re-working following the same procedure. An average down-grading rate of 5.2% per wafer have been measured. The ROC damages occurs mainly from single pixel defects or from an excessive non uniformity of the untrimmed threshold in the ROC. The latter is systematically present in four ROCs on left side of each wafer. Any other systematic worsening has not been measured.

The debugging of the bump-bonding structure, which connect the pixel pad of ROC and sensor, has also been shown for the module produced by the INFN consortium. The presence of cracks underneath the ROC passivation which occurred, in pre-production phase, after the module assembly have been avoided by increasing the diameter of the under bump metallization from 30 μm to 38 μm.

The Higgs bosons pairs production in p-p collision has been assumed as study case. BSM physical scenarios have been considered in the Higgs bosons pairs production, described by five degree of freedom in the Lagrangian. A statistical technique has been developed to define physical benchmarks in this 5-D parameters space based on the kinematics of the samples. A binned likelihood ratio has been defined as test statistic and it has been exploited as distance criterion to group the samples together. 1507 simulated samples have been analysed and grouped in 12 clusters, corresponding to 12 regions kinematically equivalent within a certain uncertainty. The results of this study will be considered by the LHC as guideline for the future non resonant di-Higgs production searches.

A preliminary study of the non-resonant Higgs boson pair decaying into $b\bar{b}b\bar{b}$ has finally been performed on data collected by CMS experiment in 2015. It consists in a comparison of different method for the reconstructed jets selection and pairing, and in the development of a preliminary data-driven background estimation method. The amount of data collected does not allow to extract a reasonable exclusion limit on the production cross section of non-resonant di-Higgs.

The analysis will continue over the next years with an accurate multi-jet background estimation and with the exploitation of multivariate analysis techniques. Considerable improvements to this search is expected to be given by the installation of the new pixel detector in 2017.

Acknowledgments

I feel very grateful to many people who spent their time, energies and know-how with me and for me.

I would like to thank:

My supervisor Dario Bisello and the co-supervisor Tommaso Dorigo for their precious support and guidance during the past three years.

Alexandra Oliveira and Mia Tosi for their active collaboration and for their advice on this thesis.

The CMS group in Padova, for having welcomed me since the beginning of my Ph.D and for their fundamental push in this conclusive period.

The CMS group of PSI for the beautiful and educational period I spent at their laboratory and for their friendliness. Special thanks to Beat Meier, Wolfram Erdmann and Roland Horisberger.

The IZM team, Thomas Fritzsch and Mario Rothermund, for the fruitful collaboration in the pixel upgrade project.

The colleagues involved in the CMS Phase 1 pixel upgrade project, in particular Daniel Pitzl and Simon Spannagel for the great sharing of knowledge, and all the members of the INFN consortium. Gian Mario Bilei, Alberto Messineo, Salvatore Costa and Roberto Dell'Orso, for allowed me to grow up in the course of this project. A special thank also to Devis Pantano, for his patience and his great professionalism.

Gino Bolla, for having received me in his great test beam team and for the opportunity to learn from his "active teaching".

Caterina Vernieri, Silvio Donato and Andrea Rizzi for their precious help in the starting phase of this new di-Higgs search, in particular for their contribution in the framework and trigger development.

The other members of the "clustering team": Florian Goertz, Carlo Gottardo and Pablo De Castro Manzano for the good work that we developed together.

My Ph.D fellows, Jacopo Pazzini and Alberto Zucchetta, for our coffee breaks and their precious suggestions.

My "Genéve group", Federica, Davide, Stefano, Michele, Andrea and all the others for their beautiful friendship and the great time we spent together.

My family, my parents, my sister and my brother, for having always supported and advised me during my academic path and my choices.

My new family, Sara. For having followed me in this adventure, for her constant presence, her perseverance, her patience.

Bibliography

[1] S. Chatrchyan et al. "Observation of a new boson at a mass of 125 GeV with the CMS experiment at the LHC". In: *Physics Letters B* 716.1 (2012), pp. 30 –61. ISSN: 0370-2693. DOI: http://dx.doi.org/10.1016/j.physletb.2012.08.021.

[2] G. Aad et al. "Observation of a new particle in the search for the Standard Model Higgs boson with the ATLAS detector at the LHC". In: *Physics Letters B* 716.1 (2012), pp. 1 –29. ISSN: 0370-2693. DOI: http://dx.doi.org/10.1016/j.physletb.2012.08.020.

[3] Y. Fukuda et al. "Evidence for Oscillation of Atmospheric Neutrinos". In: *Phys. Rev. Lett.* 81 (8 1998), pp. 1562–1567. DOI: 10.1103/PhysRevLett.81.1562.

[4] A. Aguilar et al. "Evidence for neutrino oscillations from the observation of $\overline{\nu}_e$ appearance in a $\overline{\nu}_\mu$ beam". In: *Phys. Rev. D* 64 (11 2001), p. 112007. DOI: 10.1103/PhysRevD.64.112007.

[5] A. Cohen, D. Kaplan, and A. Nelson. "Spontaneous baryogenesis at the weak phase transition". In: *Physics Letters B* 263.1 (1991), pp. 86 –92. ISSN: 0370-2693. DOI: 10.1016/0370-2693(91)91711-4.

[6] Planck_Collaboration. "Planck 2013 results. XVI. Cosmological parameters". In: *A&A* 571 (2014), A16. DOI: 10.1051/0004-6361/201321591.

[7] S. P. Martin. "A Supersymmetry Primer". In: *Perspectives on Supersymmetry II*. 2011. Chap. 1, pp. 1–153. DOI: 10.1142/9789814307505_0001.

[8] L. Evans and P. Bryant. "LHC Machine". In: *Journal of Instrumentation* 3.08 (2008), S08001.

[9] S. Myers. *The LEP Collider, from design to approval and commissioning*. John Adams' Lecture. Delivered at CERN, 26 Nov 1990. Geneva: CERN, 1991.

[10] ATLAS_Collaboration. "The ATLAS Experiment at the CERN Large Hadron Collider". In: *Journal of Instrumentation* 3.08 (2008), S08003.

[11] CMS_Collaboration. "The CMS experiment at the CERN LHC". In: *Journal of Instrumentation* 3.08 (2008), S08004.

[12] LHCb_Collaboration. "The LHCb Detector at the LHC". In: *Journal of Instrumentation* 3.08 (2008), S08005.

[13] ALICE_Collaboration. "The ALICE experiment at the CERN LHC". In: *Journal of Instrumentation* 3.08 (2008), S08002.

[14] CMS_Collaboration. *Report on collected luminosity*. URL: https://twiki.cern.ch/twiki/bin/view/CMSPublic/LumiPublicResults.

[15] G. Aad et al. "Measurement of the Inelastic Proton-Proton Cross-Section at $\sqrt{s} = 7$ TeV with the ATLAS Detector". In: *Nature Commun.* 2 (2011), p. 463. DOI: 10.1038/ncomms1472. arXiv: 1104.0326 [hep-ex].

[16] W. Stirling. *private communication*. URL: http://www.hep.ph.ic.ac.uk/~wstirlin/plots/plots.html.

[17] CMS_Collaboration. "The CMS magnet project: Technical Design Report". In: Technical Design Report CMS (1997).

[18] CMS_Collaboration. "The Tracker Project - Technical Design Report". In: Technical Design Report CMS 006 (1998).

[19] CMS_Collaboration. "Addendum to The Tracker Project - Technical Design Report". In: Technical Design Report CMS 016 (2000).

[20] H. Spieler. *Semiconductor Detector Systems*. 2005.

[21] H. C. Kastli, M. Barbero, W. Erdmann, C. Hormann, R. Horisberger, D. Kotlinski, and B. Meier. "Design and performance of the CMS pixel detector readout chip". In: *Nucl. Instrum. Meth.* A565 (2006), pp. 188–194. DOI: 10.1016/j.nima.2006.05.038. arXiv: physics/0511166 [physics].

[22] W. Erdmann. "The CMS pixel detector". In: *International Journal of Modern Physics A* 25.07 (2010), pp. 1315–1337. DOI: 10.1142/S0217751X10049098.

[23] CMS_Collaboration. In: (). URL: https://twiki.cern.ch/twiki/bin/view/CMSPublic/PixelOfflineLHCC2015.

[24] E. S. C. Claeys. *Radiation Effects in Advanced Semiconductor Materials and Devices*. Springer, 2002.

[25] K. Klein. "The CMS Silicon Strip Tracker-Overview and Status". In: *arXiv preprint physics/0610259* (2006).

[26] "Charge collection in silicon strip detectors". In: *Nuclear Instruments and Methods in Physics Research* 214.23 (1983), pp. 253 –260. ISSN: 0167-5087.

[27] M Raymond, P Moreira, et al. "The CMS tracker APV25 0.25μm CMOS readout chip". In: (2000).

[28] L. Borrello, E. Focardi, A. Macchiolo, and A. Messineo. *Sensor design for the CMS silicon strip tracker*. Tech. rep. CERN-CMS-NOTE-2003-020, 2003.

[29] CMS_Collaboration. In: (). URL: https://twiki.cern.ch/twiki/bin/view/CMSPublic/EcalDPGResults.

[30] CMS_Collaboration. "The performance of the CMS muon detector in proton-proton collisions at $\sqrt{s}$ = 7 TeV at the LHC". In: *Journal of Instrumentation* 8.11 (2013), P11002.

[31] CMS_Collaboration. "Description and performance of track and primary-vertex reconstruction with the CMS tracker". In: *Journal of Instrumentation* 9.10 (2014), P10009.

[32] R. Fruhwirth. "Application of kalman filtering to track and vertex fitting". In: *Nucl.Instr. Meth. Phys. Res. Section A* 262.2-3 (1987), pp. 444–450.

[33] K. Rose. "Deterministic annealing for clustering, compression, classification, regression, and related optimization problems". In: *Proceedings of the IEEE* 86.11 (1998), pp. 2210–2239. ISSN: 0018-9219. DOI: 10.1109/5.726788.

[34] W. Waltenberger, R. Frhwirth, and P. Vanlaer. "Adaptive vertex fitting". In: *Journal of Physics G: Nuclear and Particle Physics* 34.12 (2007), N343.

[35] CMS_Collaboration. *CMS Tracker performance plots*. URL: https://twiki.cern.ch/twiki/bin/view/CMSPublic/PhysicsResultsTRK.

[36] CMS_Collaboration. *Particle-Flow Event Reconstruction in CMS and Performance for Jets, Taus, and MET*. Tech. rep. CMS-PAS-PFT-09-001. 2009. Geneva: CERN, 2009.

[37] CMS_Collaboration. *Commissioning of the Particle-flow Event Reconstruction with the first LHC collisions recorded in the CMS detector*. Tech. rep. CMS-PAS-PFT-10-001. 2010.

[38] F. Halzen and A. Martin. *Quark & Leptons: an introductory course in modern particle physics*. Wiley India Pvt. Limited, 2008. ISBN: 9788126516568.

[39] M. Cacciari, G. P. Salam, and G. Soyez. "The anti- k t jet clustering algorithm". In: *Journal of High Energy Physics* 2008.04 (2008), p. 063.

[40] M. Cacciari and G. P. Salam. "Dispelling the N^3 myth for the k_t jet-finder". In: *Phys. Lett.* B641 (2006), pp. 57–61. DOI: 10.1016/j.physletb.2006.08.037. arXiv: hep-ph/0512210 [hep-ph].

[41] CMS_Collaboration. "Determination of jet energy calibration and transverse momentum resolution in CMS". In: *Journal of Instrumentation* 6.11 (2011), P11002.

[42] CMS_Collaboration. "Identification of b-quark jets with the CMS experiment". In: *Journal of Instrumentation* 8.04 (2013), P04013.

[43] CMS_Collaboration. "Performance of b-Tagging Algorithms in 25ns Data at 13TeV". In: *CMS-DP-2015-056* (2015).

[44] S. Cittolin, A. Rcz, and P. Sphicas. *CMS The TriDAS Project: Technical Design Report, Volume 2: Data Acquisition and High-Level Trigger. CMS trigger and data-acquisition project*. Technical Design Report CMS. Geneva: CERN, 2002.

[45] T. Bawej et al. "The New CMS DAQ System for Run-2 of the LHC". In: (2014).

[46] CERN. *LHC commissioning schedule*. URL: https://lhc-commissioning.web.cern.ch/lhc-commissioning/schedule/LHC-long-term.htm.

[47] Dominguez, A and Abbaneo, D and Arndt, K and Bacchetta, N and others. *CMS Technical Design Report for the Pixel Detector Upgrade*. Tech. rep. CERN-LHCC-2012-016. CMS-TDR-11. Additional contacts: Jeffrey Spalding, Fermilab, Jeffrey.Spalding@cern.ch Didier Contardo, Universite Claude Bernard-Lyon I, didier.claude.contardo@cern.ch. Geneva: CERN, 2012.

[48] C. Roland. "Track reconstruction in heavy ion events using the CMS tracker". In: *Nucl. Instrum. Meth.* A566 (2006), pp. 123–126. DOI: 10.1016/j.nima.2006.05.023.

[49] T. Rohe, A. Bean, V. Radicci, and J. Sibille. "Planar sensors for the upgrade of the CMS pixel detector". In: *Nucl. Instrum. Meth.* A650 (2011), pp. 136–139. DOI: 10.1016/j.nima.2010.11.156.

[50] G. B. Cerati et al. "Radiation tolerance of the CMS forward pixel detector". In: *Nucl. Instrum. Meth.* A600 (2009), pp. 408–416. DOI: 10.1016/j.nima.2008.11.114.

[51] F. Lemeilleur, G. Lindstrom, and S. Watts. "Third RD48 status report". In: (1999).

[52] J. K. et al.. "Streifendetektor Patentoffenlegungsschrift". In: (1997).

[53] "Design and test of pixel sensors for the CMS experiment". In: *Nucl. Instrum. Meth.* A461.13 (2001). 8th Pisa Meeting on Advanced Detectors, pp. 182 –184. ISSN: 0168-9002. DOI: http://dx.doi.org/10.1016/S0168-9002(00)01201-8.

[54] B. Meier and J. Lazo-Flores. "Pixel Front-end development for CMS". In: *PoS Vertex* 28 (2009).

[55] D. Hits and A. Starodumov. "The CMS pixel readout chip for the Phase 1 Upgrade". In: *Journal of Instrumentation* 10.05 (2015), p. C05029.

[56] CMS_Collaboration. *pXar*. URL: https://github.com/psi46/pxar.

[57] CMS_Collaboration. *CMS pixel phase 1 upgrade official database*. URL: http://cmspixelprod.pi.infn.it/.

[58] CMS_Collaboration. *psi46test*. URL: https://github.com/psi46/psi46test.

[59] CMS_Collaboration. *grlog*. URL: https://github.com/psi46/grlog.

[60] S. O. Bilson-Thompson, F. Markopoulou, and L. Smolin. "Quantum gravity and the standard model". In: *Classical and Quantum Gravity* 24.16 (2007), p. 3975.

[61] M. Peskin and D. Schroeder. *An Introduction to Quantum Field Theory*. Advanced book classics. Addison-Wesley Publishing Company, 1995. ISBN: 9780201503975.

[62] L. G. Sheldon. "Partial-symmetries of weak interactions". In: *Nucl. phys* 22 (1961), pp. 579–588.

[63] S. Weinberg. "A model of leptons". In: *Physical review letters* 19.21 (1967), p. 1264.

[64] A. Salam and J. C. Ward. "Electromagnetic and weak interactions". In: *Physics Letters* 13.2 (1964), pp. 168–171.

[65] J. Goldstone, A. Salam, and S. Weinberg. "Broken symmetries". In: *Physical Review* 127.3 (1962), p. 965.

[66] S. L. Glashow, J. Iliopoulos, and L. Maiani. "Weak interactions with lepton-hadron symmetry". In: *Physical Review D* 2.7 (1970), p. 1285.

[67] H. Fritzsch, M Gell-Mann, and H Leutwyler. "Advantages of the color octet gluon picture". In: *Murray Gell-Mann: Selected Papers* 40.4 (2010), p. 262.

[68] D. J. Griffiths. *Introduction to quantum mechanics*. 1995.

[69] M. Gell-Mann. "Symmetries of baryons and mesons". In: *Physical Review* 125.3 (1962), p. 1067.

[70] G. Zweig. *An SU _3 model for strong interaction symmetry and its breaking*. Tech. rep. CM-P00042884, 1964.

[71] C. Rubbia. "Experimental observation of the intermediate vector bosons W^+, W^-, and Z^0". In: *Rev. Mod. Phys.* 57 (3 1985), pp. 699–722. DOI: 10.1103/RevModPhys.57.699.

[72] F. Englert and R. Brout. "Broken Symmetry and the Mass of Gauge Vector Mesons". In: *Phys. Rev. Lett.* 13 (9 1964), pp. 321–323. DOI: 10.1103/PhysRevLett.13.321.

[73] J. Goldstone, A. Salam, and S. Weinberg. "Broken Symmetries". In: *Phys. Rev.* 127 (3 1962), pp. 965–970. DOI: 10.1103/PhysRev.127.965.

[74] LHC Higgs Cross Section Working Group, S. Heinemeyer, C. Mariotti, G. Passarino, and R. Tanaka (Eds.) "Handbook of LHC Higgs Cross Sections: 3. Higgs Properties". In: *CERN-2013-004* (CERN, Geneva, 2013). arXiv: 1307.1347 [hep-ph].

[75] LHC Higgs Cross Section Working Group. *Twiki page*. URL: https://twiki.cern.ch/twiki/bin/view/LHCPhysics/LHCHXSWGCrossSectionsFigures.

[76] G. Aad et al. "Combined Measurement of the Higgs Boson Mass in pp Collisions at $\sqrt{s} = 7$ and 8 TeV with the ATLAS and CMS Experiments". In: *Phys. Rev. Lett.* 114 (19 2015), p. 191803. DOI: 10.1103/PhysRevLett.114.191803.

[77] S. Chatrchyan, V. Khachatryan, A. M. Sirunyan, A. Tumasyan, W. Adam, and Bergauer. "Measurement of the properties of a Higgs boson in the four-lepton final state". In: *Phys. Rev. D* 89 (9 2014), p. 092007. DOI: 10.1103/PhysRevD.89.092007.

[78] C. Collaboration. "Observation of the diphoton decay of the Higgs boson and measurement of its properties". In: *The European Physical Journal C* 74 (10 2014). DOI: doi:10.1140/epjc/s10052-014-3076-z..

[79] R. Barbieri, D. Buttazzo, K. Kannike, F. Sala, and A. Tesi. "Exploring the Higgs sector of a most natural NMSSM". In: *Phys. Rev. D 87*, 115018 (2013). DOI: 10.1103/PhysRevD.87.115018. arXiv: 1304.3670 [hep-ph].

[80] L. Randall and R. Sundrum. "Large Mass Hierarchy from a Small Extra Dimension". In: *Phys. Rev. Lett.* 83 (17 1999), pp. 3370–3373. DOI: 10.1103/PhysRevLett.83.3370.

[81] R. Frederix, S. Frixione, V. Hirschi, F. Maltoni, O. Mattelaer, P. Torrielli, E. Vryonidou, and M. Zaro. "Higgs pair production at the {LHC} with {NLO} and parton-shower effects". In: *Physics Letters B* 732 (2014), pp. 142 –149. ISSN: 0370-2693. DOI: http://dx.doi.org/10.1016/j.physletb.2014.03.026.

[82] F. Goertz. "Indirect Handle on the Down-Quark Yukawa Coupling". In: *Phys.Rev.Lett.* 113.26 (2014), p. 261803. DOI: 10.1103/PhysRevLett.113.261803. arXiv: 1406.0102 [hep-ph].

[83] G. Giudice, C. Grojean, A. Pomarol, and R. Rattazzi. "The Strongly-Interacting Light Higgs". In: *JHEP* 0706 (2007), p. 045. DOI: 10.1088/1126-6708/2007/06/045. arXiv: hep-ph/0703164 [hep-ph].

[84] W. Buchmuller and D. Wyler. "Effective Lagrangian Analysis of New Interactions and Flavor Conservation". In: *Nucl.Phys.* B268 (1986), pp. 621–653. DOI: 10.1016/0550-3213(86)90262-2.

[85] R. Contino, M. Ghezzi, C. Grojean, M. Muhlleitner, and M. Spira. "Effective Lagrangian for a light Higgs-like scalar". In: *JHEP* 1307 (2013), p. 035. DOI: 10.1007/JHEP07(2013)035. arXiv: 1303.3876 [hep-ph].

[86] M. Gillioz, R. Grober, C. Grojean, M. Muhlleitner, and E. Salvioni. "Higgs Low-Energy Theorem (and its corrections) in Composite Models". In: *JHEP* 1210 (2012), p. 004. DOI: 10.1007/JHEP10(2012)004. arXiv: 1206.7120 [hep-ph].

[87] S. Dawson, A. Ismail, and I. Low. "What is in the loop? The anatomy of double Higgs production". In: *Phys. Rev.* D91.11 (2015), p. 115008. DOI: 10.1103/PhysRevD.91.115008. arXiv: 1504.05596 [hep-ph].

[88] A. Belyaev, M. Drees, O. J. Eboli, J. Mizukoshi, and S. Novaes. "Supersymmetric Higgs pair discovery prospects at hadron colliders". In: (1999), pp. 748–751. arXiv: hep-ph/9910400 [hep-ph].

[89] M. Spira and J. D. Wells. "Higgs bosons strongly coupled to the top quark". In: *Nucl.Phys.* B523 (1998), pp. 3–16. DOI: 10.1016/S0550-3213(98)00107-2. arXiv: hep-ph/9711410 [hep-ph].

[90] C. Han, X. Ji, L. Wu, P. Wu, and J. M. Yang. "Higgs pair production with SUSY QCD correction: revisited under current experimental constraints". In: *JHEP* 1404 (2014), p. 003. DOI: 10.1007/JHEP04(2014)003. arXiv: 1307.3790 [hep-ph].

[91] A. Falkowski and F. Riva. "Model-independent precision constraints on dimension-6 operators". In: *JHEP* 1502 (2015), p. 039. DOI: 10.1007/JHEP02(2015)039. arXiv: 1411.0669 [hep-ph].

[92] A. Falkowski. "Effective field theory approach to LHC Higgs data". In: (2015). arXiv: 1505.00046 [hep-ph].

[93] B. Fuks, F. Maltoni, K. Mawatari, K. Mimasu, and V. Sanz. " https://github.com/kenmimasu/Rosetta ".

[94] D. de Florian and J. Mazzitelli. "Next-to-Next-to-Leading Order QCD Corrections to Higgs Boson Pair Production". In: *PoS* LL2014 (2014), p. 029. arXiv: 1405.4704 [hep-ph].

[95] J. Grigo, K. Melnikov, and M. Steinhauser. "Virtual corrections to Higgs boson pair production in the large top quark mass limit". In: *Nucl.Phys.* B888 (2014), pp. 17–29. DOI: 10.1016/j.nuclphysb.2014.09.003. arXiv: 1408.2422 [hep-ph].

[96] J. Gao, M. Guzzi, J. Huston, H.-L. Lai, Z. Li, et al. "CT10 next-to-next-to-leading order global analysis of QCD". In: *Phys.Rev.* D89.3 (2014), p. 033009. DOI: 10.1103/PhysRevD.89.033009. arXiv: 1302.6246 [hep-ph].

[97] R. Grober, M. Muhlleitner, M. Spira, and J. Streicher. "NLO QCD Corrections to Higgs Pair Production including Dimension-6 Operators". In: (2015). arXiv: 1504.06577 [hep-ph].

[98] F. Maltoni, E. Vryonidou, and M. Zaro. "Top-quark mass effects in double and triple Higgs production in gluon-gluon fusion at NLO". In: *JHEP* 1411 (2014), p. 079. DOI: 10.1007/JHEP11(2014)079. arXiv: 1408.6542 [hep-ph].

[99] R. Frederix, S. Frixione, V. Hirschi, F. Maltoni, O. Mattelaer, et al. "Higgs pair production at the LHC with NLO and parton-shower effects". In: *Phys.Lett.* B732 (2014), pp. 142–149. DOI: 10.1016/j.physletb.2014.03.026. arXiv: 1401.7340 [hep-ph].

[100] J. Grigo, J. Hoff, and M. Steinhauser. "Higgs boson pair production: top quark mass effects at NLO and NNLO". In: (2015). arXiv: 1508.00909 [hep-ph].

[101] D. de Florian and J. Mazzitelli. "Higgs pair production at next-to-next-to-leading logarithmic accuracy at the LHC". In: (2015). arXiv: 1505.07122 [hep-ph].

[102] M. Dall'Osso, T. Dorigo, C. A. Gottardo, A. Oliveira, M. Tosi, and F. Goertz. "Higgs Pair Production: Choosing Benchmarks With Cluster Analysis". In: (2015). arXiv: 1507.02245 [hep-ph].

[103] G. Aad et al. "Search for Higgs Boson Pair Production in the $\gamma\gamma b\bar{b}$ Final State Using pp Collision Data at $\sqrt{s} = 8$ TeV from the ATLAS Detector". In: *Phys. Rev. Lett.* 114 (8 2015), p. 081802. DOI: 10.1103/PhysRevLett.114.081802.

[104] CMS_Collaboration. *Search for resonant HH production in 2gamma+2b channel*. Tech. rep. CMS-PAS-HIG-13-032. Geneva: CERN, 2014.

[105] G. e. a. Aad. "Search for Higgs boson pair production in the $b\bar{b}b\bar{b}$ final state from pp collisions at $\sqrt{s} = 8$ TeV with the ATLAS detector". In: (2015). arXiv: 1506.00285 [hep-ex].

[106] V. Khachatryan et al. "Search for resonant pair production of Higgs bosons decaying to two bottom quarkantiquark pairs in protonproton collisions at 8 TeV". In: *Phys. Lett.* B749 (2015), pp. 560–582. DOI: 10.1016/j.physletb.2015.08.047. arXiv: 1503.04114 [hep-ex].

[107] G. Aad et al. "Searches for Higgs boson pair production in the $hh \to bb\tau\tau, \gamma\gamma WW^*, \gamma\gamma bb, bbbb$ channels with the ATLAS detector". In: *Phys. Rev.* D92 (2015), p. 092004. DOI: 10.1103/PhysRevD.92.092004. arXiv: 1509.04670 [hep-ex].

[108] A. Bednyakov, A. Pikelner, and V. Velizhanin. "Yukawa coupling beta-functions in the Standard Model at three loops". In: *Physics Letters B* 722.45 (2013), pp. 336 –340. ISSN: 0370-2693. DOI: 10.1016/j.physletb.2013.04.038.

[109] P. Artoisenet, P. de Aquino, F. Demartin, R. Frederix, and S. e. a. Frixione. "A framework for Higgs characterisation". In: *JHEP* 1311 (2013), p. 043. DOI: 10.1007/JHEP11(2013)043. arXiv: 1306.6464 [hep-ph].

[110] B. Hespel, D. Lopez-Val, and E. Vryonidou. "Higgs pair production via gluon fusion in the Two-Higgs-Doublet Model". In: *JHEP* 1409 (2014), p. 124. DOI: 10.1007/JHEP09(2014)124. arXiv: 1407.0281 [hep-ph].

[111] S. Frixione, F. Stoeckli, P. Torrielli, and B. R. Webber. "NLO QCD corrections in Herwig++ with MC@NLO". In: *JHEP* 1101 (2011), p. 053. DOI: 10.1007/JHEP01(2011)053. arXiv: 1010.0568 [hep-ph].

[112] J. Alwall, R. Frederix, S. Frixione, V. Hirschi, F. Maltoni, et al. "The automated computation of tree-level and next-to-leading order differential cross sections, and their matching to parton shower simulations". In: *JHEP* 1407 (2014), p. 079. DOI: 10.1007/JHEP07(2014)079. arXiv: 1405.0301 [hep-ph].

[113] R. D. Ball et al. "Precision determination of electroweak parameters and the strange content of the proton from neutrino deep-inelastic scattering". In: *Nucl.Phys.* B823 (2009), pp. 195–233. DOI: 10.1016/j.nuclphysb.2009.08.003. arXiv: 0906.1958 [hep-ph].

[114] J. C. Collins and D. E. Soper. "Angular distribution of dileptons in high-energy hadron collisions". In: *Phys. Rev. D* 16 (7 1977), pp. 2219–2225. DOI: 10.1103/PhysRevD.16.2219.

[115] B. Aslan and G. Zech. "A New class of binning free, multivariate goodness of fit tests: The Energy tests". In: (2002). arXiv: hep-ex/0203010 [hep-ex].

[116] S. Baker and R. D. Cousins. "Clarification of the Use of Chi Square and Likelihood Functions in Fits to Histograms". In: *Nucl. Instr. Meth.* 221 (1984), pp. 437–442.

[117] S. Wilks. "The Large-Sample Distribution of the Likelihood Ratio for Testing Composite Hypotheses". In: *Annals Math.Statist.* 9.1 (1938), pp. 60–62. DOI: 10.1214/aoms/1177732360.

[118] T. Plehn, M. Spira, and P. Zerwas. "Pair production of neutral Higgs particles in gluon-gluon collisions". In: *Nucl.Phys.* B479 (1996), pp. 46–64. DOI: 10.1016/0550-3213(96)00418-X. arXiv: hep-ph/9603205 [hep-ph].

[119] M. Dall'Osso, T. Dorigo, C. A. Gottardo, A. Oliveira, M. Tosi, and F. Goertz. Tech. rep. URL: https://twiki.cern.ch/twiki/bin/view/Sandbox/NonResonantHHAtLHC.

[120] C. Collaboration. Tech. rep. URL: https://twiki.cern.ch/twiki/bin/view/LHCPhysics/LHCHXSWG.

[121] J. Alwall, M. Herquet, F. Maltoni, O. Mattelaer, and T. Stelzer. "MadGraph 5: going beyond". In: *Journal of High Energy Physics* 2011.6 (2011), pp. 1–40. ISSN: 1029-8479. DOI: 10.1007/JHEP06(2011)128.

[122] S. Agostinelli et al. "Geant4a simulation toolkit". In: *Nuclear Instruments and Methods in Physics Research Section A: Accelerators, Spectrometers, Detectors and Associated Equipment* 506.3 (2003), pp. 250 –303. ISSN: 0168-9002. DOI: http://dx.doi.org/10.1016/S0168-9002(03)01368-8.

[123] T. Sjstrand, S. Mrenna, and P. Skands. "PYTHIA 6.4 physics and manual". In: *Journal of High Energy Physics* 2006.05 (2006), p. 026.